Physics and Applications of Graphene-based Nanostructures and Nano-meta Materials

Thesis by

Chen-Chih Hsu

In Partial Fulfillment of the Requirements for

the degree of

Doctor of Philosophy

CALIFORNIA INSTITUTE OF TECHNOLOGY

Pasadena, California

2020

Defended December 16, 2019

Chen-Chih Hsu
ORCID: 0000-0003-1130-5240

ACKNOWLEDGEMENTS

It has been a long journey that words can hardly describe. I could not have completed my thesis without many people's help and support along the way. First and foremost, I would like to thank my advisor, Prof. Nai-Chang Yeh, for her continual guidance and supervision in all these years. Her wealth of knowledge, endless energy, and enthusiasm toward science inspires me to become a scientist and motivates me to pursue relentlessly in science research in my PhD career. She has spent countless hours discussing and exchanging ideas with me when I encountered difficulties in my research and also giving me encouragement whenever I faced any setbacks. Additionally, she has provided me with a great research environment to hone my skills and knowledge as a scientist by giving me the access to the KNI facilities and resources to attend various conferences for many years. Without her tremendous support and patience, I could not have reached the end goals of completing my thesis and finalizing my research.

Secondly, I would like to thank the following members for taking their time to review my thesis and serve as part of my thesis defense committee: Prof. Michael Roukes as the Chair, Prof. Jason Alicea, and Prof. David Hsieh. I'd like to thank Prof. Harry Atwater as well for sitting on my candidacy committee. I will always remember their sincere encouragement and keep their invaluable advices close to my heart as I embark on my future endeavors. Thirdly, my research would not have been achieved without the kind support of equipment from these professors: Prof George Rossman for his Raman spectrometer, Prof. Tom Rosenbaum for his PPMS, and Prof. Chih-I Wu for his Keithley 2400.

In the Yeh group, I would like to thank many excellent colleagues and students I have met throughout the years: Marcus Teague, David Boyd, Wei-Shiuan Tseng, Chien-Chang Chen, Jaiqing Wang, Wei-Hsiang Lin, Jacob Bagley, Adrian Llanos, Deepan Kishore Kumar, Chen-Hsuan Lu, Yen-Chun Chen, Jan-Kai Chang, Meng-Huan Jao, Yiran Zhang, Kathleen Yang, and Yiliang Li. It has been a privilege to work with these exceptional minds on different projects in the past, and I have gained valuable insights and helpful suggestions

from the many discussions and conversations I had with you. I'd also like to thank Loly Ekmekjian for helping me to sort out the tedious administrative paperwork.

Moreover, I want to thank all the staff members in the KNI facility: Guy DeRose, Matt Sullivan Hunt, Nathan Lee, Burt Mendoza, Alex Wertheim. Whenever the tools went done, their timely responses made the tools up and running in the shortest time. My fabricated devices wound not have been materialized without their professionalism and meticulous teaching in the use of tools.

During my PhD career at Caltech, I'm grateful to have many friends near and far to support me. I would like to thank my friends in the Association of Caltech Taiwanese (ACT). I have enjoyed playing badminton, softball, and going snowboarding with you all very much. These fun activities I have done with you as companies have made my life at Caltech more colorful. I would also like to thank my friends both in other places and in Taiwan as they have continued to provide me with warm and family-like support outside of my academic life at Caltech.

Last but not the least, I would like to thank my parents who have given their endless support and unconditional love at every moment of my life. Furthermore, thanks to my fiancé, Jennifer Liu. I'm so lucky to have met someone so special and who I can share my ups and downs with. I could not have come this far without your constant reassurance and comfort.

ABSTRACT

Graphene, a single layer of carbon atoms forming a honeycomb lattice structure, has been considered a wonder material for both scientific research and technological applications. Structural distortions in nano-materials can induce dramatic changes in their electronic properties. In particular, strained graphene can result in both charging effects and pseudo-magnetic fields, so that controlled strain on a perfect graphene lattice can be tailored to yield desirable electronic properties.

In the first part of this thesis (Chapter 2 to 5), we explore a new approach to manipulating the topological states in monolayer graphene via nanoscale strain engineering. By placing strain-free monolayer graphene on architected nanostructures to induce global inversion symmetry breaking, we demonstrate the development of giant pseudo-magnetic fields, global valley polarization, and periodic one-dimensional topological channels for protected propagation of chiral modes in strained graphene. We have also observed pseudo-magnetic field-induced quantum oscillations and valley Hall signals, including quantum valley Hall effect, by transport measurements at 1.8K.

The second part of this thesis focuses on the development and applications of other graphene-based nanostructures. We report PECVD techniques for the synthesis of various graphene and graphene-based nanostructures, including horizontal growth of graphene sheets, vertical growth of graphene nanostructures such as graphene nanostripes with large aspect ratios, and direct and selective deposition of multi-layer graphene on nanostructured substrates. By properly controlling the gas environment of the plasma, it is found that no active heating is necessary for the PECVD growth processes and that high-yield growth can take place in a single step on a variety of surfaces, including metallic, semiconducting, and insulating materials.

PUBLISHED CONTENT AND CONTRIBUTIONS

Parts of this thesis have been drawn from the following publications with permission from the publisher:

Chen-Chih Hsu*, Marcus L. Teague*, Jaiqing Wang*, Nai-Chang Yeh, "Nanoscale Strain Engineering of Giant Pseudo-Magnetic Fields, Valley Polarization and Topological Channels in Graphene", *In preparation*, 2019 (*****Equal author contributors)
C.-C. H. conceived the experiment along with co-authors, designed and fabricated the samples, performed SEM and AFM measurement, and participated in writing the manuscript

Chen-Chih Hsu, Jacob D. Bagley, Marcus L. Teague, Wei-Shiuan Tseng, Kathleen L. Yang, Yiran Zhang, Yiliang Li, Yilun Li, James M. Tour, Nai-Chang Yeh, "High-yield Single-step Catalytic Growth of Graphene Nanostripes by Plasma Enhanced Chemical Vapor Deposition", *Carbon* **129**, 527–536 (2018).
DOI: 10.1016/j.carbon.2017.12.058
C.-C. H. participated in the conception of the project, designed the experiment, synthesized the sample, and performed some of the experimental characterizations. The manuscript was prepared by C.-C. H. with input from co-authors.

Nai-Chang Yeh, **Chen-Chih Hsu**, Jacob D. Bagley, W.-S. Tseng, "Single-step Growth of Graphene and Graphene-based Nanostructure by Plasma-enhanced Chemical Vapor Deposition", Nanotechnology, 30, 162001, (2019)
DOI: 10.1088/1361-6528/aafdbf
C.-C. H. participated in the conception of the project, designed the experiment, synthesized the sample, performed some of the experimental characterizations and measurements, and assisted in writing the manuscript

Nai-Chang Yeh, **Chen-Chih Hsu**, Marcus Teague, Jaiqing Wang, David A. Boyd, Chien-Chang Chen, "Nano-scale Strain Engineering of Graphene and Graphene-based Devices", *Acta Mech. Sin.* **32**, 497–509 (2016)
DOI: 10.1007/s10409-015-0548-9
C.-C. H. participated in the conception of the project, designed the experiment, synthesized the sample, performed some of the experimental characterizations and measurements, and assisted in writing the manuscript.

David. A. Boyd, Wei-Hsiang Lin, **Chen-Chih Hsu**, M. L. Teague, C.-C. Chen, Y.-Y. Lo, W.-Y. Chan, W.-B. Su, T.-C. Cheng, C.-S. Chang, C.-I. Wu N.-C. Yeh, "Single-step Deposition of High-mobility Graphene at Reduced Temperatures", *Nature Communications* **6**, 6620 (2015)
DOI: 10.1038/ncomms7620 (2015)
C.-C. H. Participated in synthesizing the samples.

TABLE OF CONTENTS

LIST OF TABLES

LIST OF ILLUSTRATIONS

Number *Page*

Chapter 1

INTRODUCTION

1.1 Massless Dirac fermions in graphene

Graphene, a single layer of carbon atoms forming a honeycomb lattice structure, has been considered a wonder material for both scientific research and technological applications. Because of its unique atomic structure, graphene has many unique properties such as optical, electronic, thermal, and mechanical.[1–3] The crystal structure of graphene is shown in Fig. 1.1. The Bravais lattice is triangular and the lattice vectors are[1,4]

$$\boldsymbol{a}_1 = \frac{a}{2}\left(3, \sqrt{3}\right), \qquad \boldsymbol{a}_2 = \frac{a}{2}\left(3, -\sqrt{3}\right), \tag{1.1}$$

where $a \approx 1.42$ Å is the carbon-carbon distance. There are two atoms in a unit cell of graphene. They belong to two sublattices A and B. A sublattice is surrounded by three atoms from sublattice B, and vice versa. The nearest-neighbor vectors are

$$\boldsymbol{\delta}_1 = \frac{a}{2}\left(1, \sqrt{3}\right), \qquad \boldsymbol{\delta}_2 = \frac{a}{2}\left(1, -\sqrt{3}\right), \qquad \boldsymbol{\delta}_3 = a(-1,0). \tag{1.2}$$

The reciprocal lattice vectors are

$$\boldsymbol{b}_1 = \frac{2\pi}{3a}\left(1, \sqrt{3}\right), \qquad \boldsymbol{b}_2 = \frac{2\pi}{3a}\left(1, -\sqrt{3}\right). \tag{1.3}$$

The first Brillouin zone is a hexagon and there are two inequivalent points K and K' at the corner of graphene:

$$\boldsymbol{K} = \left(\frac{2\pi}{3a}, \frac{2\pi}{3\sqrt{3}a}\right), \boldsymbol{K'} = \left(\frac{2\pi}{3a}, -\frac{2\pi}{3\sqrt{3}a}\right). \tag{1.4}$$

Using the tight-binding model and considering only nearest-neighbor hopping, the tight-binding Hamiltonian is described by the 2×2 matrix

$$H(\boldsymbol{k}) = \begin{pmatrix} 0 & tS(\boldsymbol{k}) \\ tS^*(\boldsymbol{k}) & 0 \end{pmatrix}, \tag{1.5}$$

where $\boldsymbol{k}$ is the wave vector and

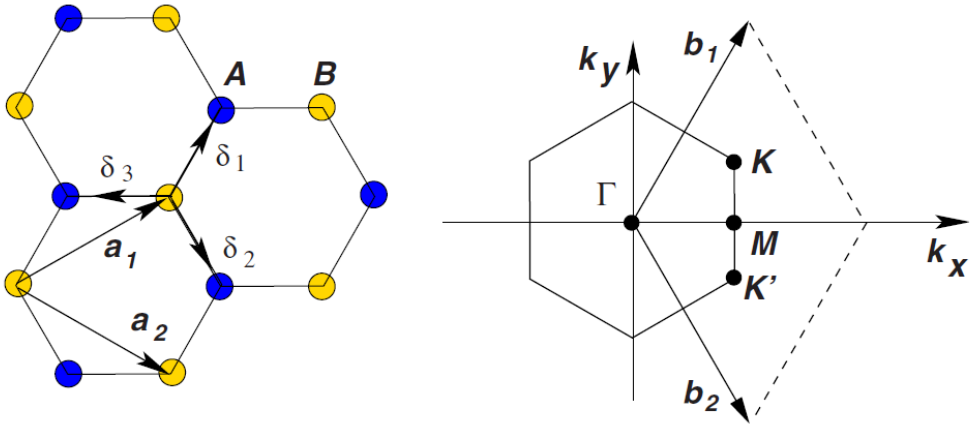

Figure 1.1. (Left) graphene honeycomb lattice with two sublattices A and B per unit cell. $\boldsymbol{a_1}$ and $\boldsymbol{a_2}$ are the lattice unit vectors, and $\boldsymbol{\delta_i}$, i=1,2,3 are the nearest-neighbor vectors. (Right) Corresponding Brillouin Zone. K and K′ points are Dirac points. Adapted from [4]

the energy bands have the form.[4,5]

$$E(\boldsymbol{k}) = \pm t|S(\boldsymbol{k})| = \pm t\sqrt{3 \pm f(\boldsymbol{k})}, \tag{1.7}$$

where $t \approx 2.8$ eV is the nearest-neighbor hopping energy and

$$f(\boldsymbol{k}) = 2\cos\left(\sqrt{3}k_y a\right) + 4\cos\left(\frac{\sqrt{3}k_y a}{2}\right)\cos\left(\frac{3k_x a}{2}\right). \tag{1.8}$$

At low energy, we can use Taylor's expansion on the Hamiltonian around the two inequivalent K and K'. The Hamiltonian has the form

$$H_{K,K'}(\boldsymbol{q}) = \hbar v_F \begin{pmatrix} 0 & q_x \mp iq_y \\ q_x \pm iq_y & 0 \end{pmatrix} = \hbar v_F \boldsymbol{\sigma}\cdot\boldsymbol{q}, \tag{1.9}$$

$$E(q) = \pm\hbar v_F|\boldsymbol{q}|, \tag{1.10}$$

where $\boldsymbol{q} = \boldsymbol{k} - \boldsymbol{K}$ and $\boldsymbol{k} - \boldsymbol{K'}$ is the momentum measured relatively to the Dirac points, $v_F = \frac{3at}{2} \approx 1 \times 10^6$ m/s is the Fermi velocity, and $\boldsymbol{\sigma}$ represents Pauli spin matrices:

$$\sigma_x = \begin{pmatrix} 0 & 1 \\ 1 & 0 \end{pmatrix}, \quad \sigma_y = \begin{pmatrix} 0 & -i \\ i & 0 \end{pmatrix}, \quad \sigma_z = \begin{pmatrix} 1 & 0 \\ 0 & -1 \end{pmatrix}. \tag{1.11}$$

The most interesting feature of the electronic energy dispersion of graphene is its linear energy-momentum relationship with the conduction and valence bands at K and K', which

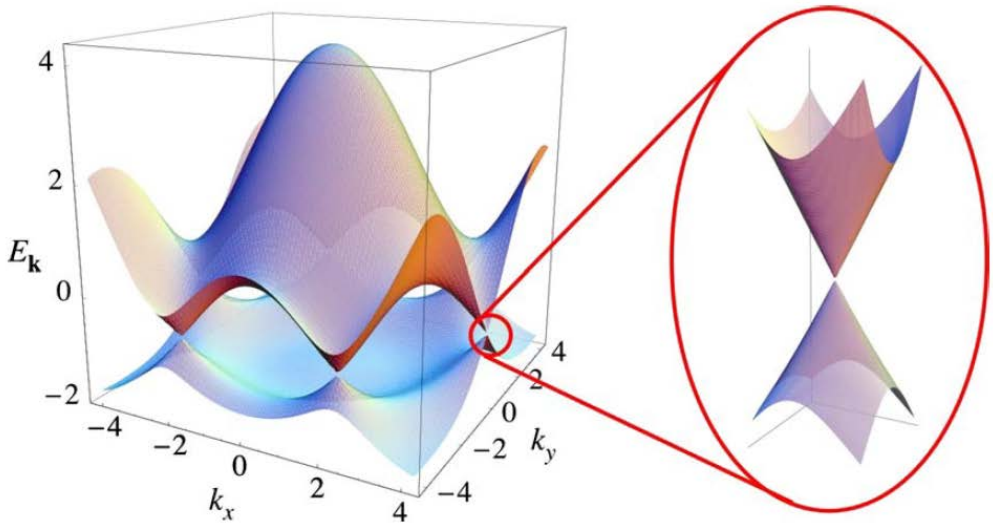

Figure 1.2. (Left) Calculated electronic dispersion in the honeycomb lattice. (Right) zoom in of the energy bands around one of the Dirac points. Adapted from [4]

are also the called Dirac points. The conical spectrum is shown in Fig. 1.2. The Hamilitonian (Eq.1.9) is an analogy to the Dirac Hamiltonian for massless fermions in two dimensions with the velocity of light c replaced by the Fermi velocity v_F ($v_F \approx \frac{1}{300}c$). Because of the linear spectrum, graphene behaves differently from materials with a parabolic-like dispersion relation.

1.2 Landau quantization in single layer graphene

One of the interesting features of Dirac fermions is their unusual phenomenon under magnetic fields. If we define a momentum $\boldsymbol{p} = \hbar\boldsymbol{q}$, the Hamiltonian can be rewritten as

$$H = v_F \boldsymbol{p} \cdot \boldsymbol{\sigma}, \tag{1.12}$$

where $\boldsymbol{p} = (p_x, p_y)$ is momentum operator and $p_x = -i\hbar\frac{\partial}{\partial x}$ and $p_y = -i\hbar\frac{\partial}{\partial y}$.

Let us consider an electron in a single graphene layer in the presence of a perpendicular magnetic field, B. In the presence of a magnetic field, we replace $\boldsymbol{p}$ by $\boldsymbol{p} + e\mathbf{A}$. So the eigenvalue equation becomes

$$(v_F(\boldsymbol{p} + e\mathbf{A}) \cdot \boldsymbol{\sigma})\psi(\boldsymbol{r}) = E\psi(\boldsymbol{r}). \tag{1.13}$$

We use the Landau gauge $\mathbf{A} = (-yB, 0,0)$ to obtain a constant magnetic field along the z-axis. This gives us

$$v_F \begin{pmatrix} 0 & p_x - ip_y - eBy \\ p_x + ip_y - eBy & 0 \end{pmatrix} \begin{pmatrix} \psi_1(\boldsymbol{r}) \\ \psi_2(\boldsymbol{r}) \end{pmatrix} = E \begin{pmatrix} \psi_1(\boldsymbol{r}) \\ \psi_2(\boldsymbol{r}) \end{pmatrix}. \tag{1.14}$$

Then we have the following two equations

$$v_F(p_x - ip_y - eBy)\psi_2(\boldsymbol{r}) = E\psi_1(\boldsymbol{r}) \tag{1.15}$$

$$v_F(p_x + ip_y - eBy)\psi_1(\boldsymbol{r}) = E\psi_2(\boldsymbol{r}). \tag{1.16}$$

For such a gauge, $[H, p_x] = 0$ and p_x is a good quantum number. We can assume the solutions $\psi_1(\boldsymbol{r}) = e^{ikx}u_1(y)$ and $\psi_2(\boldsymbol{r}) = e^{ikx}u_2(y)$ then results in two equations

$$v_F\left(\hbar k - \hbar\frac{d}{dy} - eBy\right)u_2(\boldsymbol{y}) = Eu_1(\boldsymbol{y}) \tag{1.17}$$

$$v_F\left(\hbar k + \hbar\frac{d}{dy} - eBy\right)u_1(\boldsymbol{y}) = Eu_2(\boldsymbol{y}) \tag{1.18}$$

Plugging Eq. 1.18 into Eq. 1.17, we have

$$v_F^2\left(-\hbar^2\frac{d^2}{dy^2} + e^2B^2\left(y - \frac{\hbar k}{eB}\right)^2 - \hbar eB\right)u_2(\boldsymbol{y}) = E^2u_2(\boldsymbol{y}). \tag{1.19}$$

If we define $\frac{1}{2m} \equiv v_F^2, \omega = 2eBv_F^2$, then the equation becomes

$$\left(-\frac{\hbar^2}{2m}\frac{d^2}{dy^2} + \frac{1}{2}m\omega^2\left(y - \frac{\hbar k}{eB}\right)^2 - \frac{1}{2}\hbar\omega\right)u(y) = E^2u(y). \tag{1.20}$$

This is a harmonic oscillator equation with eigenenergy energy E^2 instead of $E$and a constant $C = -\frac{1}{2}\hbar\omega$ of the left-hand side. So the energies of Eq. 1.20 are

$$E^2 = \left(n + \frac{1}{2}\right)\hbar\omega + C = n\hbar\omega = 2n\hbar eBv_F^2, \tag{1.21}$$

where n = 1, 2, 3…So the Landau levels can be written as

$$E_n = sgn(n)\sqrt{2e\hbar v_F^2|n|B}, \tag{1.22}$$

where $n > 0$ is for electron Landau levels and $n < 0$ is for hole Landau levels.

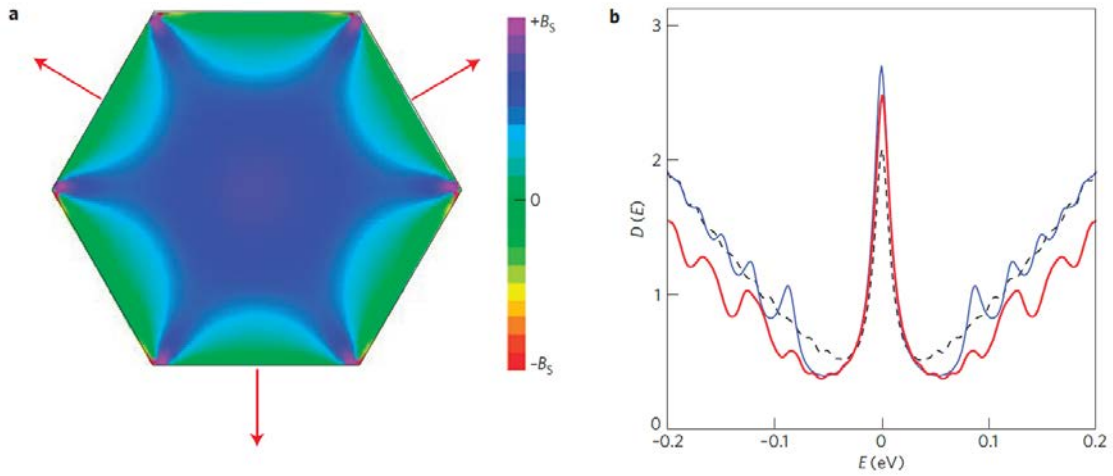

Figure 1.3. (a) Stretching graphene samples along ⟨100⟩ axes gives rise to fairly uniform pseudo-magnetic field at the center. (b) Density of states of unstrained graphene (black curve). Density of states of strained graphene (red and blue curve). Landau quantization induced by pseudo-magnetic field is shown on both curves. Images were taken from [6]

We note that the Landau level energy depends on $\sqrt{|n|}$ and $\sqrt{B}$, instead of a linear dependence for a conventional 2D electron gas with parabolic bands. Moreover, the lowest Landau level is $E_0 = 0$, instead of $\frac{1}{2}\hbar\omega$ in a typical electron gas.

Besides applying real magnetic field in graphene, it is well established that lattice structural distortions of graphene lattice can result in local strains and induce pseudo-magnetic fields and Landau levels. It has also been theoretically proposed that certain controlled strain can induce a nearly uniform pseudo-magnetic field and produce pseudo-magnetic quantum Hall effect.[6] Fig. 1.3 shows stretching graphene along the ⟨100⟩ axes can induce relatively uniform B_s in the center and lead to Landau levels in the density of states. This prediction was first observed via STM/STS studies of graphene nanobubble grown on Pt(111) substrates with pseudo fields approaching ~ 300 T.[7] This opens up the possibility of tuning the electronic properties of graphene by modifying the structural distortions of graphene by strain engineering.

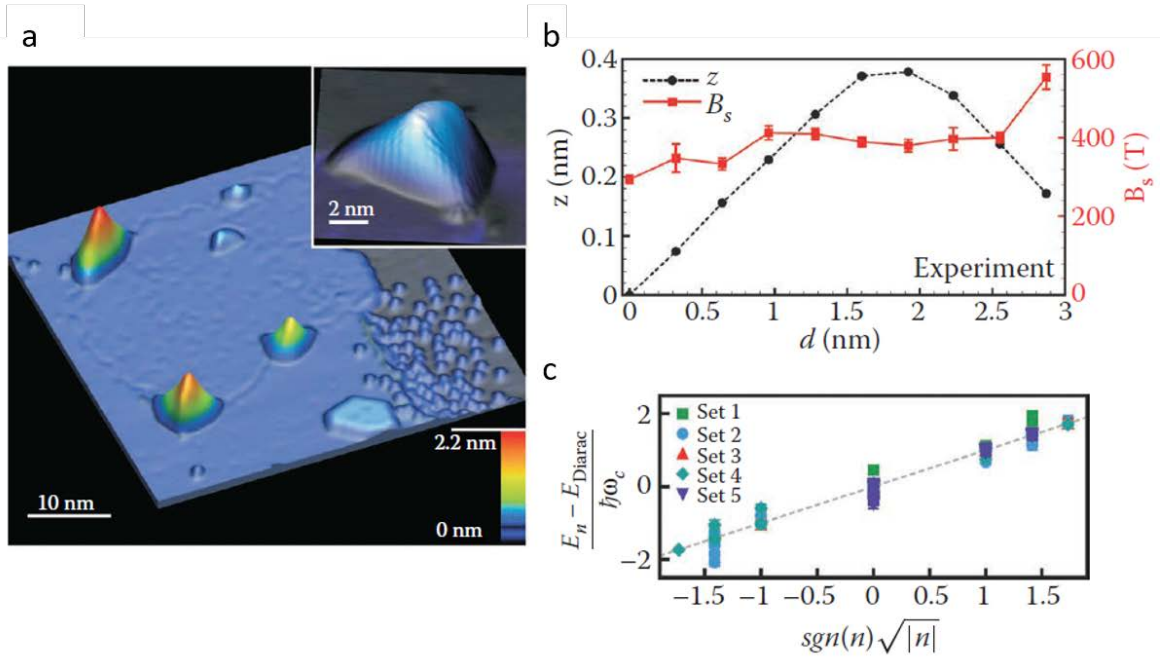

Figure 1.4. (a) Graphene nanobubbles on Pt(111). (b) Experimental topographic line scan and experimentally determined B_s profile (c) Normalized peak energy versus $sgn(n)\sqrt{|n|}$. Adapted from [7]

1.3 Synthesis of graphene and graphene-based nanostructures by plasma-enhanced chemical vapor deposition

Since the first experimental isolation of graphene in 2005, intense research of graphene worldwide has shown great promises for a wide range of technological applications because of its superior properties. One of the major challenges is how to fabricate continuous and large areas of graphene films for industrial applications. On the other hand, the compatibility of the graphene growth process with CMOS technologies is also critical to the realization of graphene-based nanoelectronic and optoelectronic applications. One possible solution is to use the plasma-enhanced chemical vapor deposition (PECVD) technique to synthesize graphene-based materials. PECVD provides a rich chemical environment, including a mixture of radicals, molecules and ions from hydrocarbon precursors, which enables graphene growth on different materials at lower temperatures and faster growth than typical thermal chemical vapor deposition. This thesis will describe various PECVD techniques that we developed for synthesis of various graphene and graphene-based nanostructures,

including horizontal growth of monolayer and multilayer graphene sheets, vertical growth of graphene nanostripes with large aspect ratios, as well as the selective growth of graphene on nanostructures in real industrial semiconductor wafers.

1.4 The Scope of this Thesis

The remaining parts of this thesis are structured as follows. The first part (Chapter 2 to Chapter 5) focuses on strain-engineering of giant pseudo-magnetic fields and valley-polarization. In Chapter 2 we introduce the basic concepts of Berry curvature and Berry phase, the effect of strain on Dirac fermions of graphene, and Raman spectroscopy of graphene. In Chapter 3 we present a new method for synthesizing nearly strain-free single-layer graphene on Cu at low temperature by plasma-enhanced chemical vapor deposition. The reproducibility and scalability of our PECVD synthesis of nearly strain-free graphene provides a platform for designing and controlling the strain in graphene, thereby tuning electronic properties of graphene on demand. In Chapter 4, we demonstrate the feasibility of nanoscale strain engineering graphene with the help of both theoretical simulation and empirical development of PECVD-grown graphene on different nanoparticles and nanostructured substrates. In Chapter 5, we report electrical transport measurements of graphene devices and demonstrate the realization of global valley polarization and periodic one-dimensional topological channels in strained graphene. These results suggest a promising pathway for realizing scalable graphene-based valleytronic devices.

The second part of this thesis concentrates on the development and applications of other graphene-based nanostructures (Chapter 6 and Chapter 7). In Chapter 6, we report a single-step growth process of graphene nanostripes (GNSPs) by adding certain substituted aromatics as precursors during the PECVD. Studies of the Raman spectra, scanning electron microscope (SEM) and transmission electron microscope (TEM) images, energy-dispersive X-ray spetrscopy (EDX), and electrical conductivity of these GNSPs as functions of the growth parameters confirm high-quality GNSPs. Chapter 7 is devoted to the development and characterization of graphene selectively growth on nanostructures of realistic industrial semiconductor wafers by PECVD.

Finally, we summarize in Chapter 8 the key results of this thesis and present an outlook for new directions and challenges. Detailed experimental methods for this work are described in the Appendix.

Chapter 2

STRAIN-ENGINEERING THE GAUGE POTENTIAL OF GRAPHENE AND GRAPHENE RAMAN SPECTROSCOPY

2.1 Introduction

It has been well recognized that the Berry phase of electronic wave functions can have a profound effect on the physical properties of materials.[8–10] For instance, the Berry phase is known to be responsible for various (quantum, anomalous, spin, and valley) Hall effects,[10–13] which can be understood by considering the semiclassical equations of motion for particles in a crystal.

In this section, we introduce the basic concepts of the Berry phase and Berry curvature. Then we discuss how the distortion-induced strain in graphene lattice can give rise to the scattering scalar potential and gauge potential in graphene. Finally, we introduce the graphene Raman spectroscopy and how strain effects on graphene can be determined by examining the Raman spectroscopy.

2.2 Berry Phase Effects on Graphene

2.2.1 Basic concepts of Berry phase and Berry curvature

Consider a Hamiltonian that depends on a set of time dependent parameters denoted by $\boldsymbol{R} = (R_1, R_2, \dots)$, i.e.,

$$H = H(\boldsymbol{R}), \boldsymbol{R} = \boldsymbol{R}(t). \tag{2.1}$$

The eigenstates for all values of the parameters can be expressed as follows:

$$H(\boldsymbol{R})|n(\boldsymbol{R})\rangle = E_n(\boldsymbol{R}))|n(\boldsymbol{R})\rangle. \tag{2.2}$$

Next, we consider an adiabatic process in which $\boldsymbol{R}(t)$ changes slowly in time. The wave function $|\psi_n(\boldsymbol{t})\rangle$ must satisfy the quantum adiabatic theorem with several phase factors. We can write the state at time t as

$$|\psi_n(\boldsymbol{t})\rangle = e^{i\gamma_n(t)} exp\left[-\frac{i}{\hbar}\int_0^t dt' E_n\left(\boldsymbol{R}(t')\right)\right]\left|n\big(\boldsymbol{R}(t)\big)\right\rangle, \tag{2.3}$$

where γ_n is known as the geometric phase or Berry phase and the second exponential is known as the dynamic phase. Inserting Eq. (2.3) into the time-dependent Schrödinger equation

$$i\hbar\frac{\partial}{\partial t}|\psi_n(\boldsymbol{t})\rangle = H\big(\boldsymbol{R}(\boldsymbol{t})\big)|\psi_n(\boldsymbol{t})\rangle, \tag{2.4}$$

and multiplying it from the left by $\langle n\big(\boldsymbol{R}(t)\big)|$, γ_n can be rewritten as a path integral in the parameter space

$$\gamma_n = \int_C d\boldsymbol{R}\cdot\boldsymbol{A}_n(\boldsymbol{R}), \tag{2.5}$$

where $\boldsymbol{A}_n(\boldsymbol{R})$ is called the Berry connection or the Berry vector potential

$$\boldsymbol{A}_n(\boldsymbol{R}) = i\left\langle n\big(\boldsymbol{R}(t)\big)\left|\frac{\partial}{\partial\boldsymbol{R}}\right|n(\boldsymbol{R})\right\rangle. \tag{2.6}$$

Eq. (2.5) shows that there is an additional phase term γ_n in the wave function during the adiabatic evolution. In analogy to electrodynamics, we can define a gauge field Ω_n called the Berry curvature, which is the curvature of Berry's connection.

$$\Omega_n(\boldsymbol{R}) = \nabla_R\times\boldsymbol{A}_n(\boldsymbol{R}). \tag{2.7}$$

Then according to Stokes's theorem, the Berry phase can be written as a surface integral

$$\gamma_n = \int_S d\boldsymbol{S}\cdot\Omega_n(\boldsymbol{R}), \tag{2.8}$$

where S is an arbitrary surface enclosed by the path C.

If $\boldsymbol{R}(t)$ is three-dimensional, then the Berry curvature is an analogy to the magnetic field in the parameter space. For the same reason as the magnetic field is, Berry curvature is gauge invariant.

2.2.2 Berry phase in Bloch bands

Here we consider the Berry phase in crystalline solids because the band structure of crystals is a natural platform to study the Berry phase. According to the Bloch theorem, the eigenstates of a periodic potential $V(\boldsymbol{r}+\boldsymbol{a}) = V(\boldsymbol{r})$ satisfy the following boundary condition:

$$\psi_{n\boldsymbol{k}}(\boldsymbol{r}+\boldsymbol{a}) = e^{i\boldsymbol{k}\cdot\boldsymbol{a}}\psi_{n\boldsymbol{k}}(\boldsymbol{r}) \tag{2.9}$$

$$\psi_{n\boldsymbol{k}}(\boldsymbol{r}) = e^{i\boldsymbol{k}\cdot\boldsymbol{r}}u_{n\boldsymbol{k}}(\boldsymbol{r}), \tag{2.10}$$

where n is the band index, $\boldsymbol{a}$ is the Bravais lattice vector, $\hbar\boldsymbol{k}$ is the crystal momentum, and the Bloch periodic function satisfy $u_{n\boldsymbol{k}}(\boldsymbol{r}) = u_{n\boldsymbol{k}}(\boldsymbol{r}+\boldsymbol{a})$. Because $\boldsymbol{k}$ dependence of the basis function is involved in the Block problem, we expect to see Berry phase effects in crystals. For example, if $\boldsymbol{k}$ is only varied in the momentum space, then the Bloch state will pick up a Berry phase.

From Eq. (2.6) and (2.7), we can also define the Berry curvature of the energy bands by

$$\Omega_n(\boldsymbol{k}) = \nabla_{\boldsymbol{k}} \times i\langle u_n(\boldsymbol{k})|\nabla_{\boldsymbol{k}}|u_n(\boldsymbol{k})\rangle. \tag{2.11}$$

The Berry curvature $\Omega_n(\boldsymbol{k})$ is an intrinsic property of the band structure because it only depends on the wave function. It is nonzero in the materials if the crystal has broken time-reversal or inversion symmetry. Berry curvature plays an important role in the dynamics of Bloch electrons. In the following we'd like to discuss the effects on transport properties of crystals.

2.2.2 Anomalous velocity and symmetry consideration

Consider the semiclassical dynamics of Bloch electron's equations of motion for particles in a crystal:

$$\boldsymbol{v}_n(\boldsymbol{k}) = \frac{\partial E_n(\boldsymbol{k})}{\hbar\,\partial\boldsymbol{k}} - \dot{\boldsymbol{k}} \times \Omega_n(\boldsymbol{k}), \tag{2.12}$$

$$\hbar\dot{\boldsymbol{k}} = e\mathbf{E} + e\boldsymbol{v}_n(\boldsymbol{k}) \times \mathbf{B}, \tag{2.13}$$

where $\boldsymbol{v}_n(\boldsymbol{k})$ and $E_n(\boldsymbol{k})$ denote the particle velocity and energy of a crystalline momentum $\boldsymbol{k}$, **E** and **B** represent the applied electric and magnetic fields, respectively. In addition to the usual band dispersion contribution, the Berry curvature of Bloch bands also contributes to an extra term $\dot{\boldsymbol{k}} \times \Omega_n(\boldsymbol{k})$ to $\boldsymbol{v}_n$, which is known as the anomalous velocity. Because the anomalous velocity is always transverse to the electric field, this will give rise to a Hall current.

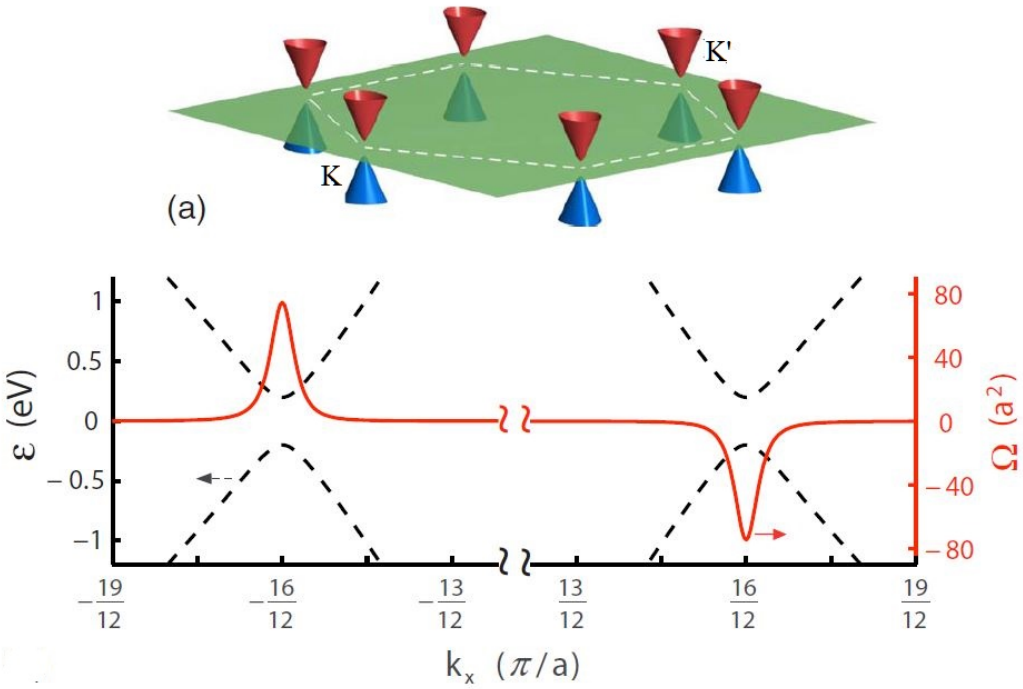

Figure 2.1 Energy bands (top panel) and Berry curvature of the conduction band (bottom panel) of a graphene sheet with broken inversion symmetry. The first Brillouin zone is outlined by the dashed lines, and two inequivalent valleys are labeled as K and K′. Adapted from [10].

Next, it's important to understand what conditions the Berry curvature term cannot be neglected. Berry curvature $\Omega_n(\boldsymbol{k})$ can be obtained by symmetry analysis. Eq. (2.7) should be invariant under time-reversal and spatial inversion operation. Under time-reversal symmetry, $\boldsymbol{v}_n(\boldsymbol{k})$, $\boldsymbol{k}$ change the sign while **E** is fixed. Under spatial inversion, $\boldsymbol{v}_n(\boldsymbol{k})$, $\boldsymbol{k}$, and **E** change sign. Therefore, if the system has time-reversal symmetry, Eq. (2.7) requires that

$$\Omega_n(-\boldsymbol{k}) = -\Omega_n(\boldsymbol{k}). \tag{2.14}$$

If the system has spatial inversion symmetry, then

$$\Omega_n(-\boldsymbol{k}) = \Omega_n(\boldsymbol{k}). \tag{2.15}$$

As a result, Berry curvature is zero if crystals have time-reversal and spatial inversion symmetry simultaneous. However, for systems with either time-reversal or inversion symmetries broken, we need to include the anomalous velocity to fully describe the

electron equation of motion. For $\mathbf{B} = 0$, the anomalous Hall effect (AHE) can appear in the presence of spontaneous magnetization, whereas either spin Hall effect (SHE) or valley Hall effect (VHE) can occur due to broken inversion symmetry.

Take graphene as an example, the Berry curvature of pristine graphene is zero because of both time-reversal and inversion symmetries. However, Berry curvature becomes nonzero if we add a staggered AB sublattice potential to a single layer graphene (SLG) sheet to break the inversion symmetry.[14] Fig. 2.1 shows the energy band and Berry curvature of this system. Berry curvature at K and K′ valley have opposite signs due to time-reversal symmetry.

2.3 Theory for strain-induced modifications to the Dirac fermions in single layer graphene

2.3.1 Introduction

In general, structural distortions in graphene may be associated with surface ripples, topological defects, adatoms, vacancies, and extended defects such as edges, cracks, and grain boundaries.[4,6,15–18] The distortion-induced strain in the graphene lattice typically gives rise to two primary effects on the Dirac fermions. One is an effective scattering scalar potential[15–17] and the other is an effective gauge potential.[6,18]

The physical causes for the strain-induced effective scalar and gauge potentials in graphene may be understood in terms of the changes in the distance or angles between the p_z orbitals that modify the hopping energies between different lattice sites, thereby giving rise to the appearance of a vector (gauge) potential $\boldsymbol{A}$ and a scalar potential ϕ in the Dirac Hamiltonian.[4,19] Under the preservation of global time-reversal symmetry, the presence of strain-induced vector potential leads to opposite pseudo-magnetic fields $\mathbf{B_s} = \nabla \times \boldsymbol{A}$ and $\mathbf{B_S^*} = \nabla \times \boldsymbol{A}^* = -\nabla \times \boldsymbol{A} = -\mathbf{B_s}$ for the two inequivalent valleys at K and K′, respectively. On the other hand, the presence of a spatially varying scalar potential can result in local charging effects known as self-doping.[4]

2.3.2 Overview of the effect of strain on Dirac fermions of graphene

The disorder generally induces two types of contributions to the original Dirac Hamiltonian H_0. One is associated with the charging effect of a scalar potential, and the other is associated with a pseudo-magnetic field from a strain-induced gauge potential. For an ideal graphene sample near its charge neutral point, the massless Dirac Hamiltonian H_0 in the tight-binding approximation is given by:

$$H_0 = -t \sum_{\langle i,j\rangle,\sigma} \left(a_{i,\sigma}^{\dagger} b_{j,\sigma} + H.c.\right) - t' \sum_{\langle i,j\rangle,\sigma} \left(a_{i,\sigma}^{\dagger} a_{j,\sigma} + b_{i,\sigma}^{\dagger} b_{j,\sigma} + H.c.\right), \tag{2.16}$$

where $a_{i,\sigma}\left(a_{i,\sigma}^{\dagger}\right)$ annihilates (creates) an electron with spin σ ($\sigma = \uparrow, \downarrow$) on site $\boldsymbol{R}_i$ of the sublattice A, $b_{i,\sigma}\left(b_{i,\sigma}^{\dagger}\right)$ annihilates (creates) an electron with spin σ on site $\boldsymbol{R}_i$ of the sublattice B, $t \approx 2.8$ eV ($t' \approx 0.1$ eV) is the nearest-neighbor (next-nearest-neighbor) hopping energy for fermion hopping between different sublattices, and $H.c.$ refers to the Hermitian conjugate.[4]

The presence of lattice distortion results in a spatially varying in-plane displacement field $\boldsymbol{u}(x,y) = \left(u_x(x,y), u_y(x,y)\right)$and a spatially varying height displacement field $h(x,y)$. Therefore, in addition to changes in the distances or angles among the two-dimensional σ-bonds, distortion also induces changes in the distance or angle of the p_z orbitals. Such three-dimensional lattice distortion gives rise to the following expressions for the strain tensor components u_{ij} (where $i, j = x, y$):

$$u_{xx} \equiv \frac{\partial u_x}{\partial x} + \frac{1}{2}\left(\frac{\partial h}{\partial x}\right)^2, \quad u_{yy} \equiv \frac{\partial u_y}{\partial y} + \frac{1}{2}\left(\frac{\partial h}{\partial y}\right)^2, \quad u_{xy} \equiv \frac{1}{2}\left(\frac{\partial u_x}{\partial y} + \frac{\partial u_y}{\partial x}\right) + \frac{1}{2}\left(\frac{\partial h}{\partial x}\frac{\partial h}{\partial y}\right), \tag{2.17}$$

so that an additional perturbative Hamiltonian H' must be introduced to describe the wave-functions of Dirac fermions in distorted graphene:[4,15,16]

$$\begin{aligned} H' &= -\sum_{i,j,\sigma}\left[\delta t^{ab}\left(a_{i,\sigma}^{\dagger}\, b_{j,\sigma}\, + H.c.\right) + \delta t^{aa}\left(a_{i,\sigma}^{\dagger}\, a_{j,\sigma}\, + b_{i,\sigma}^{\dagger}\, b_{j,\sigma}\,\right)\right] \\ &= \int d^2r \sum_{\alpha=1,2}\left[\Phi(\boldsymbol{r})\Psi_{\alpha}^{\dagger}(\mathrm{r})\Psi_{\alpha}(\boldsymbol{r}) + \Psi_{\alpha}^{\dagger}(\boldsymbol{r})(\tilde{\sigma}\cdot A_{\alpha})\Psi_{\alpha}(\boldsymbol{r})\right] \\ &\equiv\ H_{\Phi} + H_{\boldsymbol{A}}, \end{aligned} \tag{2.18}$$

where δt^{ab} and δt^{aa} (= δt^{bb}) are strain-induced modifications to the nearest and next-nearest neighbor hopping energies, respectively, $\tilde{\sigma}$ represents the (2 × 2) Pauli matrices, $\Psi_{\alpha}(\boldsymbol{r})$ denotes the spinor operator for the two sublattices in the continuum limit, and H_{Φ} ($H_{\boldsymbol{A}}$) represents the strain-induced perturbation to the scalar (gauge) potential. We note that in the event of finite z-axis corrugation, the modified hopping integrals for Dirac fermions from one site to another must involve not only the in-plane orbitals but also the p_z orbitals of the distorted graphene sheet as the result of the three-dimensional distribution of electronic wavefunctions

Specifically, the strain-induced gauge potential $\boldsymbol{A} = \left(A_x, A_y\right)$ in Eq. (2.18) is related to the two-dimensional strain field $u_{ij}(x, y)$ by the following relation (with the x-axis chosen along the zigzag direction):

$$\begin{aligned} A_x &= \pm\frac{\beta}{a_0}\left(u_{xx} - u_{yy}\right), \\ A_y &= \mp 2\frac{\beta}{a_0}u_{xy}, \end{aligned} \tag{2.19}$$

where $a_0 \approx 0.142$ nm is the nearest carbon-carbon distance, and β is a constant ranging from 2 to 3 in units of the flux quantum.[4] Similarly, the compression/dilation components of the strain can result in an effective scalar potential $\Phi(x, y)$ in addition to the aforementioned pseudo-magnetic field so that there may be a static charging effect.[15–17] Here $\Phi(x, y)$ is given by:

$$\Phi(x, y) = \Phi_0\left(u_{xx} + u_{yy}\right) \equiv \Phi_0\bar{u}, \tag{2.20}$$

where $\Phi_0 \approx 3$ eV, and $\bar{u}$ is the dilation/compression strain.

By inserting the explicit expressions given in Eqs. (2.17), (2.19), and (2.20) into Eq. (2.18), we find that the excess strain components associated with the changes in the distances and angles of the p_z -orbitals may be written in forms of $\left[\left(\frac{\partial h}{\partial x}\right)^2+\left(\frac{\partial h}{\partial y}\right)^2\right]$ and $\left(\frac{\partial h}{\partial x}\right)\left(\frac{\partial h}{\partial y}\right)$, respectively. We further note that in the event of strong z-axis corrugation, the strain components resulting from the variations in the p_z -orbitals may become dominant over the in-plane strain components according to Eq. (2.17).

Thus, the total Hamiltonian for the Dirac fermions of graphene becomes $\mathrm{H} = H_0 + H' = H_0 + (H_\Phi + H_{\boldsymbol{A}})$. The physical significance of the perturbed term $H_{\boldsymbol{A}}$ is analogous to the contribution of a vector potential $\boldsymbol{A}$ in a two-dimensional electron gas that gives rise to a vertical magnetic field $\mathbf{B_s} = \nabla \times \boldsymbol{A} = B_s\hat{z}$ and the formation of quantized orbitals. In this context, the Landau levels E_n of Dirac fermions under a given B_s satisfy the following relation

$$E_n = \mathrm{sgn}(n)\sqrt{(2ev_F^2\hbar B_s)|n|}, \tag{2.21}$$

where v_F denotes the Fermi velocity of graphene and n denotes integers. Additionally, the magnetic length l_B associated with a given B_s is $l_B \equiv \sqrt{\left(\frac{\hbar}{eB_s}\right)} \sim \frac{25\ nm}{\sqrt{B_s}}$ (B_s in units of Tesla).[4] Similarly, the physical significance of the perturbed term H_Φ is analogous to the contribution from a scalar potential Φ. For strain primarily induced by corrugations along the out-of-plane (z) direction, the typical strain is of order $\bar{u} \sim \left(\frac{\Delta z}{L}\right)^2$ from Eq. (2.17), where Δz denotes the height fluctuations and L is the size of the lateral strained region. In principle, the charging effect associated with the scalar potential can be suppressed in a graphene layer suspended over metal if $\Delta z \ll l_B$.[6,18] However, for $\Delta z \sim l_B$, the strain-induced charging effect can no longer be effectively screened so that experimental observation of such an effect at the nanoscale may be expected.[20,21]

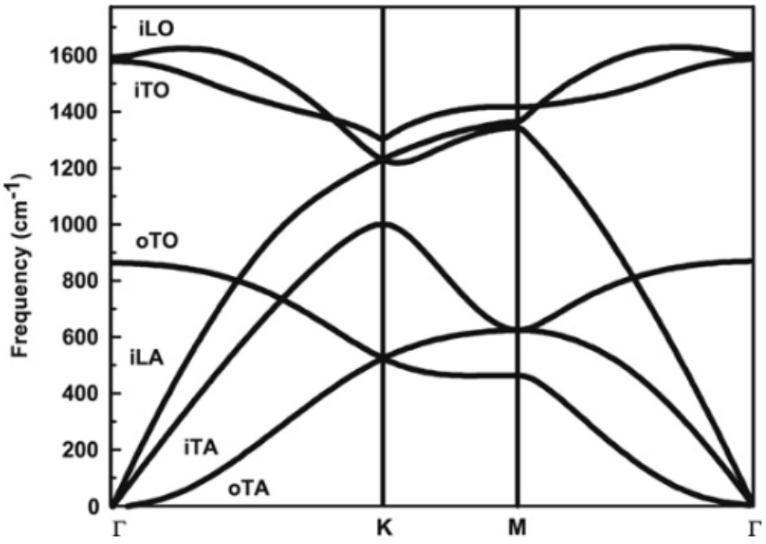

Figure 2.2 Calculated phonon dispersion relation of graphene showing the iLO, iTO, oTO, iLA, iTA, and oTA phonon branches. (From [22])

2.4 Raman spectroscopy of graphene

2.4.1 Raman spectroscopy of graphene

Raman spectroscopy has been a powerful experimental tool that can reveal numerous important characteristics of graphene samples.[22–25] Raman spectroscopic studies of graphitic samples can provide useful information about the number of layers, stacking order, disorder, as well as the behavior of electrons and phonons in the samples. To understand the Raman modes in graphene, it's important to start with the phonon dispersion of graphene. Figure 2.2 is the phonon dispersion of graphene.[22] Because the single-layer graphene unit cell has two carbon atoms, there are six phonon branches, which are three acoustic (A) and three optical (O) phonons. Two acoustic and two optical phonon branches are in-plan (i) modes. Two branches are out-of-plane (o) modes. If the direction of the vibration modes is along with the carbon-carbon bonds, the modes are known as transverse (T). If the direction of the vibration modes is perpendicular to the carbon-carbon bonds, the modes are known as longitudinal (L). In particular, iLO and iTO phonons are responsible for the main Raman bands observed in graphene.

Figure 2.3 is a representative Raman spectrum of one of our PECVD-grown graphene samples transferred onto a SiO_2/Si substrate. The most prominent features in the Raman

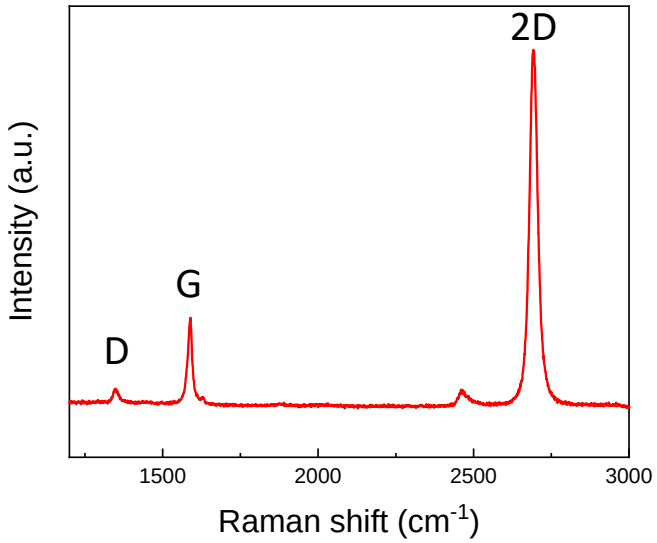

Figure 2.3 Raman spectrum of single-layer PECVD-grown graphene transferred onto a SiO_2/Si substrate.

spectra of single-layer graphene include the so-called G-band appearing at ~1582 cm^{-1} and the 2D (also known as G′) band at ~2700 cm^{-1}, using laser excitation at 2.41 eV. In the case of a disordered sample or at the edge of a graphene sample, the so-called disorder-induced D-band at around ~1350 cm^{-1} is also present. The 2D band exhibits a single Lorentzian feature with a full width at half maximum (FWHM) of ~ 28.8 cm^{-1} and the ratio of intensity of 2D band (I_{2D}) to the intensity of G band (I_G) is ~ 4, suggesting that this is a single-layer graphene.[26,27]

The G band is a first-order process that is associated with a doubly-degenerate in-plane sp^2 C-C stretching mode (iTO and iLO) in the Brillouin zone center, as shown in Fig. 2.4(a) and Fig. 2.5(a). It belongs to the E_{2g} irreducible representation at the Brillouin zone center Γ point. This band exists in all sp^2 carbon systems, including amorphous carbon, fullerene, carbon nanotube, graphene, and graphite.

The D band is a second-order process Raman processing originating from the in-plane breathing-like mode of the carbon rings, as shown in Fig 2.4 (b). It belongs to the totally

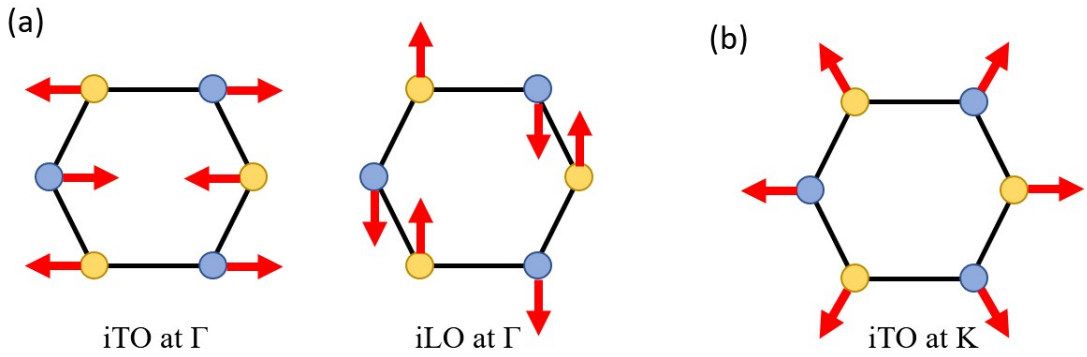

Figure 2.4 Sketch of the phonon vibrations of Raman bands in graphene. (a) G band vibration modes for the iTO and iLO phonons at the Γ point. (b) D band vibration mode for the iTO phonon at the K point.

symmetric irreducible representation A_1' at the K or (K′) point in the first Brillouin zone. It involves an elastic (defect) and an inelastic (iTO phonons) scattering processes near the K point and is only visible when there are defects and edges within the graphene, as shown in Fig. 2.5 (b).

The 2D peak (at around 2,700 cm^{-1}) also originates from a second-order process, involving two inelastic scattering process (two iTO phonons) near the K or (K′) point, so the frequency is approximate twice the D band frequency, as shown in Fig. 2.5(c). This process is known as double resonant (DR) because the incident or scattered photon and the first or second phonon scattering are resonant with electronic levels in graphene. The 2D band process can also be triple resonant, which is shown in Fig. 2.6 (b). This band is always visible even if the D peak is not visible because no defect scattering is involved.

The number of graphene layers and stacking order in multilayer graphene (MLG) can be analyzed by the linewidth and peak position of 2D mode. For instance, the 2D-band of bilayer graphene with perfect Bernal A-B stacking should be considered as the superposition of four Lorentzian peaks that correspond to four different double resonance (DR) processes associated with bilayer graphene, whereas that of trilayer graphene with A-B-A stacking would involve six Lorentzian peaks.[22] In the case of perfect three-dimensional (3D) graphite, the 2D-band consists of two Lorentzian peaks.

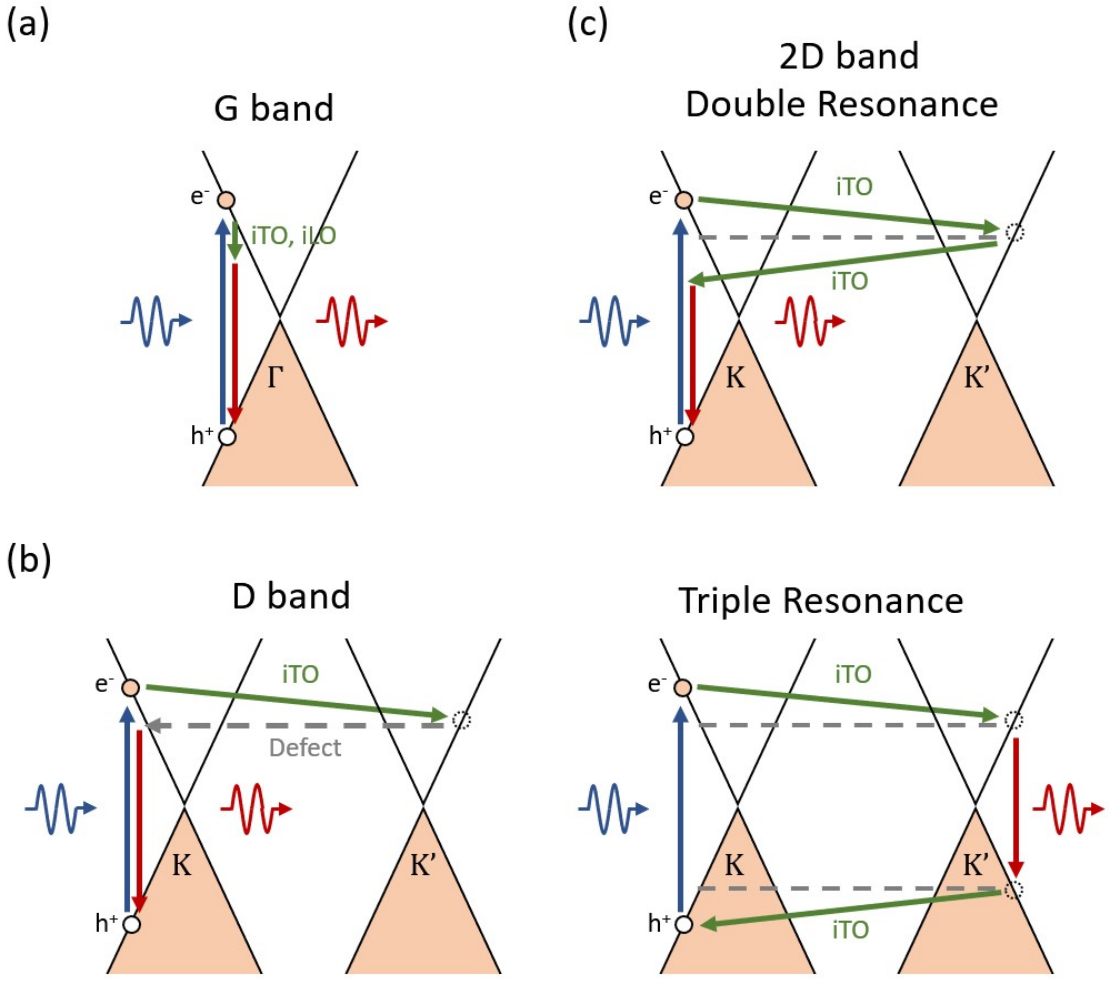

Figure 2.5 Sketch of Raman processes in graphene. (a) G band (b) D band double resonant process (c) 2D band generated through a second-order process that is double resonant (top) or triple resonant (bottom).

2.4.2 Raman spectroscopy of turbostratic graphene

The number of graphene layers can only be determined by Raman spectroscopy for graphene samples with AB Bernal stacking. Mechanical exfoliation graphene made from HOPG has predominantly AB stacking; however, it's not always the case for graphene samples made by other synthesis methods.

Turbostratic graphene is a multilayer graphene sample with each layer rotating randomly against each other along the c axis. The interlayer spacing (> 0.342 nm) is larger than that

for crystalline graphite (c/2 = 0.335 nm). Because of the interaction between each layer is weaker, the Raman spectrum of turbostratic graphene is very similar to the single-layer graphene. But the 2D band is broadened due to the random angle associated with each graphene layer.

2.4.3 Raman spectra for strained graphene

The structural distortion-induced strain effects on graphene can also be determined by examining the Raman spectroscopy. Specifically, the biaxial strain $(\epsilon_{ll} + \epsilon_{tt}) \approx (u_{xx} + u_{yy})$ of graphene can be estimated by considering the Raman frequency shifts $\Delta\omega_m \equiv (\omega_m - \omega_m^0)$. and the Gruneisen parameter γ_m^{biax}:[26,28]

$$\gamma_m^{\text{biax}} = \frac{\Delta\omega_m}{\omega_m^0(\epsilon_{ll} + \epsilon_{tt})}, \tag{2.20}$$

where *m* (= G, 2D) refers to the specific Raman mode. Using $\gamma_{2D}^{\text{biax}} = 2.7$ and $\gamma_G^{\text{biax}} = 1.8$, we can determine the average strain of graphene samples prepared under different conditions. As exemplified in Fig. 2.7 for the comparison of the Raman spectroscopy taken on thermal CVD-grown graphene and a low-temperature PECVD grown graphene, we found a general trend of downshifted G-band and 2D-band frequencies for all PECVD-grown graphene relative to thermal CVD-grown graphene on the same substrate, indicating reduced strain in PECVD grown graphene.[29]

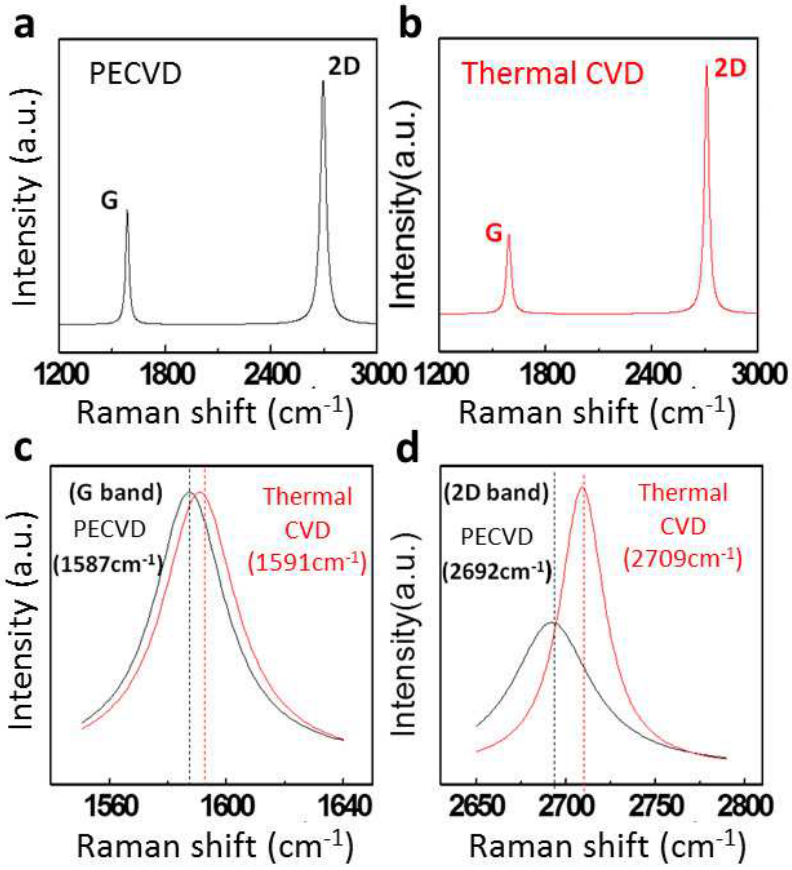

Figure 2.6 Determining the strain effects in graphene from Raman spectroscopy: (a) A representation Raman spectrum (laser wavelength 514 nm) of a PECVD-grown graphene sample. (b) A representative Raman spectrum of a thermal CVD-grown graphene sample. (c) Comparison of the G-band frequency of the PECVD- and thermal-grown graphene showing a downshifted G-band and therefore reduced strain in the PECVD-grown graphene. (d) Comparison of the 2D-band frequency of the PECVD- and thermal CVD-grown graphene showing a downshifted 2D-band and therefore reduced strain in the PECVD-grown graphene, consistent with the finding shown in (c). Adapted from [30]

Chapter 3

SINGLE-STEP GROWTH OF GRAPHENE BY PLASMA-ENHANCED CHEMICAL VAPOR DEPOSITION

3.1 Introduction

The realization of many promising technological applications of graphene and graphene-based nanostructures depends on the availability of reliable, scalable, high-yield, and low-cost synthesis methods. Plasma enhanced chemical vapor deposition (PECVD) has been a versatile technique for synthesizing many carbon-based materials, because PECVD provides a rich chemical environment, including a mixture of radicals, molecules, and ions from hydrocarbon precursors, which enables graphene growth on a variety of material surfaces at lower temperatures and faster growth than typical thermal chemical vapor deposition. In this chapter, we review recent advances in the PECVD techniques for the synthesis of graphene on different metal substrates. We also developed a new growth method based on microwave (MW) PECVD. By properly controlling the gas environment of the plasma, it is found that no active heating is necessary for the PECVD growth processes and that high-yield graphene growth can take place in a single step on a variety of surfaces.

3.2 Current techniques used for the synthesis of graphene

To date, several methods have been developed for the mass-production of graphene, which includes liquid-phase exfoliation of graphite,[31,32] synthesis on SiC,[33,34] thermal chemical vapor deposition (T-CVD),[35] and PECVD.[29,36] Among these different synthesis methods, T-CVD has been developed for growing large-area graphene with reasonably high quality. However, T-CVD growth of graphene generally requires multiple processing steps and a relatively long time in both substrate preparation and graphene growth.[37–39] Moreover, high-temperature processes (~1000 °C) in the T-CVD synthesis are incompatible with applications relevant to the semiconducting industry, and the high thermal budget adds further constraints on mass production. Recently, oxygen and oxygen-containing species

were also found to play an important role in graphene synthesis, such as graphene nucleation, graphene shape, and bilayer and multilayer graphene (MLG) formation.[37,40–42] In contrast to the T-CVD growth method, PECVD has proven to be a versatile approach that offers a number of advantages.[29,36] PECVD has been widely used for synthesizing many carbon-based materials, such as diamonds, graphene, vertically oriented graphene nano-walls and nano-sheets, and carbon nanotubes (CNTs). The plasma can provide a rich chemical environment, including a mixture of free radicals, photons, energetic electrons, excited molecules, and active ions. This environment enables graphene growth on different surfaces at relatively lower temperatures and faster growth than T-CVD.[29,36] Additionally, PECVD techniques can be employed for fast and large-scale functionalization of graphene and related materials, which is a versatile approach that further broadens the scope of graphene-based applications. These advantages make PECVD growth of graphene and graphene-related nanostructures highly attractive and have been considered as a promising technique to improve the compatibility of graphene growth with semiconducting manufacturing processes.

3.3 Reviews of PECVD growth of graphene sheets on transition metal substrates

Generally speaking, graphene growth could be achieved at a reduced temperature by PECVD on different transition metal substrates such as Co,[43,44] Ni,[45–48] and Cu.[29,47,49–55] Among the pioneering works, Woo et al grew high-quality and uniform graphene films at 850 °C in a remote RF-PECVD system.[45] SEM images and electron backscattering diffraction map showed highly crystallized graphene with few atomic defects and well-ordered structure. The carrier mobility was ~ 4500 $cm^2V^{-1}s^{-1}$ at room temperature. Nandamuri et al also employed an RF-PECVD system to synthesize MLG on Ni (111) single crystals and polycrystalline Ni foils in about one-minute growth time.[46] The size of the graphene domains was found to be consistent with the dimensions of the flat grain Ni surfaces, which ranged from ~1 μm to ~20 μm, suggesting epitaxial growth on the Ni polycrystalline substrate. Subsequently, SLG was successfully grown on Ni foil by MWPECVD with the growth temperature from 450 °C to 750 °C,[48] and the number of graphene layers could also be controlled by changing the gas mixture of H_2/CH_4 ratio. Peng

et al demonstrated the synthesis of few-layer graphene sheets on an ultra-thin Ni film coated on SiO2/Si substrate using low-temperature RF-PECVD without introducing any H2,[48] where the number of graphene layers could be controlled by the thickness of Ni film at 475 °C. In general, it is found that the use of Ni substrates for graphene synthesis by PECVD methods typically yields MLG due to the high carbon solubility in Ni, similar to the findings in T-CVD graphene growth.

On the other hand, Cu foils have been widely used for graphene growth because of the low cost and commercial availability. Moreover, Cu is an excellent substrate for synthesizing high-quality SLG due to the low carbon solubility and its catalytic nature. With the help of plasma, hydrocarbon precursors can break apart more easily so that carbon atoms and radicals can directly assemble into graphene on the Cu surface. For example, Kim et al have deposited large-area graphene-like films on Al and Cu foils using an MW assisted surface wave plasma CVD (MW-SWP-PECVD) method at a substrate temperature ∼400 °C .[56] However, graphene films grown by MW-SWP-PECVD required high power (3–4.5 kW), and their Raman spectroscopy exhibited large D and D′ peaks, which indicated lots of defects and boundaries. Similarly, Terasawa et al investigated the growth mechanism of graphene in varying the growth conditions by an RF-PECVD.[57] When the substrate temperature was kept at 500 °C, carbon nano-walls (CNWs) were found on the Cu surface. On the other hand, as the substrate temperature was raised to 900 °C, SLG was fabricated with a small D peak. It was found that the growth of SLG was activated by the Cu catalytic surface at high substrate temperature, whereas the growth of CNWs was initiated by the hydrocarbon radicals in the plasma.

In the following years, the growth of graphene by the PECVD methods faced two major challenges. One was to fabricate continuous and large areas of graphene films, and the other was to improve the quality of the PECVD-grown graphene. Yamada et al combined a PECVD process at a low substrate temperature of ∼380 °C and a roll-to-roll process for mass production of graphene.[50] Although the resulting graphene structures were defective, Raman spectra along the width direction of the Cu foil was found to be uniform. This result suggested

that roll-to-roll growth by the PECVD method appeared promising for realizing continuous and large-area graphene films in industrial production.

Meanwhile, many research groups have experimented with different PECVD systems and growth conditions to improve the quality of graphene grown on Cu substrates. Kim et al demonstrated the synthesis of SLG on polycrystalline Cu foils under various Ar/CH_4 and H_2/CH_4 gas ratios for substrate temperatures ranging from 700 °C to 830 °C.[51] The grain size of graphene was found to range from ~0.4 to ~3 μm and the shape was arbitrary or rounded hexagonal. In particular, they found out even without any H_2 flow, methane alone could still provide enough hydrogen species for single-layer graphene synthesis on Cu by PECVD, which implied that methane could be the source for both hydrogen and carbon. Similar graphene films were synthesized using remote MWPECVD at a substrate temperature of 600 °C with various ratios of methane and hydrogen mixture.[52] The remote plasma setup used in the work could reduce defects incurred from ion bombardment in the plasma. Moreover, it was found that with increasing H_2 flow rate, Raman spectra showed higher-quality graphene films with larger 2D-to-G and smaller D-to-G intensity ratios as well as narrower FWHMs of the 2D band. Nang et al also demonstrated graphene synthesis on Cu foils by means of inductively-coupled plasma chemical vapor deposition (IC-PECVD).[54] Graphene quality was found to improve with increasing growth time and plasma power. In 2015, Laan et al used RF-PECVD to grow SLG at substrate temperatures as low as 220 °C.[55] These graphene films could be easily removed from Cu foils and transferred to other substrates by dipping the sample into water.

In Table 3.1 we summarize the aforementioned PECVD growth conditions on metallic substrates and the resulting graphene characteristics from measurements of Raman spectroscopy, sheet resistance, and electrical mobility. For polycrystalline graphene samples, the average in-plane sp^2 crystallite size (L_a) of the samples may be estimated by using the intensity ratio (I_D/I_G):[58]

Method	Material	Growth Time	Growth Temp. (°C)	I_{2D}/I_G	I_D/I_G	$FWHM_{2D}$ (cm^{-1})	Grain Size	Sheet Resistance (Ω/sq)	Mobility ($cm^2V^{-1}s^{-1}$)	Ref
RF-PECVD	Co	15 s ~ 20 min	800	1.25 ~ 1.75	0.35~ 0.68	73 ~ 80	22 ~ 63 nm	–	–	15
RF-PECVD	Co	40 s	800	< 1	0.131	–	–	2661	–	16
RF-PECVD	Ni	5 min	850	0.71 ~ 2.03	~ 0	–	tens of μm	–	4500 (@RT)	17
RF-PECVD	Ni	1 min	650 ~ 700	0.24	~ 0	–	< 1 μm ~ 20 μm	–	3000	18
MW-PECVD	Ni	1 min	450 ~ 750	0.6 ~ 3.7	0.01 ~ 0.5	29 ~ 46	–	590 ~ 1855	–	19
RF-PECVD	Ni	100 ~ 600 s	475	0.22 ~ 1	0.2 ~ 1.8	33 ~ 60	–	4226 ~ 9142	–	20
MW-SWP-PECVD	Cu, Al	30 ~ 180 s	300 ~ 400	3.4	2.52	37	< 1 μm	1000 ~ 4100	–	21
RF-PECVD	Cu	5 min	950	0.2 ~ 2.25	1 ~ 1.5	–	10 ~ 20 nm	–	–	22
MW-SWP-PECVD	Cu	96 s	380	0.12 ~ 0.85	1.1 ~ 2.19	–	5 ~ 15 nm	9×10^5 ~ 3×10^6	–	23
RF-PECVD	Cu	0.2 ~ 4 min	700 ~ 830	2.2 ~ 4	0.2 ~ 0.7	31 ~ 43	0.4 ~ 3 μm	–	3200 (@RT)	24
MW-SWP-PECVD	Cu	2 ~ 4 min	240 ~ 500	0.42 ~ 0.78	1.39 ~ 2.25	–	–	10030	–	25
DC-PECVD	Cu	5 min	600	0.98 ~ 2.29	0.13 ~ 0.33	35 ~ 39	–	–	–	26
RF-PECVD	Cu	5 s ~ 60 min	950	0.98	0.11 ~ 0.82	–	–	1950 ~ 5200	–	27
RF-PECVD	Cu	2 and 4 min	220	1.51 ~ 1.72	0.78	–	0.1 ~ 1.2 μm	800	200	28
MW-PECVD	Cu	5 ~ 20 min	420	2.7	~ 0	28.8	a few mm's	–	3×10^4 ~ 6×10^4 (@RT)	11

Table 3.1. Comparison of different synthesis conditions for PECVD-growth of SLG on metallic substrates and the resulting characteristics of the graphene samples. Here RT refers to room temperature. Adapted from [59]

$$L_a(nm) \equiv \frac{560}{E_L^4}\left(\frac{I_D}{I_G}\right)^{-1}, \tag{3.1}$$

where E_L denotes the excitation energy of the laser source. Therefore, a variety of useful information about the quality and structural characteristics of graphene samples can be obtained by analyzing the peak frequencies, linewidths, and relative intensities of prominent Raman modes.

3.4 Single-step deposition of high-mobility graphene at reduced temperatures

We have developed a new growth method based on MW-PECVD under no active heating to the substrates.[29,59] This new method has been shown to reproducibly achieve, in one step, high-mobility large-sheet graphene samples that are nearly strain-free.

3.4.1 PECVD setup

The PECVD system is schematically illustrated in Fig. 3.1(a). It consists of an Evenson cavity and a power supply (MPG-4, Opthos Instruments Inc.), which provides an exciting

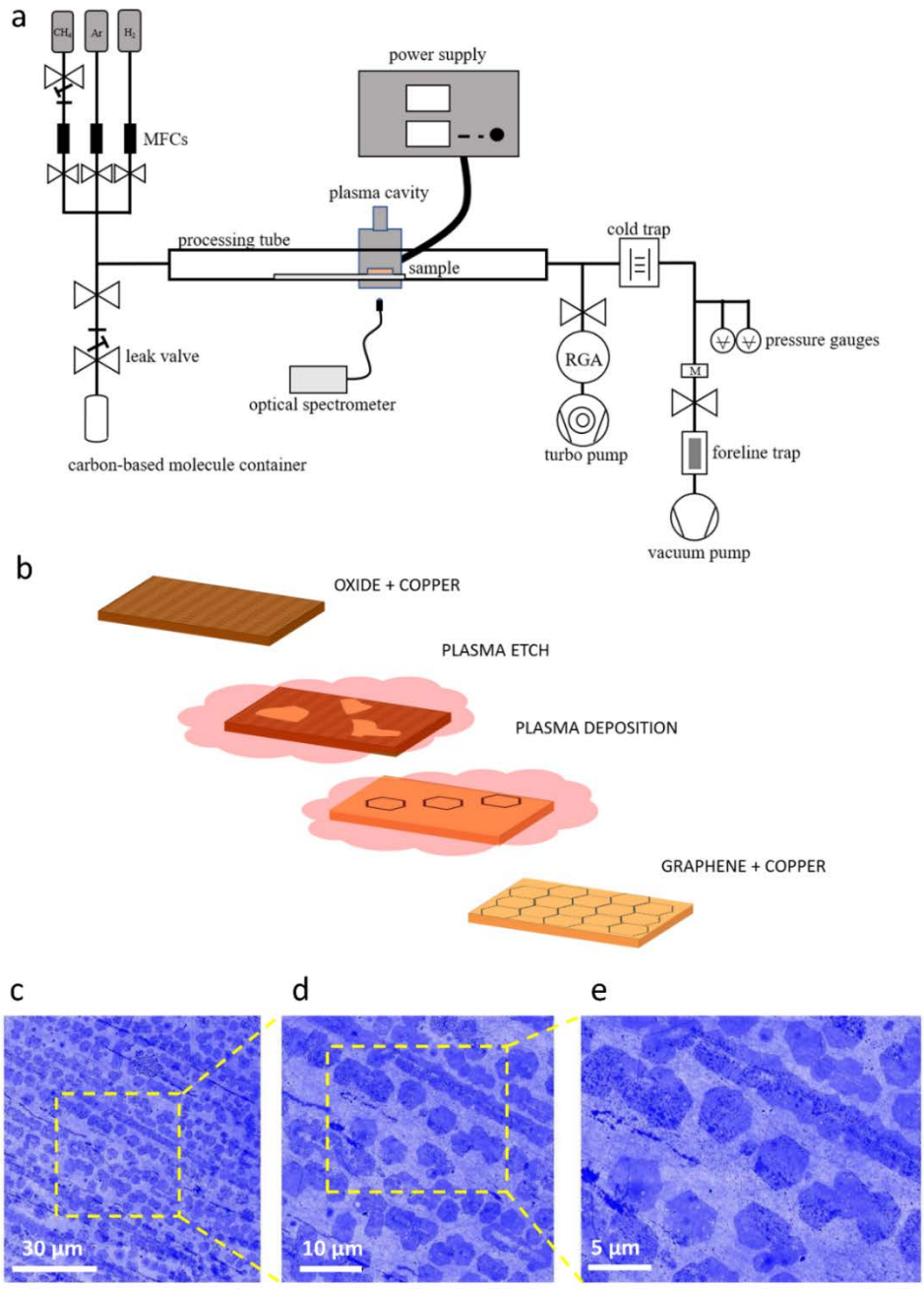

Figure 3.1 (a) A schematic of the PECVD setup for the synthesis of graphene sheets and VG-GNs without active heating. (b) Schematic illustration of the single-step PECVD growth mechanism of graphene on copper. (c)–(e) False-color SEM images of graphene grown for excessive time and transferred to single-crystalline sapphire, with increasing magnification from left to right, showing well-aligned, hexagonal adlayer graphene domains (dark) on the bottom SLG (light), which illustrate how the hexagonal grains nucleated along parallel lines of the copper foil coalesce into a single sheet of graphene.

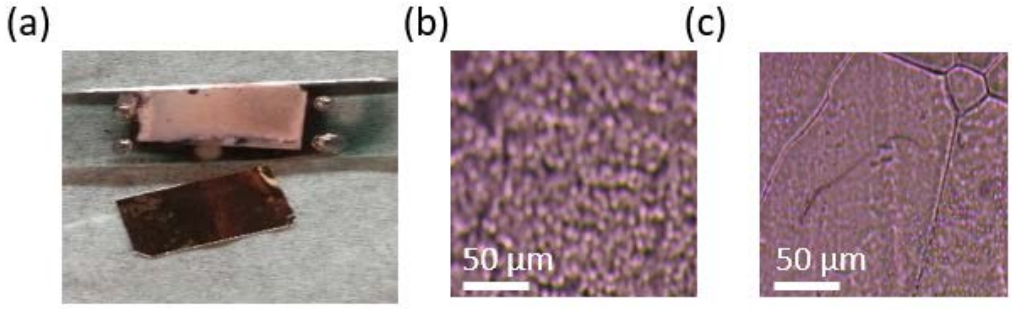

Figure 3.2 (a) A Cu foil and the sample holder, showing etched Cu after PECVD growth. Optical images of the top (b) and bottom (c) of a Cu foil after growth.

MW frequency of 2.45 GHz to generate plasma. A residual gas (RGA) is used to monitor the precursor and by-products partial pressure. The gas delivery system consists of mass flow controllers (MFCs) for H_2, CH_4, and Ar. The CH_4 gas flow is controlled by a leak valve placed before the methane MFC. Other than these typical gases to grow large-area graphene sheets, a quartz container stored with some substituted aromatics may be attached to the growth chamber via a leak valve and a quarter-turn, shut-off valve. With the addition of substituted aromatics such as 1,2-dichlorobenzene (1,2-DCB), 1,2-dibromobenzene(1,2-DBB), 1,8- dibromonaphthalene (1,8-DBN), and toluene as the seeding molecules, we can choose to grow graphene nanostripes (GNSPs), which will be elaborated later in chapter 6.

3.4.2 Nucleation and growth

In this new approach, cyano radicals play an important role in a hydrogen-methane plasma to remove Cu native oxide without active heating. After Cu is smoothly etched, graphene growth is found to nucleate from arrays of well-aligned hexagonal domains and eventually coalesced into a large sheet of ~1 cm^2, as schematically shown in Fig 3.1(b) and further exemplified in Fig. 3.1 (c)–(e). Raman spectroscopic of these SLG sheets generally revealed excellent spectral quality, as exemplified by a typical point spectrum in the red spectrum in the right panel of Fig. 3.3

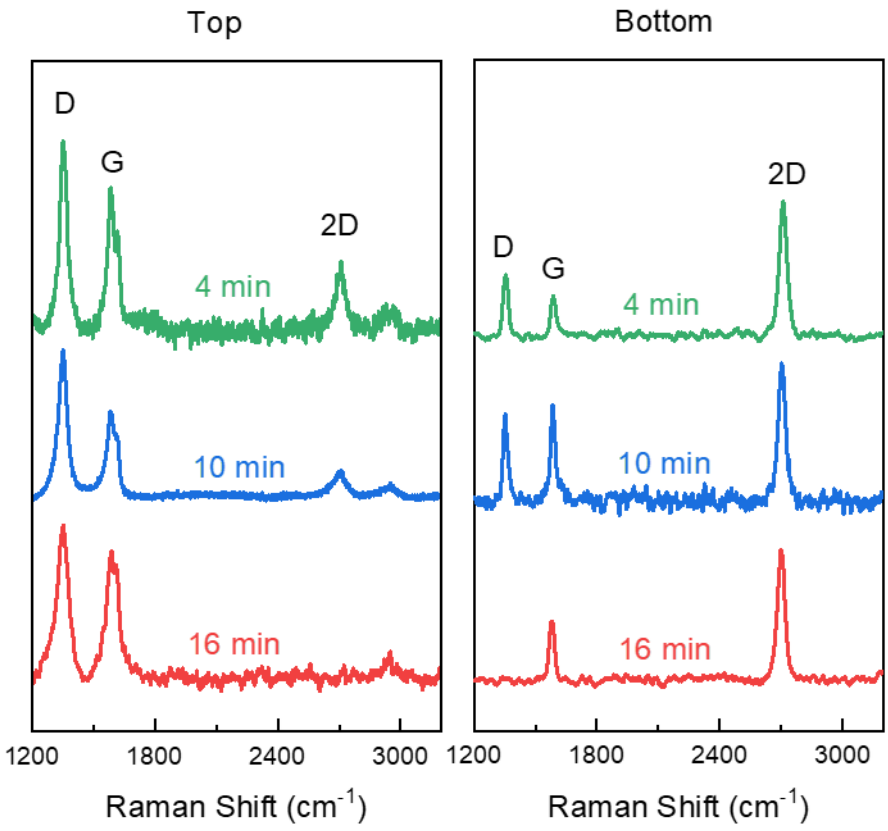

Figure 3.3 Comparison of the time-evolved Raman spectra of the top and bottom of the Cu foil taken with increasing growth time

We find that removal of Cu always accompanies graphene growth, as evidenced by the presence of Cu deposits on the quartz tube and sample holder for each successful growth. Fig. 3.2 (a) shows Cu deposits were found on the quartz sample holder after successful growth. Fig. 3.2 (b) and (c) are optical images of the Cu top surface and bottom surface after successful graphene growth. The top surface of the sample was always randomly pitted after growth (Fig. 3.2(b)) due to the direct ion bombardment in the plasma, but the bottom surface was smooth (Fig. 3.2(c)).

Nucleation of graphene occurred on both sides of the substrate. With continuous exposure to the plasma for 10 ~ 20 mins, disordered graphite and SLG covered the top and bottom sides. The time evolution Raman spectra of PECVD-graphene on Cu foil during growth is shown

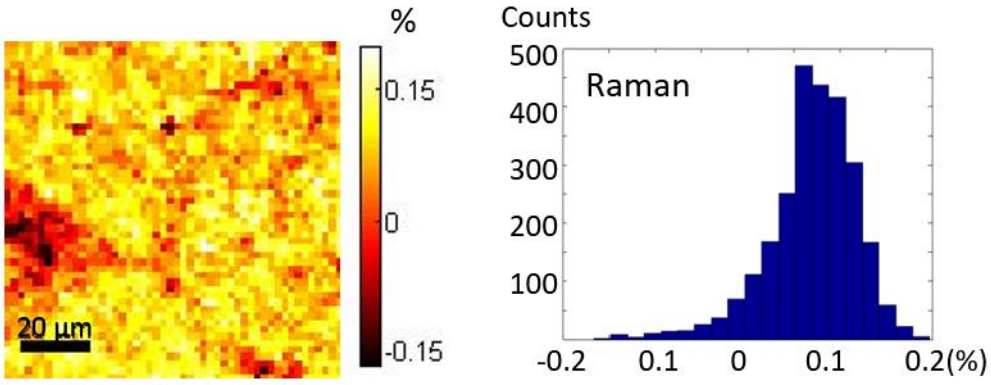

Figure 3.4. A strain map (left panel) and the corresponding histogram (right panel) of PECVD-grown graphene over a (100 × 100) µm2 area as derived from Raman spectroscopic studies.

in Fig. 3.3. Spectra from the top side show distinct D-band; however, the 2D-band decreased and vanished with increasing growth time, which indicates the formation of disordered graphite. On the contrary, spectra from the bottom side showed that the D-band decreased and eventually disappeared with increasing growth time. The I_{2D}/I_G indicated the formation of SLG, which is also consistent with the coalescence of graphene domains as shown in Fig. 3.1 (c) ~ (e)

3.4.3 Strain and structural order

Moreover, estimates of the magnitude of strain can be measured from both Raman spectroscopy and scanning tunneling microscopy (STM).[29] The biaxial strain $(\epsilon_{ll} + \epsilon_{tt})$ in the PECVD-graphene on Cu foil is determined by the Raman frequency shifts $\Delta\omega_m \equiv (\omega_m - \omega_m^0)$. and the Gruneisen parameter γ_m^{biax} in Eq. (2.20). Generally, we found a general trend of downshifted G-band and 2D-band for all PECVD graphene relative to thermal CVD-grown graphene on the same substrate. This indicates the averaged biaxial strain in PECVD-graphene is much reduced.

Fig. 3.4 is a spatial strain map of PECVD-grown graphene over an area of (100×100) μm^2 and the corresponding histogram. It shows nearly strain-free graphene with an average of 0.07% strain. This is in sharp contrast to the significant strain-induced effects found in thermal CVD-grown graphene.

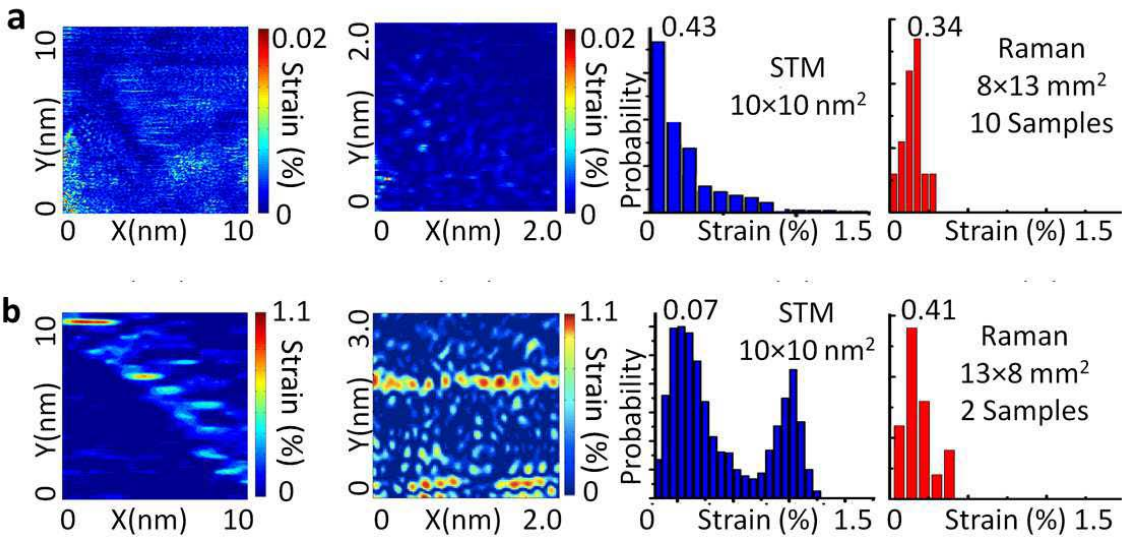

Figure 3.5. (a) From left to right, compression/dilation strain maps over successively decreasing areas taken with STM at 77 K (first and second columns, color scale in units of %), strain histogram (third column) of the strain map shown in the first column, and strain histogram (fourth column) obtained from Raman spectroscopic studies of different areas of multiple PECVD-graphene samples grown on Cu foils. (b) From left to right, compression/dilation strain maps over successively decreasing areas taken with STM at 77 K (first and second columns, color scale in units of %), strain histogram (third column) of the strain map shown in the first column, and strain histogram (fourth column) obtained from Raman spectroscopic studies of different areas of multiple thermal CVD-grown graphene samples on Cu foils.

The STM topography is also used to further analyze strain at the microscopic scale. For a local two-dimensional displacement field by $\mathbf{u} = u_x\hat{x} + u_y\hat{y} \equiv \mathbf{r} - \mathbf{r_0}$, where $\mathbf{r}$ and $\mathbf{r_0}$ are the actual position of a carbon atom and its equilibrium position in ideal graphene, respectively,[60] the compression/dilation strain is given by $\left(\frac{\partial u_x}{\partial x}\right) + \left(\frac{\partial u_y}{\partial y}\right) \equiv u_{xx} + u_{yy}$, which is proportional to the biaxial strain.[19–21] Using the topographies from both PECVD-graphene and T-CVD graphene on Cu foils, we obtained the spatial strain maps over successively decreasing areas in Fig. 3.5. The corresponding strain histograms are given in the third column in Fig. 3.5. The PECVD-graphene exhibited low and relatively homogeneous strain distributions. Further comparison with the macroscopic strain obtained from a collection of Raman spectra taken on different areas of multiple PECVD-

graphene samples is summarized by the strain histograms in the fourth column in Fig. 3.5. The average strain in PECVD-grown graphene was consistently more than one order of magnitude smaller than that of the SLG grown by the T-CVD method. There is overall consistency between microscopic STM studies and macroscopic Raman spectroscopic studies, revealing low strain for all PECVD-graphene. The finding of much-reduced strain in our PECVD-grown graphene samples is also consistent with their much better electrical mobility, typically 30 000 ~ 70 000 $cm^2V^{-1}s^{-1}$ at 300 K, which is comparable to the best values (40 000 ~ 60 000 $cm^2V^{-1}s^{-1}$) reported in multi-step, thermal CVD-grown single-crystalline graphene at 1.7 K.[37]

In addition to the high electrical mobility, we note that large-area strain-free graphene may be applied to strain engineering of novel nano-electronics by transferring strain-free SLG to substrates with pre-designed nanostructures to induce controlled spatial distributions of strain.[61] This approach is achievable because the local electronic properties of graphene are known to be highly susceptible to nanoscale lattice distortions.[7,19,21,61] Thus, proper design of the strain-induced on graphene by its underlying, nanoscale architected substrates can result in desirable modifications to the local electronic properties of graphene. Such nanoscale strain engineering of graphene for novel electronics is only feasible with the availability of sizable and nearly strain-free graphene synthesized by the PECVD method described in this chapter.

Chapter 4

NANOSCALE STRAIN ENGINEERING OF GRAPHENE

4.1 Introduction

As we have mentioned in Chapter 2, the distortion-induced strain in graphene lattice can give rise to an effective scattering scalar potential and an effective gauge potential (Eq. 2.18). For instance, compression, and dilation distortion can lead to charging effects in localized regions,[4,15–17] which have been manifested as strain-enhanced local density of states by scanning tunneling microscopic and spectroscopic (STM/STS) studies of graphene[21] that was grown by means of the high-temperature chemical vapor deposition (CVD) technique. It has also been theoretically proposed that certain controlled strain can induce a nearly uniform pseudo-magnetic field by lifting the valley degeneracy of graphene.[20,35] This prediction was first verified empirically via STM/STS studies of graphene nano-bubbles grown on Pt(111) substrates,[7] and subsequently reported in thermal CVD grown graphene on copper.[21] The presence of significant pseudo-magnetic fields could lead to the localization of Dirac fermions, whereas the charging effect could lead to strong scattering of Dirac fermions, both contributing to the reduction of electrical mobility. Further, extended structural distortion may lead to long-range symmetry breaking, giving rise to fundamental changes in the electronic band structures such as gap opening in the Dirac spectra and spontaneous local time-reversal symmetry breaking.[20,62,63] The symmetry-breaking distortion may give rise to novel gauge potentials, such as certain non-Abelian gauge potentials[57] and the Kekule distortion, [58] yielding novel electronic states such as fractionally quantized energy spectra as seen in STS studies of strained graphene.[20,21]

The susceptibility of graphene to structural distortions can, in fact, provide opportunities for engineering unique electronic properties of graphene.[64] For instance, the presence of pseudo-magnetic fields could be applied to the development of "valleytronics"[65–67] by lifting the valley degeneracy of graphene. Proper nanoscale strain engineering may also produce tunable electronic density of states for nano-electronic devices such as electron

beam collimators/deflectors or field-effect transistors.[64–67] On the other hand, the feasibility of nanoscale strain engineering relies on the premise of subjecting an ideal graphene sheet to controlled structural distortion. While exfoliated graphene could achieve nearly ideal graphene characteristics, the extremely small sheets and the non-scalable approaches to the production are not compatible with strain-engineering of practical devices. Alternatively, chemical vapor deposition (CVD) techniques at high temperatures (~ 1000ºC) have been shown to produce large sheets of graphene, although the resulting graphene often reveals significant spatial strain variations[21] unless numerous additional processing steps were taken.[37] The presence of uncontrollable strain distribution would not be suitable for nanoscale strain-engineering. In this context, the capability of reproducibly growing sizable high-quality and strain-free graphene is necessary for realizing the concept of strain engineering.

Our new PECVD method has been shown to reproducibly achieve, in one step, high-mobility large-sheet graphene samples that are nearly strain-free, paving the way for the realization of nanoscale strain-engineering. The objective of this chapter is to demonstrate the feasibility of nanoscale strain engineering of graphene by means of both theoretical simulations and empirical development of PECVD-grown graphene on nanostructured substrates. The correlation between realistic designs of nanoscale strain distributions and the resulting effects on the electronic properties of graphene is evaluated by means of molecular dynamics. Empirical proof of concept for nanoscale strain engineering via nanostructured substrates for graphene is also demonstrated and compared with theoretical simulations.

4.2 Theoretical simulations of strain-induced pseudo-magnetic fields

We employed molecular dynamics (MD) techniques to compute the spatial distributions of the displacement field, strain tensor and pseudo-magnetic field for given engineered nanoscale structural distortions to graphene. For simplicity, we chose either a nano-sphere or a nano-hemisphere with a varying radius as the building block for constructing different nanostructures on the substrate.

4.2.1 Methods of the simulations

For the MD simulations, we used the software package LAMMPS, which is available on the website http://lammps.sandia.gov. We considered a monolayer squared-shape graphene sheet with a fixed number of monolayer carbon atoms and assumed that the positions of the carbon atoms at the boundaries of this graphene sheet remained invariant throughout the simulations. To induce structural distortions, we moved the graphene sheet adiabatically towards either a nano-sphere or a nano-hemisphere of gold nanoparticle until a desirable maximum height h_0 relative to the boundaries of the graphene sheet was reached Fig. 4.1(a) ~ (b), and then relaxed the entire system until it reached equilibrium. Here the load necessary to move the graphene sheet towards the nanostructure was comparable to the combined effect of ambient air pressure and gravity.

Next, to ensure that the intrinsic properties of graphene were largely preserved without significant perturbations from the nanostructured substrate, we assumed that the attractive coupling between the graphene sheet and the underlying nanostructured substrate was sufficiently weak that it did not directly affect the graphene Hamiltonian. On the other hand, the attractive interaction must also be sufficiently strong to ensure proper conformation of graphene to the nanostructured substrate. We found that this situation could be realized by inserting a monolayer of hexagonal boron nitride (h-BN) in-between the graphene sheet and the nanostructure/substrate provided that the crystalline structure of the h-BN layer was aligned at an incommensurate angle relative to the graphene sheet so that no superlattice structures formed within the finite sheet of graphene under consideration.

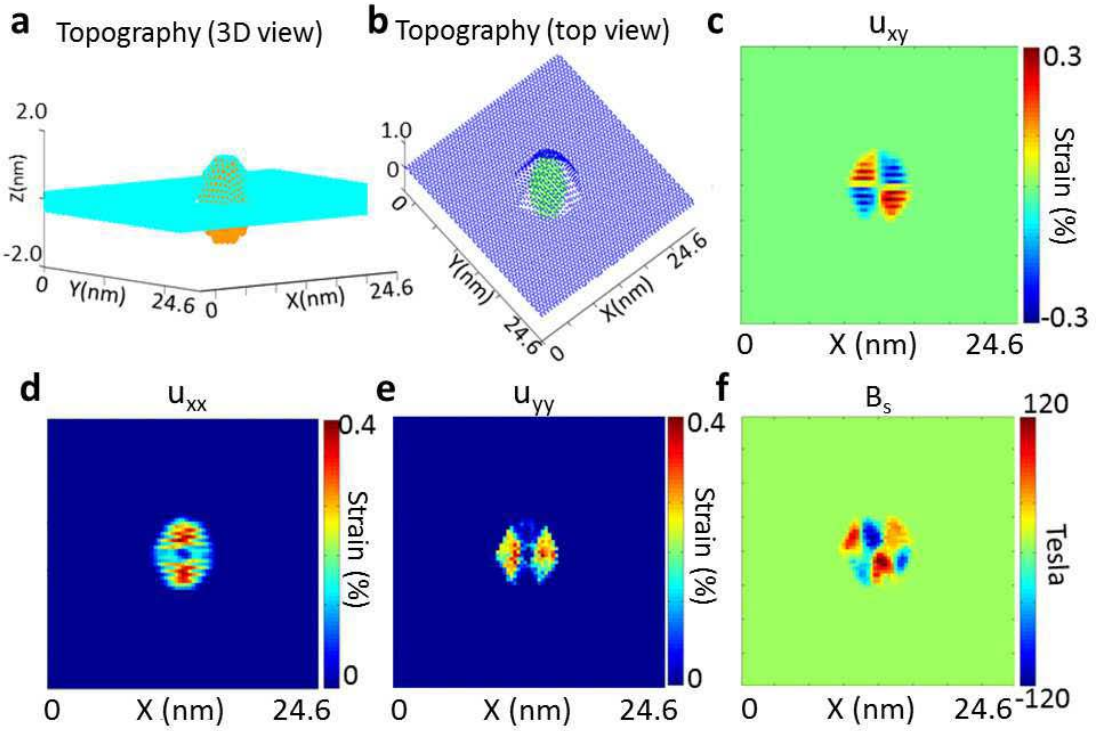

Figure 4.1. MD simulations of the strain effects on a (24.6×24.6) nm^2 graphene sheet induced by a nanoparticle with a diameter 2.4 nm and a maximum height h_0 = 2.4 nm: (a) A three-dimensional illustration of the structural distortion to the graphene sheet above a nanoparticle. (b) The two-dimensional topographic distortion of the graphene sheet shown in (a). (c) Spatial map of the strain tensor u_{xy}. (d) Spatial map of the strain tensor u_{xx}. (e) Spatial map of the strain tensor u_{yy}. (f) Spatial map of the pseudo-magnetic field B_s.

The rationale for the choice of h-BN for the substrate material was based on the empirical fact that graphene on h-BN exhibited as excellent electrical mobility and fractional quantum Hall effects as those of suspended pristine graphene, in sharp contrast to substantially degraded mobility of graphene on other substrates (such as SiO_2/Si). Therefore, we employed realistic parameters for the van der Waals interaction of BN with carbon atoms and assumed isothermal conditions throughout the simulations and all nanostructured substrates for empirical strain engineering of graphene described in this chapter.

Based on the approach outlined above, we were able to locate the three-dimensional coordinates of all carbon atoms on the graphene sheet and determined the two-dimensional coordinates of the three-dimensional displacement fields (u_x, u_y, h) and the resulting strain tensor components (u_{xx}, u_{yy}, u_{xy}) from Eq. (2.17). Finally, we computed the vector potential components $(\mathrm{A}_x, \mathrm{A}_y)$ from Eq. (2.19) and the pseudo-magnetic field components $(\mathrm{B}_x, \mathrm{B}_y)$.

4.2.2 Strain induced by an isolated nanosphere on the substrate for graphene

Using the aforementioned criteria and Eq. (2.17), we obtained in Fig. 4.1(c) ~ (f) maps of the strain tensor components u_{xx}, u_{yy}, u_{xy} and the resulting pseudo-magnetic field B_s for a graphene sheet of (100 × 100) unit cells, which was (24.6 × 24.6) nm^2 in area, under the distortion of a nanoparticle with a diameter d = 2.4 nm and a maximum height h_0 = 2.4 nm.

It is interesting to note that the spatial distribution of the strain-induced pseudo-magnetic fields B_s reveals an approximate three-fold symmetry pattern with the alternating polarity of B_s values that maximize around the location of the gold nanoparticle. The orientation of the three-fold symmetry pattern coincides with the zigzag direction of the graphene lattice structure. We further note the large magnitude of B_s values (up to ~ 120 Tesla, Fig. 4.1(f)), suggesting substantial modifications of the graphene electronic properties under such a nanostructure of comparable lateral and vertical dimensions. For comparison, if the maximum height h_0 is reduced from 2.4 nm to 1.2 nm, the maximum $|B_s|$ value decreases from ~ 120 to ~ 77 Tesla, which is consistent with the strong dependence of the induced pseudo-magnetic field on the height of the distortion.

4.3 Engineering arrays of nanodots on silicon substrates by focused-ion-beam

4.3.1 Sample preparation

Our first step towards nanoscale strain engineering of graphene was to investigate whether initially strain-free graphene could conform well to periodic arrays of nanostructures and would result in significant strain and pseudo-magnetic fields as theoretically predicted. To

this end, we fabricated periodic spherical nanostructures using a dual-focused ion beam (FIB) and scanning electron microscope (SEM) (FEI Nova NanoLab 600 DualBeam). The primary Ga^+ ion beam was operated at 30 keV and beam current was 10 pA. After the fabrication, we determined the topography of these nanostructures by means of both SEM and atomic force microscopy (AFM). The SEM images were taken with 5 kV acceleration voltage, 98 pA beam current, and a working distance ~ 5 mm. The AFM images were acquired in the tapping mode by Bruker Dimension Icon AFM.

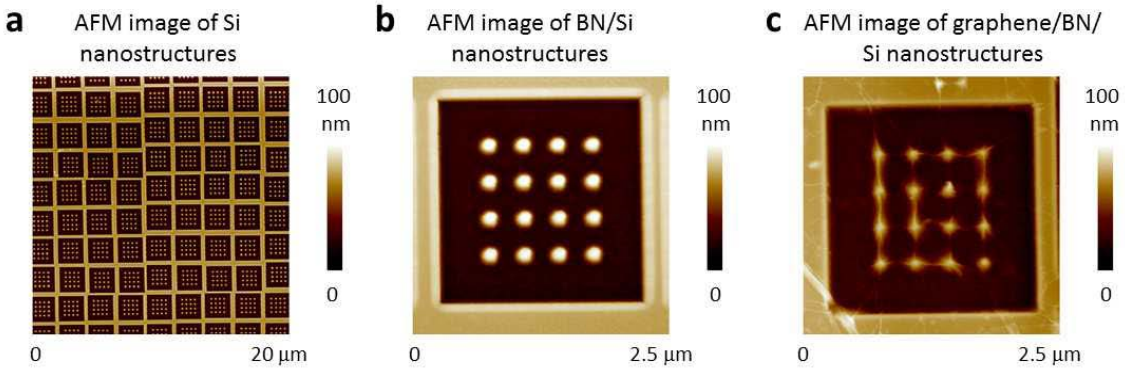

Figure 4.2. AFM images of nanostructures for strain engineering of graphene: (a) Arrays of Si-nanostructures created by Ga- FIB over a (25 × 25) μm^2 area. The diameter and height of the nanostructures were ~220 nm and ~60 nm, respectively, and the inter-dot separation between the centers of the neighboring nanodots was ~440 nm. (b) One monolayer of BN on top of Si-nanostructures over a (2.5×2.5) μm^2 area, showing excellent conformation of BN to the Si nanodots. (c) One monolayer of graphene on top of the structure shown in (b), revealing graphene "wrinkles" along the aligned Si nanodots.

The nanostructures that we fabricated on silicon using the Ga-FIB consisting of nanodots with a diameter of ~ 220 nm and a height of ~ 60 nm, as shown in Fig. 4.2. These nanostructures were repeated into (4×4) arrays with an average separation of ~ 440 nm (between the centers of two neighboring nanodots) within a (2.5×2.5) μm^2 square, and the same arrangements were repeated over a (20 × 20) μm^2 area. Monolayer hexagonal boron nitride (h-BN) was then transferred onto the Si-nanostructures, followed by the transfer of PECVD-graphene onto the substrate of BN/Si-nanostructures. We performed AFM and SEM measurements on every step of the process and found that BN conformed very well

to the Si-nanostructures, as exemplified by the AFM image in Fig. 4.2(b). Interestingly, upon the deposition of graphene on BN/Si-nanostructures, we found that graphene appeared to wrinkle up slightly along the nanostructures, as exemplified by the AFM image in Fig. 4.2(c).

4.3.2 Raman spectroscopic studies of the nanostructure-induced strain effects on graphene

To investigate the macroscopic strain induced by regular arrays of nanostructures, we performed spatially resolved Raman spectroscopic studies on the graphene/BN/Si-nanostructure sample shown in Fig. 4.2(c), and also compared the spectra with those taken from reference areas of the same sheet of graphene without underlying Si-nanostructures. The Raman spectrometer used a laser excitation of 532 nm with a spot size of about 500 nm. We mapped at 0.5 μm per pixel steps. Each 2D-band spectrum was fit to a single Lorentzian, and the frequency peak position was assigned as the corresponding 2D-band frequency. While the spatial resolution of the Raman spectrometer at 0.5 μm was not sufficient to resolve the spatial distribution of strain associated with the individual nanodots, it appeared that the strain effects induced by the larger squared features could be resolved in some places. Overall the spatial map of the 2D-band over the area of graphene above the nanostructures clearly revealed significant inhomogeneity (Fig. 4.3(a)), which was in sharp contrast to the spatial homogeneity of the 2D-band map of a controlled area of graphene on top of a flat region of the BN/Si substrate (Fig. 4.3(b)). A more quantitative comparison of the spatial distributions of the 2D-band frequency in these two areas is illustrated by the histograms in Fig. 4.3(c), where a much broader 2D-band and therefore much wider strain variations induced by the presence of nanostructures is clearly demonstrated.

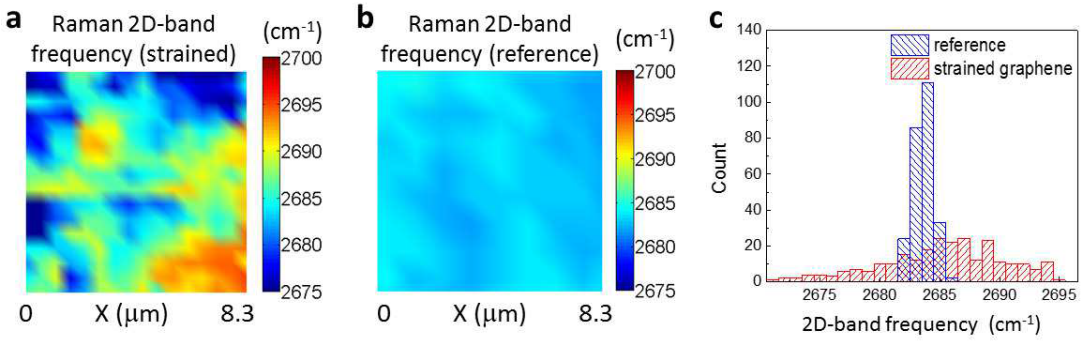

Figure 4.3. Raman spectroscopic studies of the spatial distributions of strain in graphene: (a) Spatial map of the 2D-band of graphene on top of a (10 × 10) μm^2 area of nanostructure arrays shown in Fig. 4.2(a). The pixel size of the Raman map is 0.5μm, which is insufficient to resolve the small nanostructures. Nonetheless, the map still reveals strong spatial inhomogeneity, with some of the highly strained lines consistent with the larger patterned features of the squares. (b) Spatial map of the 2D-band of graphene over a (10×10) μm^2 reference area above a flat region of the BN/Si substrate. The pixel size of the Raman map is 0.5μm, and the map appears to be spatially homogeneous. (c) Comparison of the histogram of the 2D-band between strained graphene in (a) and the strain-free reference area in (b), showing much broader 2D-band distributions in the strained area.

4.4 Engineering nanodots on silicon by self-assembly of gold nanoparticles

In order to investigate the strain distributions with much higher spatial resolution, STM must be employed. However, it is generally very challenging to locate the small (20 × 20) μm^2 patterned area within a relatively large sample area, typically on the order of (5×5) mm^2, under the atomically sharp STM tip. While this issue may be addressed by enlarging the total area of patterned nanostructures, another plausible approach was to distribute metallic nanoparticles over the entire substrate by means of self-assembly. This approach could enable quasi-periodic distributions of nanoparticles with a limited range of diameters. Although not ideal for well-controlled strain engineering, the use of self-assembled nanoparticles in place of either FIB or electron-beam fabricated nanostructures could provide preliminary and semi-quantitative verifications for our theoretical designs, and so was worthy of exploration.

4.4.1 Sample preparation

For this work, the self-assembled gold nanoparticles were developed from solutions on silicon substrates using block copolymer lithography (BCPL)[68]. The preparation procedure is briefly summarized below.

The solutions were mixed in a Pyrex 5 ml micro volumetric flask that was specifically designed for microchemical work. The glassware was cleaned in aqua regia, rinsed in DI water, followed by ultrasonication, and triple rinsed in DI water followed by mild baking to remove any residual moisture. The copolymer (Polymer Source, Inc.) was the diblock copolymers 25.5 mg of polystyrene (81,000)-block-poly(2-vinylpyridine)(14,200), which was dissolved in 5 ml of ultra-high purity toluene (Omnisolve, 99.9%) and spun vigorously with a Teflon stir bar for four days. The solution was clear. The gold precursor was Gold(III) chloride hydrate (99.999% trace metals basis Aldrich, Inc.), and 14.6 mg were added to the diblock copolymer solution under dry nitrogen and in a darkened environment. The solution was then stirred vigorously for l0 days to insure particle uniformity. The solution remained clear upon stirring, but the color changed to amber.

The gold arrays were formed on mechanical grade silicon (5 x 5) mm without removing the native oxide. The silicon substrate was first blown with dry nitrogen to remove particulates and then subjected to a 100 W oxygen plasma (Technics Inc., Planar Etch) for five minutes to remove any hydrocarbon residue. The substrate was loaded on a spin-coater and held in place with a vacuum chuck. The Au-BCPL solution was dropped onto the silicon substrate so that the entire top surface was covered. The sample remained covered for 30 s before starting the spin process. Samples were spun at 3000 RPM for 60 s. The substrate was removed from the spin-coater and placed in an oxygen plasma for 25 minutes at 100 W and was subsequently removed from the plasma and baked overnight at 220 ◦C.

Upon drying the solution and removing the polymer, quasi-periodic gold nanoparticles of diameters ranging from 14 to 20 nm remained and covered the surface of the silicon substrate, with an average separation between adjacent nanoparticles ranging from 10 to

30 nm, as exemplified in Fig. 4.4(a) for an AFM image over an area of (1 × 1) μm^2. Next, a monolayer BN was placed over the Au-nanoparticles/silicon substrate, which was found to conform well to the nanoparticles, as shown in Fig. 4.4(b). Finally, a monolayer PECVD-grown graphene was placed on top of the BN/Au-nanoparticles/silicon, which induced wrinkles on graphene, as illustrated in Fig. 4.4(c) and similar to the findings in Fig. 4.2(c). In particular, we note a general preferential wrinkle alignment along approximately 150º direction relative to the x-axis of the plot.

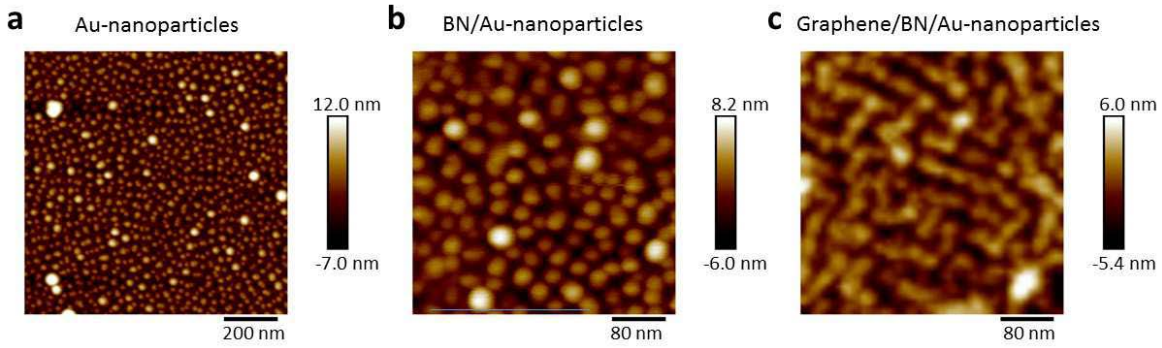

Figure 4.4 AFM images of self-assembled nanostructures: (a) Quasi-periodic gold nanoparticles of diameters 14 ~ 20 nm on silicon over an area of (1 × 1) μm^2. (b) One monolayer of h-BN on top of the same quasi-periodic gold nanoparticles in (a) over a (500 × 500) nm^2 area, showing excellent conformation of BN to the Au nanoparticles. (c) One monolayer of PECVD-grown graphene on top of the structure shown in (b), revealing graphene "wrinkles" with a preferential wrinkle alignment along approximately 150º direction relative to the x-axis of the plot.

4.4.2 Characterizations of strain-induced modifications to the density of states by scanning tunneling spectroscopy

We performed STM and STS studies on the aforementioned graphene/BN/Au-nanoparticle sample at 300 K to characterize the spatial distribution of strain. In Fig. 4.5(a) the STM topography over a (140×140) nm^2 area revealed the protrusion of graphene above nanoparticle structures. Close-up point spectroscopic studies around the nanoparticle structures (Fig. 4.5(b), which corresponded to the lower-left area of Fig. 4.5(a)) indicated

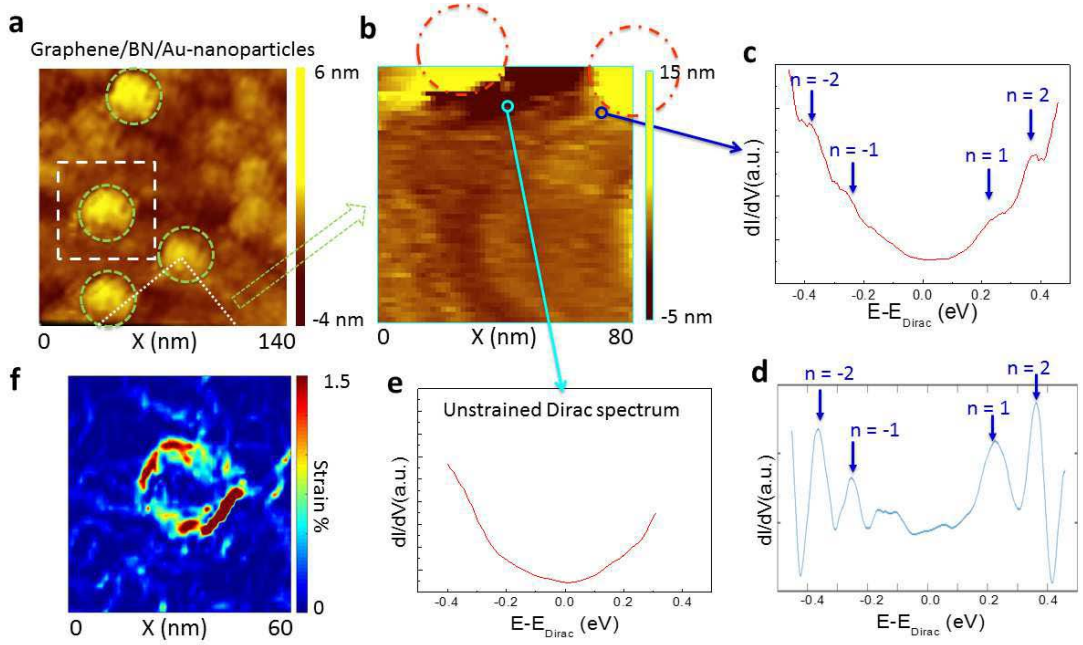

Figure 4.5 STM studies of the topography and tunneling spectroscopy in graphene/BN/Au-nanoparticles at 300 K: (a) Surface topography of a (140×140) nm^2 area, showing surface protrusion above Au-nanoparticles of ~25 nm diameter. (b) Surface topography of an (80×80) nm^2 area that corresponded to the region partially indicated by the white box in (a), showing two partial nanoparticles in the upper region. (c) Point spectrum taken at the location indicated by the blue circle on the right, which corresponded to a region of rapid changes in height. Excess enhancement in the tunneling conductance appeared at quantized energies that corresponded to Landau levels associated with a pseudo-magnetic field on the order of B_s ~ 55 Tesla according to Eq. (2.21). (d) The same point spectrum as in (c) after subtraction of the background Dirac spectrum. (e) Point spectrum taken at the location indicated by the light blue circle on the left, which corresponded to a flat region of negligible strain so that the spectrum is consistent with the standard Dirac spectrum. (f) The magnitude of the biaxial strain map of graphene obtained from atomically resolved topographic studies of the (60 × 60) nm^2 area indicated by the white dashed box in (a), showing maximal strain near the periphery and minimal strain around the top of the nanoparticle.

that in the highly strained regions where maximum changes in the graphene height appeared (with >~ 10 nm descent over a lateral dimension <~ 4 nm), extra spectral features associated with the quantized density of states under a large pseudo-magnetic field appeared on top of the typical Dirac spectrum, as exemplified in Fig. 4.5(c), where the excess quantized spectral features (Fig. 4.5(d), after the subtraction of the Dirac spectrum) correspond to a pseudo-magnetic field B_s ~ 55 Tesla according to Eq. (2.21). In contrast,

for relaxed regions of the graphene sample, the tunneling spectra recovered the standard Dirac spectrum under finite thermal smearing (Fig. 4.5(e)). Interestingly, the magnitude of the strain-induced pseudo-magnetic field is somewhat smaller than the result of $B_s \sim 77$ Tesla from the MD simulations for an isolated nano-hemisphere with a diameter 2.4 nm and maximum height $h_0 = 1.2$ nm, the latter having an aspect ratio comparable to that of the Au-nanoparticles used in this work. This finding is reasonable because generally for the same aspect ratio of structural distortions, the induced strain decreases gradually with the increasing physical size of the distortion.

4.4.3 Discussion

Although the concept of nanoscale strain engineering of initially strain-free graphene samples has been verified semi-quantitatively based on the aforementioned studies, a number of challenges remain.

First, any finite interactions between the substrate material and graphene would complicate the effect induced by generic structural distortions. While our insertion of a monolayer of BN between the substrate and graphene was intended to minimize the influence of the substrate and to preserve the generic properties of graphene, in the event of nearly perfect alignment of graphene with the underlying h-BN lattices, the Dirac electrons of graphene could become gapped[67] so that the theoretical foundation for strain engineering of gapless Dirac fermions would no longer hold.

Second, our MD simulations have assumed perfectly local pseudo-magnetic fields in response to the local strain. This assumption is justifiable if the carrier density in the graphene sheet is sufficiently low so that electronic screening effects are negligible. On the other hand, doping effects of spatially inhomogeneous charged impurities could result in weakened pseudo-magnetic fields and broadened Landau levels, which may account for the relatively broad linewidths observed in the tunneling spectra in Fig. 4.5(c).

Quantitatively, we may incorporate the non-local correction to the evaluation of an effective pseudo-magnetic field $\langle Bs(x_0, y_0)\rangle$ at position (x_0, y_0) by the following formula:

$$\langle B_s(x_0, y_0)\rangle = (2\pi l_0^2)^{-1} \int_{-X}^{X} dx \int_{-Y}^{Y} dy\, B_s(x, y) \times exp\left[-\sqrt{(x - x_0)^2 + (y - y_0)^2}/l_0\right], \tag{4.1}$$

where l_0 denotes the mean free path, and we have assumed that the x-range (y-range) of the sample expands from $-X$ to X (from $-Y$ to Y). For a constant pseudo-field distribution over an infinite sample, we have $\langle B_s(x, y)\rangle = B_s(x, y)$ everywhere within the sample as expected. On the other hand, a short mean free path l_0 would result in effective $\langle B_s(x, y)\rangle$ values significantly smaller than the local value of $B_s(x, y)$ according to Eq. (4.1).

We further remark that the relevant characteristic length involved in the non-local effect of pseudo-magnetic fields in Eq. (4.1) should be the mean free path l_0 rather than the pseudo-magnetic field length l_B, because the contributions from the strain-induced gauge potential are only perturbative to the total Hamiltonian of the Dirac fermions, hence not all Dirac fermions are completely localized to the length scale of l_B by the presence of a pseudo-magnetic field, which is different from the situation for a global time-reversal symmetry breaking magnetic field.

For a given spatial distribution of $B_s(x, y)$, if we define the deviation of the effective pseudo-magnetic field $\langle B_s(x, y)\rangle$ from its local value by δB_s, we find that from Eq. (2.21), the linewidth δE_n of the Landau level energy E_n becomes $\delta E_n \propto \sqrt{|n/B_s|}\delta B_s$. Therefore, the linewidth of E_n increases with increasing non-local corrections to B_s. On the other hand, for a given pseudo-magnetic field distribution we expect sharper Landau levels at locations with larger B_s values. Ultimately, we expect much sharper conductance peaks for pseudo-magnetic fields induced on nearly impurity-free graphene by well-ordered and

well-shaped nanostructures and hope to verify this notion by further experimental investigation.

4.5 Engineering nanodots on silicon by Pd tetrahedron nanocrystals

4.5.1 Graphene/BN/Pd tetrahedron sample preparation

In this session, the Pd tetrahedron nanocrystals (NCs) were synthesized by a wet-chemical method.[69] The preparation procedure is briefly summarized below. We mixed 7.6 mg palladium (II) acetylacetonate (Pd(acac)2), 16.5 mg iron (II) acetylacetonate (Fe(acac)2), 50.0 mg polyvinylpyrrolidone (PVP), and 10.0 ml N, N-dimethylformamide (DMF) into a 30 mL vial. After ultrasonication for 5 minutes, the mixture was heated at 120°C for 10 hours in an oil bath on a hotplate. The resulting precipitant was collected by centrifugation and rinsed with ethanol several times.

To induce controlled nanoscale strain on initially strain-free graphene, we carried out the procedures schematically illustrated in Fig. 4.6(a). A Si substrate was first ultrasonicated in acetone and subsequently in IPA for 10 minutes each, blown dry with dry nitrogen, and then loaded into a 100 W O_2-plasma for 5 minutes to remove any traces of hydrocarbon residue. The Pd tetrahedron suspension was dropped onto the Si substrate and spun at 1500 RPM for 1 minute. After the spin-coating process, the sample was loaded into a 100 W O_2-plasma for 5 minutes again to remove any residue on the Pd tetrahedron NCs. The resulting typical size of the Pd tetrahedron NCs ranges from 50 to 70 nm and the height ranges from 40 to 60 nm, as exemplified in Fig 4.6(b) and 4.6(c). Next, a monolayer BN was transferred over the substrate covered by the Pd tetrahedron NCs, followed by the transfer of PECVD-graphene onto the BN/Pd-NCs. AFM and SEM measurements were performed on every step of the process. We found that graphene/BN conformed very well to the Pd tetrahedron NCs if they were well separated from each other, as exemplified by the AFM image in Fig. 4.6(d) and 4.6(e) (top panel). However, we found that graphene tended to form wrinkles along the Pd tetrahedrons if they were sufficiently closed to each other, as exemplified by the AFM images in the bottom panel of Fig. 4.6(e). This situation is similar

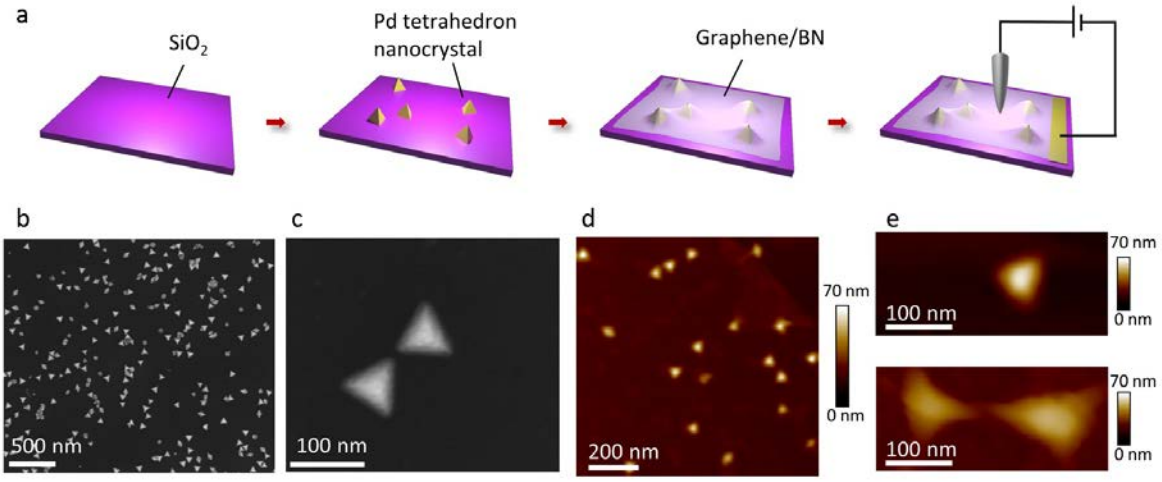

Figure 4.6 Nanoscale strain engineering of graphene: (a) Schematic illustrations showing the steps taken to induce strain on graphene by Pd tetrahedron nanocrystals (NCs). (b) An SEM image of randomly distributed Pd tetrahedron NCs distributed on a Si substrate over a (3 × 3) μm2 area. (c) A zoom-in SEM image of two Pd tetrahedron NCs. (d) Exemplifying AFM image of graphene/*h*-BN/Pd tetrahedron NCs. (e) Top panel: AFM image of graphene/BN on a single Pd tetrahedron NC, showing excellent conformation of graphene/BN to the single Pd tetrahedron NC. Bottom panel: AFM image of graphene/BN on two closely spaced Pd tetrahedron NCs, showing the formation of a graphene "wrinkle" between the two Pd tetrahedron NCs.

to our previous observation of graphene/*h*-BN on Au nanoparticles and graphene/*h*-BN on Si nanostructures.

4.5.2 Topographic and spectroscopic evidence for the formation of giant pseudo-magnetic fields

In Fig. 4.7 we illustrate the comparison of the strain-induced pseudo-magnetic fields for the K valley from both topographic and spectroscopic studies at room temperature. The main panel of Fig. 4.7(a) and Fig. 4.7(b) are respectively zoom-out AFM and STM topographic images over a (100 × 100) nm^2 area that cover the full view of monolayer

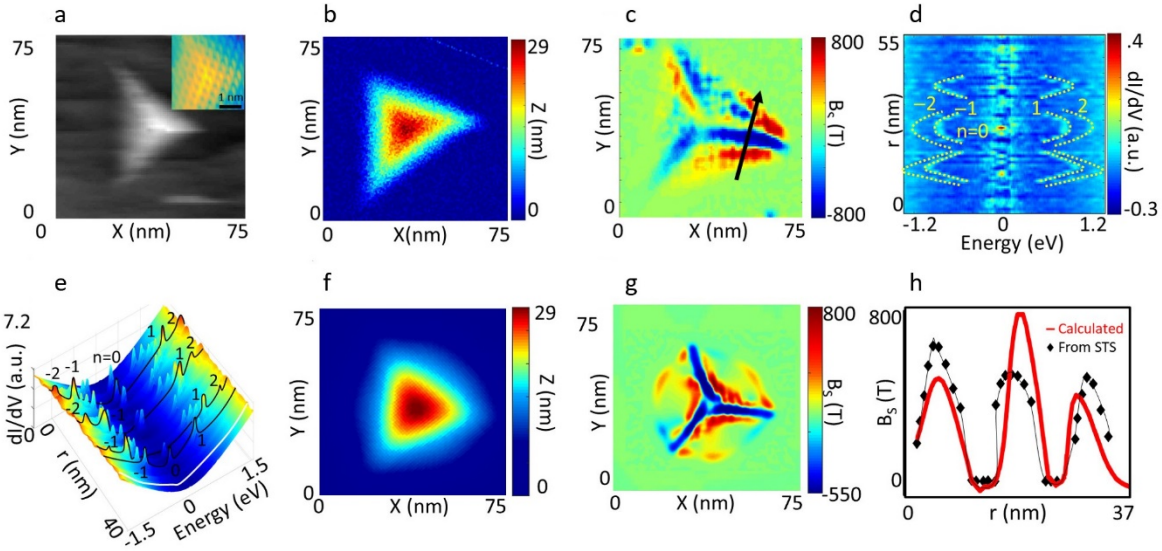

Figure 4.7 Topographic and spectroscopic studies of strain-induced effects on graphene at room temperature due to one Pd tetrahedron NC: (a) Three-dimensional (3D) topographic images of the distorted graphene taken by AFM (Main Panel) and by STM (Inset, a zoom-in image with atomic resolution). (b) 3D topographic image of the distorted graphene taken by STM. (c) The pseudo-magnetic field map calculated from the topography over the same area as shown in (b).(d) Tunneling conductance spectral difference relative to the Dirac spectrum of strain-free graphene is shown along the line-cut indicated by the black arrow in (c), revealing spatially varying strengths of strain-induced pseudo-magnetic fields as manifested by the variations in the Landau-level separation. (e) Representative spectra of tunneling conductance-*vs.*-energy of strained graphene along the black line-cut in (c), showing quantized conductance peaks in strained regions and the V-shape Dirac spectrum in strain-free regions as exemplified by the white curve located at $r \sim 36$ nm. (f) 3D topographic map of graphene/*h*-BN deformation on an ideal tetrahedron, as computed from MD simulations described in Supplementary Material. (g) Pseudo-magnetic field map computed from the topographic distortion in (f). (h) Comparison of the absolute values of pseudo-magnetic fields $|B_s(r)|$ derived from topographic studies (red line) and from the Landau level separations in STS (black diamonds), showing overall satisfactory agreement. Here r denotes the distance measured from the lower-left end to the upper-left end of the black arrow shown in (c).

graphene/*h*-BN over an isolated Pd tetrahedron. In the inset of Fig. 4.7(a), a zoom-in atomically resolved STM topography of graphene over a (3×3) nm^2 area near the tip of the tetrahedron reveals strong structural distortion in graphene with significant height displacements. Assuming the validity of first-order strain-induced perturbation to the Dirac Hamiltonian and using the Molecular Dynamics (MD), we obtain the resulting pseudo-

magnetic field distributions in Fig. 4.7(c) for the topography shown in Fig. 4.7(b). Given the significant structural distortions in graphene, we note the resulting large magnitudes of the pseudo-magnetic field, up to ~ 800 Tesla in maximum values if computed from the topographic information.

Concurrent spectroscopic studies of the strained graphene over the isolated tetrahedron also revealed spatially varying tunneling spectra, as exemplified in Fig. 4.7(d) for a collection of high-resolution tunneling conductance vs. bias voltage spectra along the black line indicated in Fig. 4.7(c). Here the horizontal axis in Fig. 4.7(d) corresponds to the bias voltage, the vertical axis corresponds to the spatial dimension along the black line (from the lower left to the upper right) in Fig. 4.7(c), and the colors represent the tunneling conductance difference from the unstrained graphene. The three-dimensional representation of the tunneling spectra taken along the same line-cut is shown in Fig. 4.7(e). Specifically, a typical V-shaped tunneling spectrum for ideal graphene is clearly shown in the strain-free region, as exemplified by the white curve in Fig. 4.7(e), whereas increasing larger energy separations for consecutive peak features are found for the tunneling spectra taken at increasingly strained regions, showing a consistent increase in the Landau level energy separations with the increasing magnitude of strain found in the topographic studies.

To further verify the consistency between the magnitude of the pseudo-magnetic field determined from topography and from spectroscopy, we compare in Fig. 4.7(h) the absolute values of pseudo-magnetic fields $|B_s(r)|$ derived from topographic studies (Fig. 4.7(c)) and those from the Landau level separations (Fig. 4.7(d)), showing overall reasonable agreement. Here r denotes the distance measured from the lower-left end to the upper-left end of the black arrow in Fig. 4.7(c). Additionally, we carried out MD simulations for the topography and pseudo-magnetic field map of single layer graphene/*h*-BN strained by a perfect tetrahedron with a base dimension of 30 nm, as shown in Fig. 4.7(f) and 4.7(g), respectively. These MD simulations are largely consistent with the experimental results shown in Fig. 4.7(b) and 4.7(c), although it is difficult to achieve detailed agreement due to

unknown microscopic interaction parameters between the single layer graphene/*h*-BN and the underlying nano-tetrahedron that are required to carry out the MD simulations.

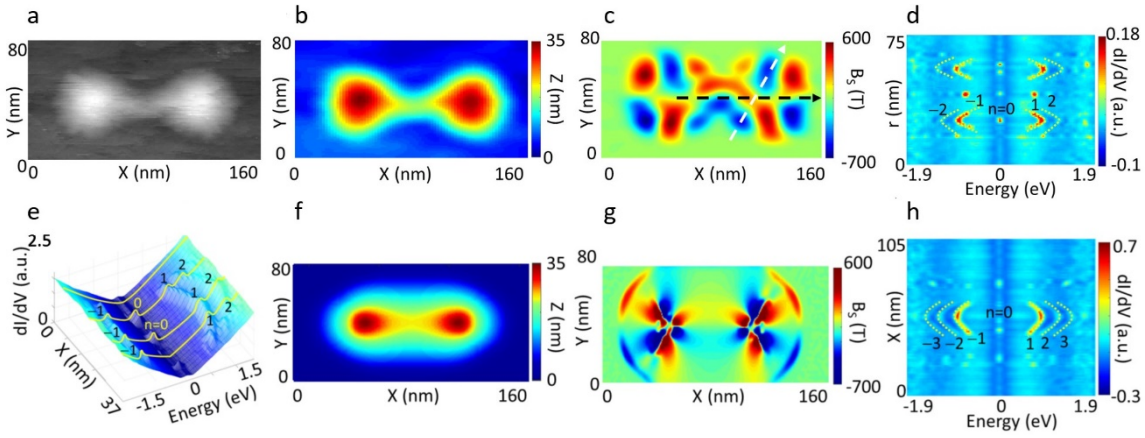

Figure 4.8 Topographic and spectroscopic studies of strain-induced effects on graphene due to two closely separated Pd tetrahedron NCs: (a) Three-dimensional (3D) topographic images of the distorted graphene taken by AFM (Main Panel) and by STM (Inset, a zoom-in image with atomic resolution). (b) 3D topographic image of the distorted graphene taken by STM. (c) The pseudo-magnetic field map calculated from the topography over the same area as shown in (b). (d) The tunneling conductance spectral difference from the Dirac spectrum along the line-cut shown by the white dashed line in (c). (e) Spatially resolved tunneling spectra of strained graphene along the black dashed line in (c), showing strain-induced quantized conductance peaks. (f) 3D topographic map of graphene/*h*-BN on two ideal tetrahedrons computed from MD simulations. (g) Pseudo-magnetic field map computed from topographic distortion shown in (f). (h) The tunneling conductance spectral difference relative to the Dirac spectrum along the line cut shown by the black dashed line in (c).

Next, we consider the strain on graphene induced by two closely spaced nano-tetrahedrons, as manifested by the topography in Fig. 4.8(a) and the corresponding pseudo-magnetic field map for the K-valley in Fig. 4.8(b). We found that the maximum magnitude for the pseudo-magnetic field computed from the structural distortion was ~ 600 Tesla (Fig. 4.8(c)), smaller than that found in the case of the single tetrahedron (Fig. 4.7(c)). This is because the comparable height displacements to those in Fig. 4.8(b) were spread over a larger lateral dimension in the case of two closely spaced tetrahedrons so that the magnitude of $(\partial h/\partial i)$ $(\partial h/\partial j)$ becomes significantly reduced, where *i* and *j* denote either

x or *y* coordinate. Moreover, detailed comparisons of the spectroscopically determined pseudo-magnetic fields (as exemplified in Fig. 4.8(d) for the line-cut spectra along the white dashed line and in Fig. 4.8(e) for the line-cut spectra along the black dashed lines in Fig. 4.8(c)) with those determined topographically (Fig. 4.8(c)) were found to be in good agreement quantitatively, as shown in Fig. 4.8(h). In addition to verifying the consistency between the topographic and spectroscopic derivations of strain-induced pseudo-magnetic fields, the development of a topographic "wrinkle" between two near-by nanostructures is noteworthy. Moreover, the resulting pseudo-magnetic fields along the wrinkle direction appeared to form quasi-one-dimensional "channels" of nearly uniform pseudo-magnetic fields, whereas those perpendicular to the wrinkle exhibited relatively rapid and continuous spatial variations with alternating signs. This formation of a topographic wrinkle in graphene between two nanostructures provides a hint for developing controlled and spatially extended strain to achieve global inversion symmetry breaking, which is the subject of our following exploration.

4.5.3 Discussion

Although the strain-induced pseudo-magnetic fields do not break the global time-reversal symmetry, the gauge potentials A and A^* associated with the two valleys (*a.k.a.* two pseudospins) K and K′ in reciprocal space are opposite in sign and give rise to a peculiar zero mode.[62] This zero-mode corresponds to a condensate where the Dirac fermions are delocalized over the entire sample, and yet they remain alternately localized and anti-localized for the pseudo-spin projection in the real space, yielding local spontaneous time-reversal symmetry breaking.[62] Empirically, this spontaneous symmetry breaking may be manifested by the alternating presence and absence of the tunneling conductance peak at $n = 0$ for two inequivalent sublattices in graphene, which has been previously demonstrated by STS studies of molecular graphene. In this study, we also found that the point spectra of all strained regions exhibit statistically equal probabilities of the two zero modes. That is, the tunneling spectra at zero bias ($V = 0$) exhibit either a conductance peak or a conductance gap, as exemplified in Fig. 4.9(a) for the zero-bias conductance map of strained graphene over a Pd tetrahedron and the corresponding histograms in Fig. 4.9(b).

This finding, therefore, provides supporting evidence for spontaneous local time-reversal symmetry breaking due to strain-induced gauge potentials in real graphene.

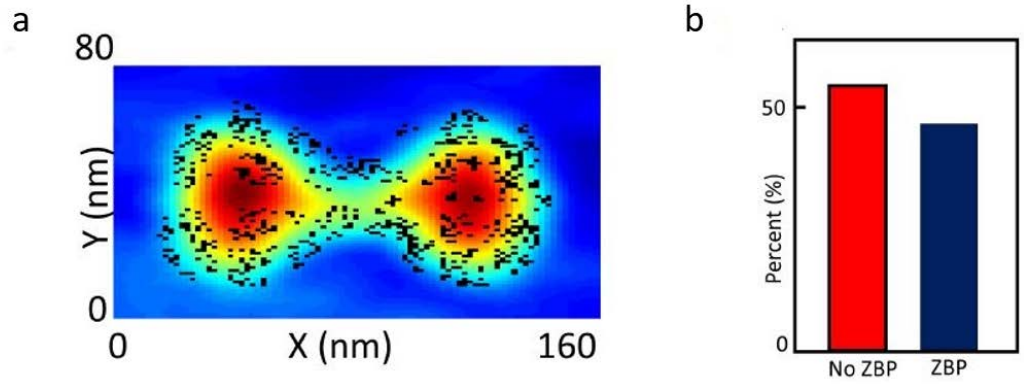

Figure 4.9 Scanning tunneling spectroscopic evidence for strain-induced spontaneous local time-reversal symmetry breaking and two zero modes in single layer graphene. (a) Spatially resolved map of the locations showing finite zero-bias conductance peaks (marked in black squares) in single layer graphene strained by two Pd-tetrahedron NCs shown in Fig. 4.8(b). (b) Histogram of the occurrence of zero-bias conductance peaks (denoted as "ZBP") and gaps (denoted as "No ZBP") for spectra taken in single layer graphene strained by two Pd-tetrahedron NCs shown in Fig. 4.8(b), showing statistically comparable probabilities for the appearance and absence of the zero-bias conductance peaks in the strained single layer graphene.

4.6 Conclusion

We have reviewed in this work the theoretical foundation for nanoscale strain engineering of graphene and have demonstrated the use of molecular dynamics techniques for designing various nanostructures to realize different patterns of pseudo-magnetic fields. We have also presented experimental evidence for strain-induced charging effects and giant pseudo-magnetic fields and described feasible empirical approaches based on nanofabrication techniques to realizing strain-engineering of pseudo-magnetic fields and valleytronics.

While the nanoscale strain engineering effects may be determined by STM, we emphasize that useful designs must ensure that the strain effects are extended to mesoscopic and even macroscopic scales for realistic device applications. Hence, the use of theoretical

simulations (such as the molecular dynamics techniques) to assist the design of collective nanostructures for desirable strain distributions and device performance can greatly improve the effectiveness of experimental implementations, which is the subject of our investigation in the next chapter.

Acknowledgments

I would like to thank Jiaqing Wang and Marcus Teague for their help on providing MD simulation results.

Chapter 5

GRAPHENE TRANSPORT MEASUREMENT AND GRAPHENE VALLEYTRONICS

5.1 Introduction

In a crystalline solid, charge and spin are intrinsic degrees of freedom of an electron. They have been widely studied and developed in academia and industry. In addition to charge and spin, another degree of freedom of an electron is valley, which is a local minimum in the conduction band or local maximum in the valence band. Like spin in spintronics, using the valley degree of freedom of an electron to store and carry information has attracted lots of attention in recent years because of the rise of 2D materials.

As we mentioned in Chapter 2, graphene with broken inversion symmetry has opposite Berry curvatures at K and K' valley. These Berry curvatures behave like an effective magnetic field in momentum space. A transverse valley current can be induced due to the anomalous velocity, which is called the valley Hall effect (VHE). In single layer graphene, inversion symmetry can be broken by atomically aligning single layer graphene on top of h-BN.[67] Moreover, giant non-local resistance with the order of quantum resistance can be observed without a magnetic field at low temperature, indicating the occurrence of the quantum valley Hall state.[70] In bilayer graphene, an electric field perpendicular to the graphene can break the inversion symmetry. Valley Hall transport has been demonstrated using nonlocal transport measurement in a Hall bar geometry with back-gated voltages.[71,72] Additionally, one-dimensional valley-polarized conducting channels associated with the protected chiral edge states of quantum valley Hall insulators have been demonstrated at the domain walls between AB- and BA-stacked bilayer graphene[73]. In this chapter, we demonstrate a different approach to manipulating the valley current in single layer graphene via nanoscale strain engineering.

5.2 Formation of periodic parallel graphene wrinkles for valley splitting and as topological channels

In order to generate strain on a large scale, we employed nanofabrication technology to develop regular arrays of nano-cones on silicon with processes described in the appendix. Two types of periodic arrays were explored. One was a triangular lattice structure and the other was a rectangular lattice structure, as shown by the SEM images in the top panels of Figs. 5.1(a) and 5.1(b), respectively. We found that the wrinkles induced on SLG by a triangular lattice had the tendency of forming along any of the three equivalent directions, as shown by the SEM image in the bottom panel of Fig. 5.1(a). In contrast, wrinkles induced by the rectangular lattice were generally well aligned and parallel to each other, as exemplified by the SEM image in the bottom panel of Fig. 5.1(b) and the AFM images in the top panels of Figs. 5.1(c) and 5.1(d). The corresponding pseudo-magnetic fields associated with the graphene distortions in the top panels of Figs. 5.1(c) and 5.1(d) are computed from the topography and shown in the bottom panels of Figs. 5.1(c) and 5.1(d).

It is worth noting that each extended graphene wrinkle results in four parallel, relatively uniform pseudo-magnetic fields along one direction and varying with alternating signs perpendicular to the channels, as illustrated in the bottom panel of Fig. 5.1(d). Given that the pseudo-magnetic fields as observed by K and K′ Dirac fermions are opposite in sign, the formation of parallel channels of pseudo-magnetic fields can effectively result in valley splitting and valley polarization. As illustrated by the theoretical simulations in the upper panels of Figs. 5.2(a)~(b), for valley-degenerate Dirac fermions incident perpendicular to the parallel channels of pseudo-magnetic fields, K- and K′-valley fermions can become spatially separated and the lateral separation will increase with the increasing number of wrinkles they pass over, provided that the average separation (d) of consecutive wrinkles is less than the ballistic length (l_B) of Dirac fermions.

Specifically, the ballistic length l_B is related to the conductance (G), mobility (μ), and carrier density (n_{2D}) of Dirac fermions in single layer graphene by the following relation:[4]

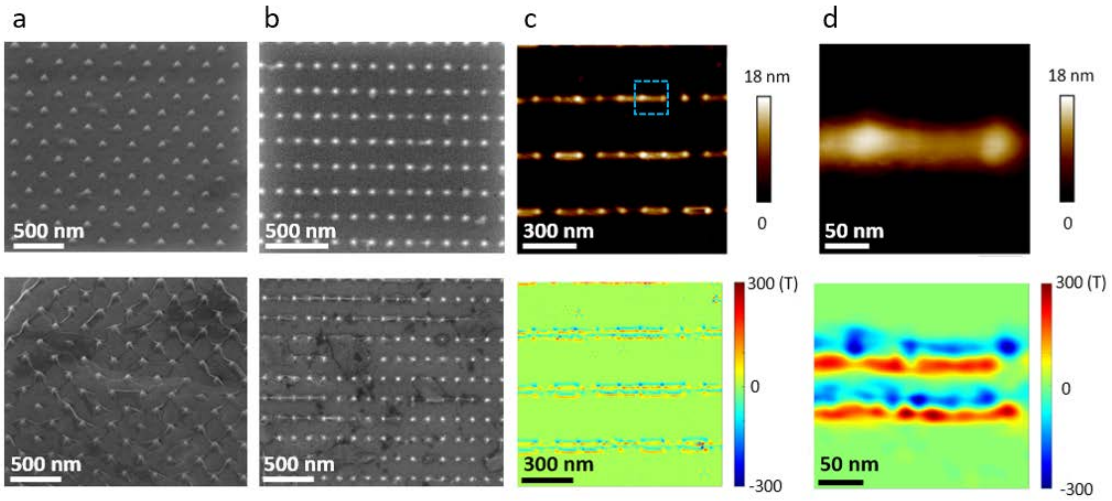

Figure 5.1 Extended strain effects induced by periodic arrays of nano-cones on graphene: (a) Top panel: SEM image of triangular arrays of cone-shaped nanostructures fabricated on a SiO2/Si substrate. Bottom panel: SEM image of monolayer-graphene/*h*-BN films on the triangular arrays shown in the top panel, showing graphene wrinkles appeared randomly along with three equivalent directions. (b) Top panel: SEM image of rectangular arrays of cone-shaped nanostructures fabricated on a SiO2/Si substrate. Bottom panel: SEM image of single layer graphene/*h*-BN films on the rectangular arrays shown in the top panel, showing graphene wrinkles parallel to the axis of closer spaced nanostructures. (c) AFM image (top panel) of three parallel graphene wrinkles and the corresponding map of pseudo-magnetic fields (bottom panel). (d) AFM image (top panel) of the graphene wrinkle enclosed by the blue dashed box in (c) and the corresponding map of pseudo-magnetic fields (bottom panel).

$$G = \frac{2e^2}{2\pi\hbar}(k_F l_B) = n_{2D} e\mu, \qquad l_B = \left(\frac{2\pi\hbar}{2e}\right)\frac{n_{2D}\mu}{k_F} = \left(\frac{\hbar}{e}\right)\mu\sqrt{\pi n_{2D}}, \tag{3.1}$$

where $k_F = (n_{2D}\pi)^{1/2}$ is the Fermi momentum, e is the electron charge, and $2\pi\hbar$ denotes the Plank constant. For typical values of n_{2D} = 10^{10} ~ 10^{12} cm^{-2} and μ ~ 10^5 cm^2/V-s for our PECVD grown graphene, we find that l_B = 120 nm ~ 1.2 μm. Thus, by proper nanofabrication to design the d value and by gating the PECVD-grown graphene for suitable n_{2D} and l_B, the condition $d < l_B$ can be satisfied within realistic experimental parameters to achieve valley splitting and therefore valley polarized currents.

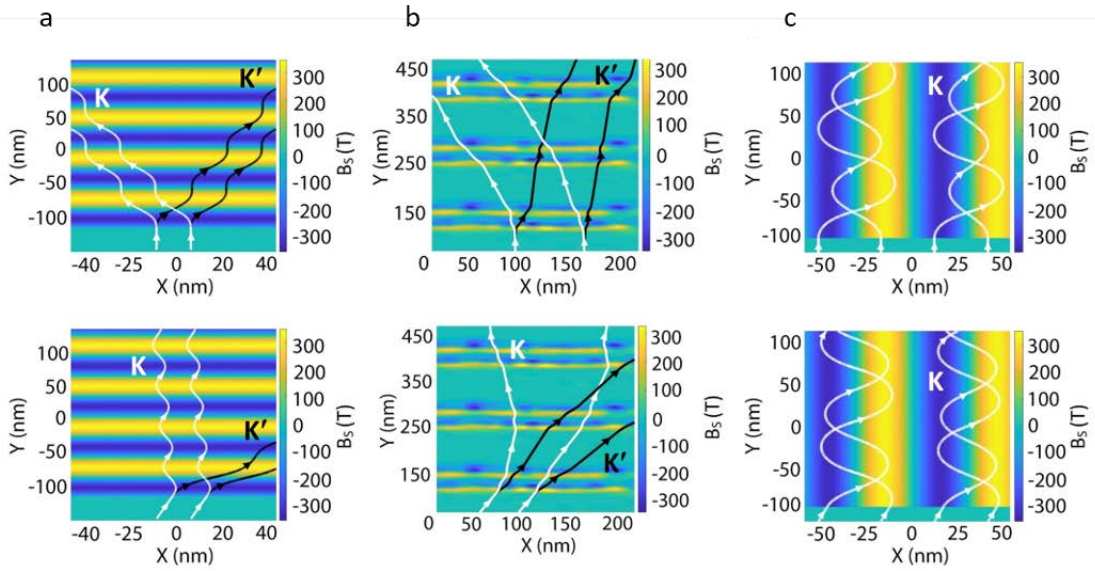

Figure 5.2 Parallel graphene wrinkles as topological channels for valley splitting and valley polarized propagation: (a) Simulations for parallel graphene wrinkles as a valley splitter, showing the trajectories of initially valley-degenerate (K + K') fermions from strain-free regions becoming split when injected vertically into regions with strain-induced periodic channels of pseudo-magnetic fields. Top panel: Trajectories of K and K' fermions for an incident angle perpendicular to the parallel channels ($\theta = 0°$). Bottom panel: Trajectories of K- and K'-valley fermions for an incident angle at $\theta = 15°$ relative to the normal vector of the parallel channels. (b) Top panel: Simulated trajectories of K and K' fermions for an incident angle perpendicular to the realistic strain-induced parallel pseudo-magnetic fields ($\theta = 0°$) shown in Fig. 5.1(c). Bottom panel: Simulated trajectories of K and K' fermions for an incident angle at $\theta = 15°$ relative to the normal vector of the realistic strain-induced parallel pseudo-magnetic fields shown in Fig. 5.1(c). (c) Simulations for parallel graphene wrinkles as a valley propagator, showing the collimation of valley-polarized fermions. Top panel: Trajectories of K-valley fermions incident at an angle parallel to the channels ($\theta = 90°$). Bottom panel: Trajectories of K-valley fermions incident at an angle $\theta = 75°$ relative to the normal vector of the parallel channels. (Simulations done by Jiaqing Wang)

In addition to yielding valley splitting as discussed above, the parallel distributions of alternating signs of pseudo-magnetic fields can serve as *topological channels* for chiral Fermions. As shown in Fig. 5.2(c), theoretical simulations for realistic arrays of nanostructures reveal that chiral Dirac fermions (*i.e.*, either K- or K′ fermions) can be preserved when propagating along the parallel channels of strain-induced pseudo-magnetic fields, as illustrated by the simulations shown in the top panel of Fig. 5.2(c). Additionally, valley-polarized Dirac fermions can even be collimated along the topological channels if

the incident angle deviates slightly from the channel direction, as exemplified in the bottom panel of Fig. 5.2(c). Thus, parallel graphene wrinkles can serve as an effective conduit for protected propagation of valley-polarized Dirac fermions.

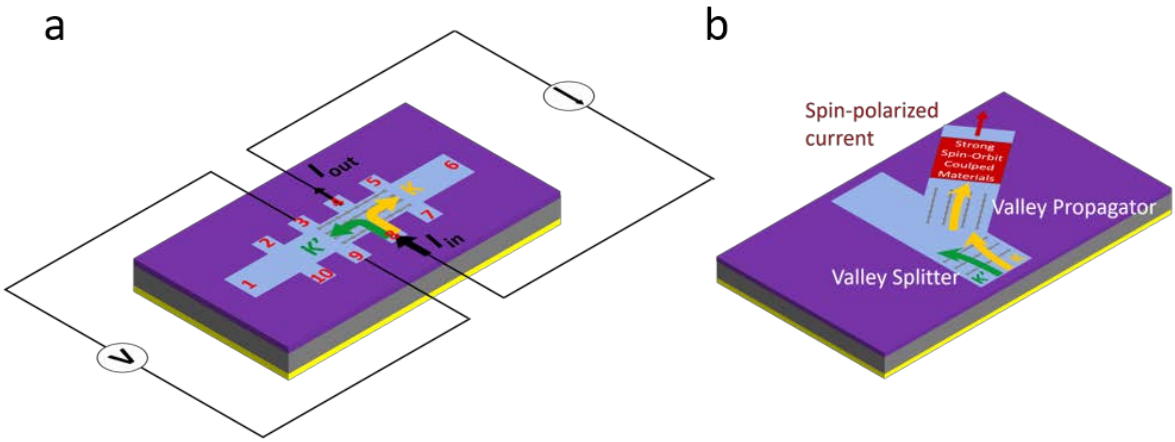

Figure 5.3 Schematics of the experimental configurations for graphene-based valleytronics and spintronics. The blue-shaded area represents a patterned single layer graphene/*h*-BN sample with strain-engineered periodic parallel wrinkles, and the purple region denotes a thin-layer of SiO_2 on top of a Si-substrate (grey region). (a) A graphene valley-Hall transistor: For graphene wrinkles parallel to the long axis, an incident current (I_{in}) perpendicular to the wrinkles will lead to splitting of the K and K′ Dirac fermions. Therefore, in addition to the longitudinal resistance (R) that may be determined either from $R = (V_{25}/I_{16})$ or equivalently from $(V_{10,7}/I_{16})$, a non-local resistance (R_{NL}) may be detected from $R_{NL} = (V_{39}/I_{48})$ as shown above, or equivalently from (V_{57}/I_{48}). By placing the graphene Hall bar on the SiO_2/Si substrate and attaching a back gate to the Si, the Fermi level of the graphene can be controlled relative to the Dirac point by tuning the gate voltage (V_G) so that a sharp peak in R_{NL}-vs.-V_G is expected when the Fermi level coincides with the Dirac point.[67] This configuration is, therefore, a field effect transistor. (b) A valleytronic-to-spintronic device: The combination of graphene-based valley-splitters and valley-propagators can lead to the generation of valley-polarized currents, as schematically illustrated by the yellow arrows for the trajectory of K-valley Dirac fermions. The injection of valley-polarized currents into a strong spin-orbit-coupled material can further lead to outgoing spin-polarized currents for spintronic applications.

5.3 Nanoscale strain engineering of graphene-based valleytronic devices

The formation of periodic parallel graphene wrinkles by means of modern nanofabrication technology provides a pathway towards realizing controlled strain-induced effects for the scalable development of graphene-based valleytronic devices. For instance, by patterning

a valley-Hall device configuration with the long-axis parallel to graphene wrinkles as schematically illustrated in Fig. 5.3(a), strong non-local resistance and valley-Hall effects may be detected under proper back-gated voltages, leading to a valley-Hall transistor similar to the previous observation of the valley Hall effect in exfoliated single layer graphene-on-*h*-BN flakes.[67] It is also conceivable to obtain highly valley-polarized currents through the combination of valley-splitters (Figs. 5.2(a) ~ (b) and valley-propagators (Fig. 5.2(c), as conceptually illustrated in Fig. 5.3(b). Finally, we note that many such devices can be developed by means of scalable and reproducible nanofabrication technology on large-area PECVD-grown graphene sheets, thus making the applications of graphene-based nanoscale valleytronic/spintronic devices closer to reality.

5.4 Valley Hall effect of strained graphene

To detect the valley Hall signal, we fabricated valley Hall devices as shown in Fig. 5.4(b). and the measurement was performed using a low-frequency (17Hz) lock-in technique. The nonlocal resistance R_{NL} was measured at room temperature in the same configuration reported in other literature.[67,70] However, a nonlocal voltage can also be measured because of stray currents, which can be described by the van der Pauw relation

$$R_{\mathrm{NL}} \sim \rho_{xx} \exp\left(-\pi \frac{\mathrm{L}}{\mathrm{w}}\right), \tag{5.1}$$

where L is the distance between the current path and voltage probes and w is the device width. For our strained device, L = 8 μm and w = 4 μm. For the untrained sample, L = 4 μm and w = 4 μm as illustrated in Fig. 5.4(a) and (b). In order to compare the measured R_{NL} of the strained and unstrained devices under identical geometry, R_{NL} of unstrained devices is scaled down by a factor of $\exp\left(-\pi \frac{\mathrm{L}}{\mathrm{w}}\right)$ as shown in Fig. 5.4(c). Our measured R_{NL} of strained sample is more than two orders of magnitude larger than the R_{NL} of the unstrained sample, which is totally not compatible with the van der Pauw relation. The dramatical difference of the R_{NL} of the unstrained and strained sample suggests that we've measured the valley Hall signal on the strained sample.

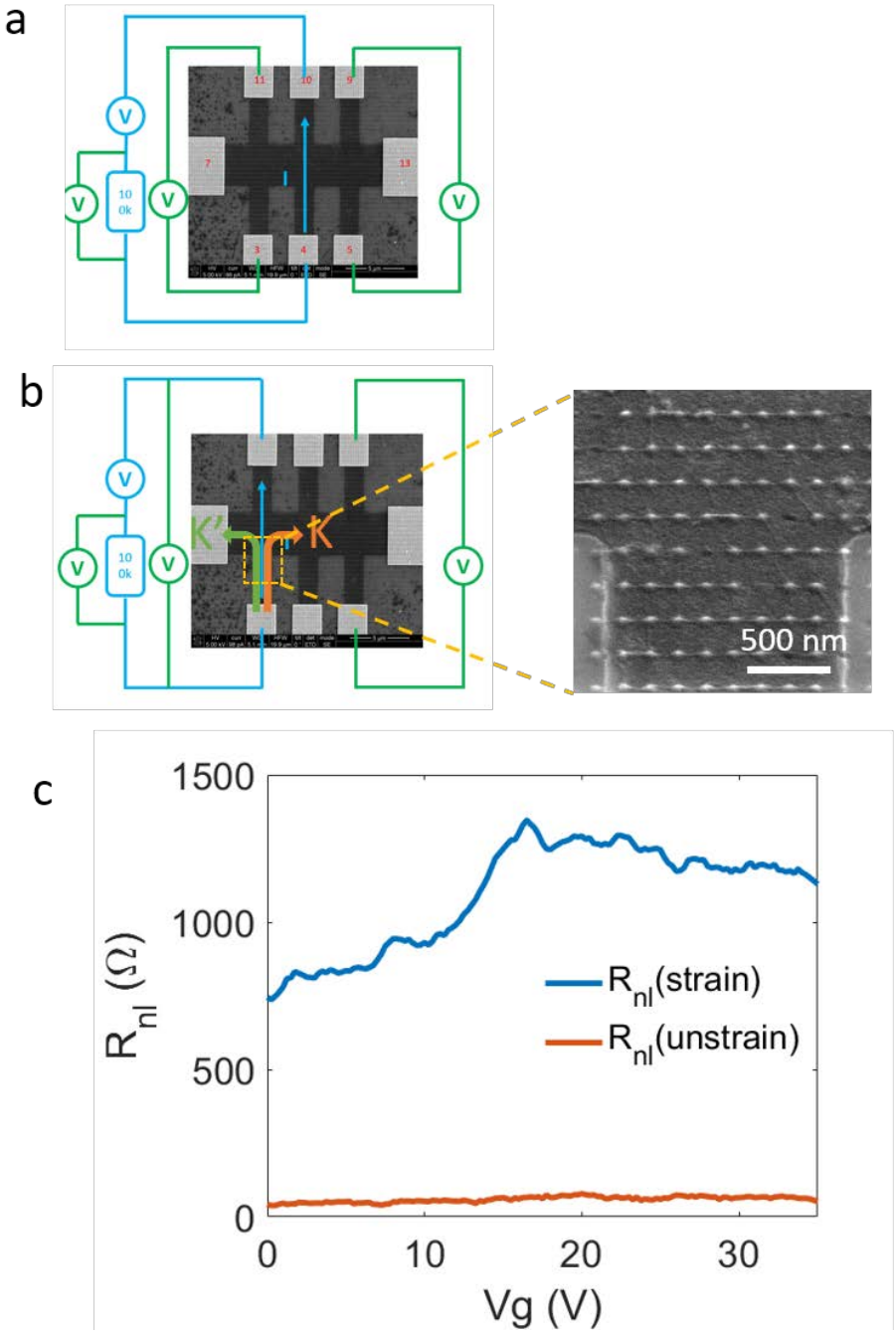

Figure 5.4 Schematic of the nonlocal resistance measurement on an (a) unstrained and (b) strained sample. Zoom-in SEM image shows graphene wrinkles on the periodic arrays. (c) Comparison of the measured R_{NL} of strained and unstrained devices as a function of the back gate voltage (V_g), which is associated with the 2D carrier density. R_{NL} of unstrained devices is scaled down by a factor of $\exp\left(-\pi\frac{L}{w}\right)$. The peak position associated with R_{NL} indicates the Dirac point.

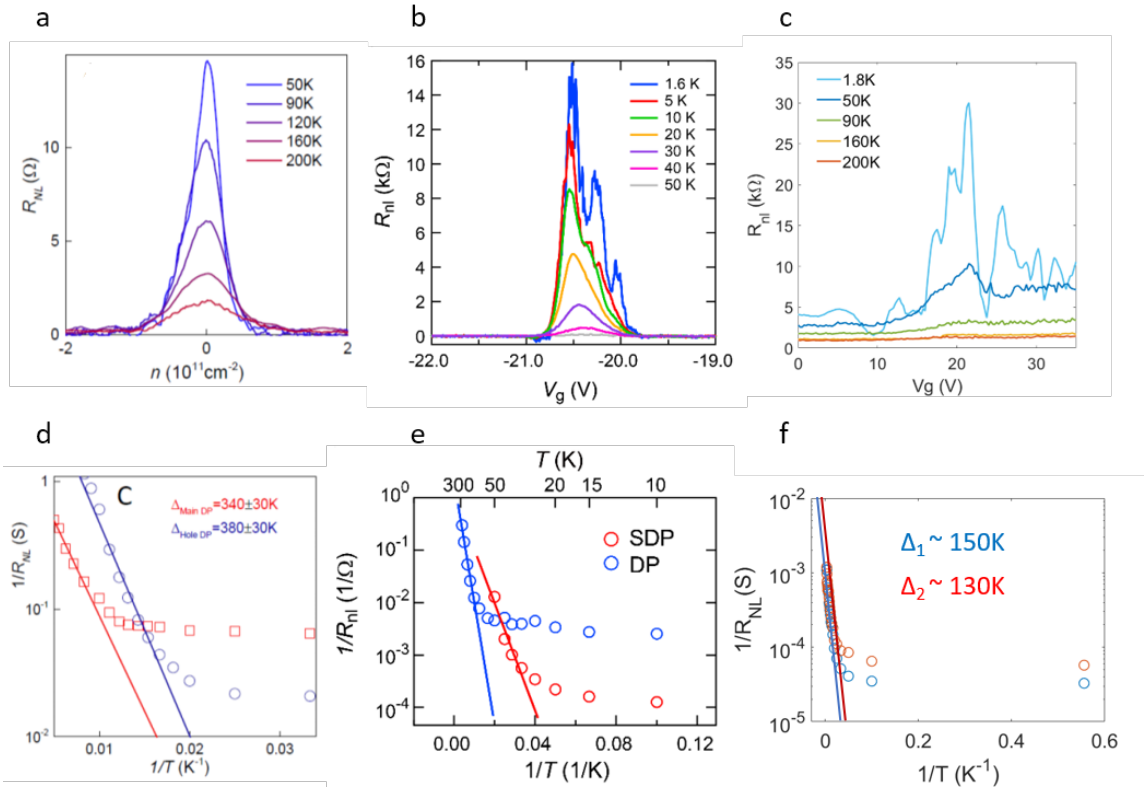

Figure 5.5 Temperature dependence of nonlocal resistance R_{NL}. (a) Adapted from [67]. (b) Adapted from [70]. (c) Our data. (d) ~ (f) Arrhenius-type plots of R_{NL} from (a) ~ (c), respectively. In (e) DP denotes "Dirac point" and SDP denotes "second Dirac point".

Next, we measured R_{NL} of strain sample as a function of back gate voltage at different temperatures and compare our results with those by Gorbachev *et al.* and Komatsu *et al.*[67,70] for SLG aligned on h-BN as shown in Fig. 5.5. We found consistent trends as a function of temperature and very large nonlocal signals. Besides, at low temperature, the R_{NL} signals became narrower and we started seeing some additional peaks, which will be discussed later. We collected the temperature dependence of maximum R_{NL} and plotted $1/R_{NL}$ as a function of 1/T. We also found a similar trend of our data (Fig. 5.5(f)) compared to the typical R_{NL} of valley Hall signals (Fig. 5.5(d) and (e)). The temperature dependence of R_{NL} in Fig. 5.5(f) can be described by the Arrhenius formula and the bandgap thus derived is around 150K and 130K, respectively.

When the temperature dropped to 1.8K, we can see very clear peaks on the R_{NL}. We can use the following equations to calculate the energy separation of these peaks. The capacitance of the SiO_2 substrate is:

$$C = \frac{Q}{V} = \frac{n_{2D} e A}{V_g - V_{Dirac}} = \frac{\varepsilon_r \varepsilon_0 A}{d}, \tag{5.2}$$

where n_{2D} is the carrier density, e is electron charge, A is the area of the substrate, d is the thickness of SiO_2 = 250 nm, V_g is the back gate voltage, ε_r is SiO_2 dielectric constant = 3.9, and ε_0 = 8.85 x 10^{-12} F/m is vacuum permittivity. So n_{2D} can be rewritten as

$$n_{2D} = \frac{\varepsilon_r \varepsilon_0 (V_g - V_{Dirac})}{ed}. \tag{5.3}$$

The graphene energy eigenstate is

$$E(k) = \hbar v_F k_F = \hbar v_F \sqrt{n_{2D}\pi}, \tag{5.4}$$

where $k_F = \sqrt{n_{2D}\pi}$ is the Fermi wave vector, so

$$E(V_g) = \hbar v_F \sqrt{\frac{\pi \varepsilon_r \varepsilon_0 (V_g - V_{Dirac})}{ed}}. \tag{5.5}$$

Fig. 5.6(a) shows the R_{NL} data of a strain sample as a function of the back gate voltage. We found that peaks in the R_{NL} are associated with the pseudo-magnetic field-induced Landau levels at a single valley. The R_{NL} is found to show peaks at quantum resistance values of $h/e^2 \approx$ (25.8kΩ), $h/2e^2$ and $h/3e^2$ over the measured range of the Vg. The observed phenomena can be understood as the manifestation of quantized Landau levels (for indices n = 0, ±1, ±2…) at a single valley due to strain-induced pseudo-magnetic fields and valley splitting, as illustrated in Fig. 5.6(b). In particular, the spin-degree of degeneracy for each Landau level is found to further split into two energy levels (for indices n = $0_{\pm}$, $\pm 1_{\pm}$, $\pm 2_{\pm}$…) with an energy separation of $\Delta E_0 = e^2/(4\pi\varepsilon_0 l_B)$ due to strong Coulomb interactions among strain-localized carriers. Thus, electron spins become spontaneously polarized in order to reduce the Coulomb repulsion, leading to spontaneous symmetry breaking and ferromagnetism. Here l_B denotes the magnetic length associated with an averaged pseudo-magnetic field B and is given by $l_B = \sqrt{\hbar/(eB)}$.

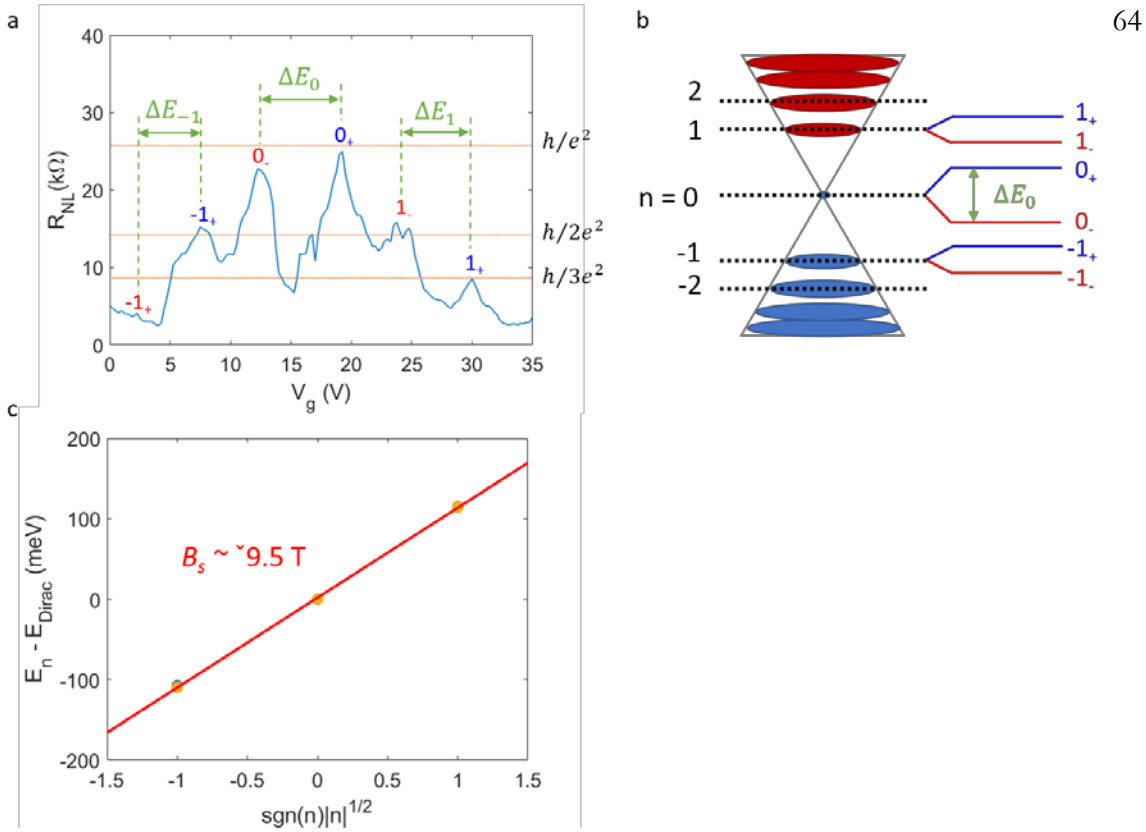

Figure 5.6 (a) The R_{NL} of a strained sample as a function of the back gate voltage. R_{NL} shows distinct quantized oscillation associated with different Landau Levels. (b) Schematic illustration of the pseudo-magnetic field-induced Landau levels and further spin-split levels for the Dirac cone at either the K or K' valley. (c) Magnitude of the pseudo-magnetic field is determined by the plot of $E - E_{Dirac}\ (eV)\ vs.\sqrt{n}$, where n is an integer. The slope is proportional to the pseudo-magnetic field. For the energy separations shown in Fig. 5.6(a), the corresponding averaged pseudo-magnetic field is $|B|$~ 9.5T, which is consistent with $\Delta E_0 \approx$ 84meV.

We compare the energy separation with Eq. 1.22 and plot $E - E_{Dirac}\ (eV)\ vs.\sqrt{n}$ as shown in Fig. 5.6(c), and calculate the magnitude of the corresponding effective pseudo-magnetic fields to be ~ 9.5T. Although STM/STS study shows very strong local pseudo-magnetic fields in certain regions, these strain-induced wrinkles are actually very far apart (300 ~ 400 nm). If we average over the total area by the effective mean free path, the non-local effective $\langle B_s(x,y)\rangle$ value is much smaller than the maximum value of $B_s(x,y)$ according to Eq. (4.1), as shown in Fig. 5.7(b).

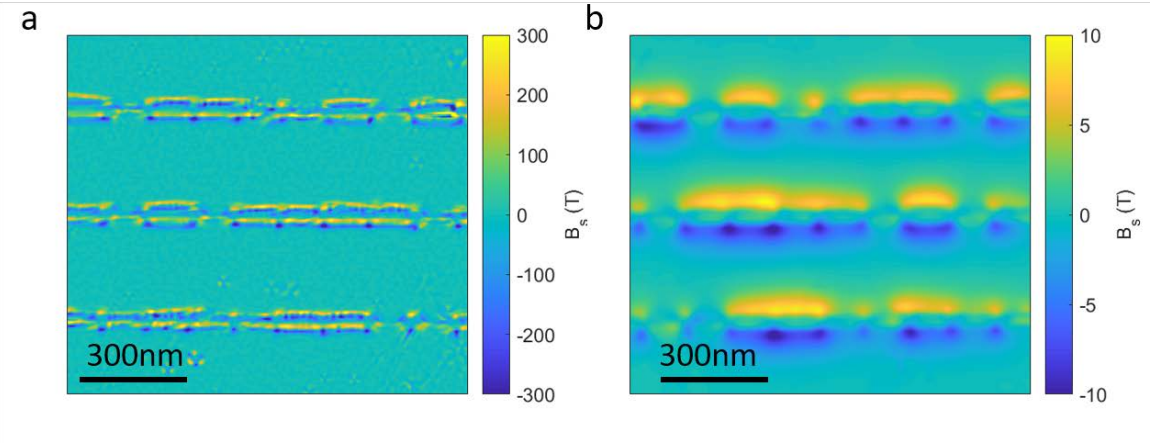

Figure 5.7 (a) The pseudo-magnetic field map calculated from the topography of graphene wrinkles. (b) Calculated map of effective pseudo-magnetic field $\langle B_s(x,y)\rangle$ by Eq. 4.1. The effective mean free path l_0 was chosen as 35 nm in the calculation.

In addition to the quantum valley Hall effect demonstrated above, spin polarization due to spontaneous symmetry breaking leads to another quantum phenomenon, the quantum anomalous Hall effect, as shown in Fig. 5.8(a) for the measurement configuration and in Fig. 5.8(b) for the detected anomalous Hall signals by applying electrical current across contacts 1-5 and detecting the Hall resistance (R_{xy}) across contacts 4-6. In the absence of any external magnetic fields, the Hall resistance R_{xy} cannot possibly appear unless there is finite magnetization due to the presence of ferromagnetism. Our strained graphene device not only exhibits R_{xy} signals larger than the longitudinal resistance (R_{xx} measured across contacts 2-4) but also reaches the values of quantum anomalous Hall resistance of h/e^2 and $h/2e^2$ for Fermi levels comparable to the same quantized energies where quantum valley Hall effect appears. This is the first observation of strain-induced quantum anomalous Halle effects, which implies that strained graphene devices can induce ferromagnetism and spin-polarized currents for applications to non-dissipative spintronics.

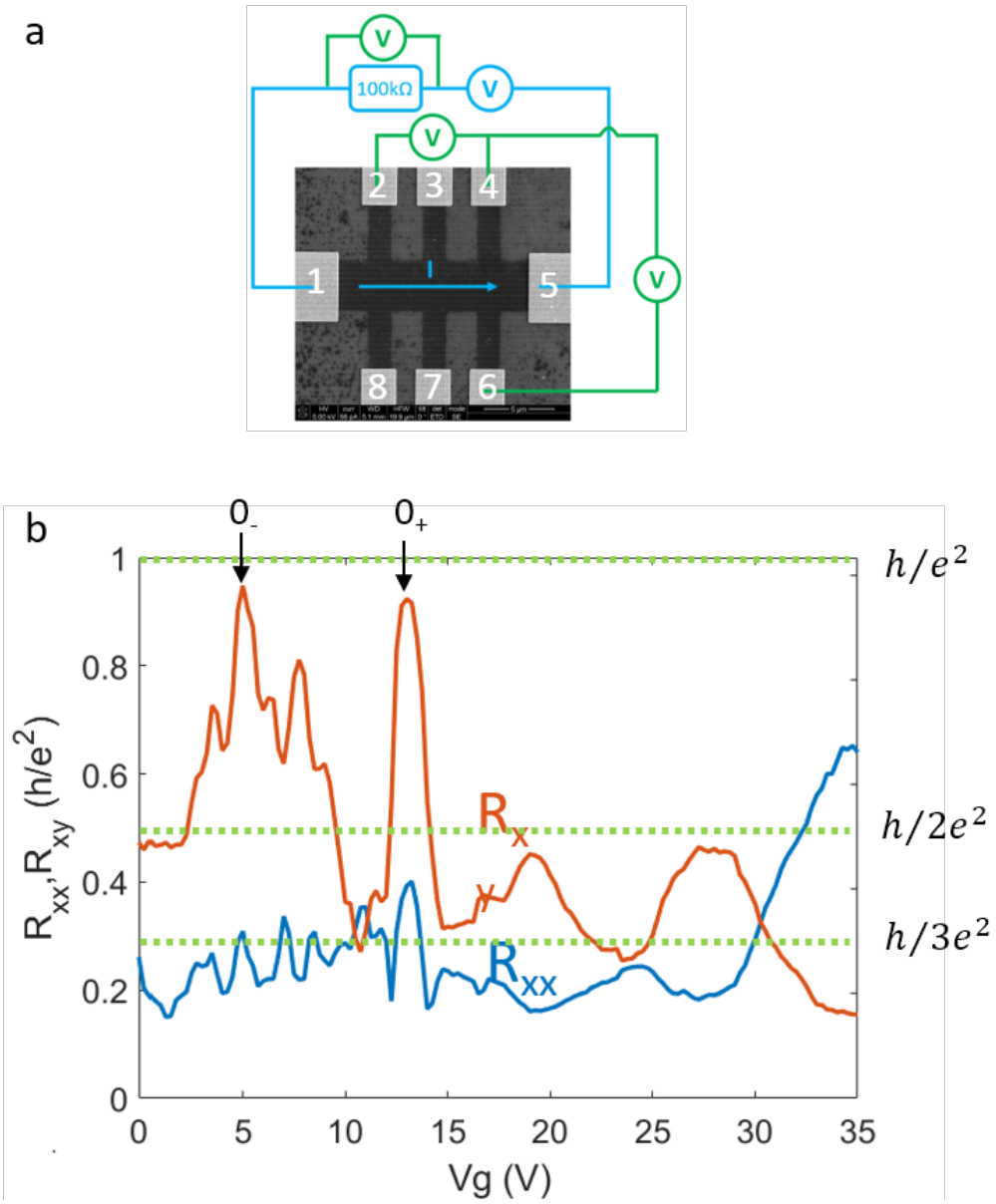

Figure 5.8 (a) Schematic setup of Hall measurement. (b) Comparison of the longitudinal resistance (R_{xx}) and Hall resistance (R_{xy}) vs back gate voltage Vg at zero magnetic field at 1.8K, showing peaks at quantum anomalous Hall resistance values h/e^2 and $h/2e^2$ in R_{xy} at the spin-split zeroth Landau levels (0_+ and 0_-) and first Landau levels ($+1_+$ and $+1_-$), respectively.

5.5 Conclusion

Valley Hall effect can be obtained on a system with broken inversion symmetry but without any strain. In contrast, Quantum Hall effect can be manifested in the graphene system under real magnetic field, but there is no Hall signal in the absence of magnetic field. In our strain devices, we have both valley Hall signals as well as pseudo-magnetic field-induced quantum oscillations in zero magnetic field. Quantum oscillations will give rise to the oscillation in longitudinal resistance, and at the same time, such oscillations can be manifested in the R_{NL} signal. The much larger R_{NL} in strained devices than that in unstrained devices also suggests we've seen valley Hall effect

We have demonstrated that periodic graphene wrinkles as topological channels for valley splitting and protective valley propagation, leading to valley Hall effect and pseudo-magnetic field quantum oscillations. The presence of valley Hall signals is manifested by the very clear strained induced R_{NL}, and the R_{NL} temperature dependence is consistent with theoretical predictions for the valley Hall induced effect. In addition, we have observed pseudo-magnetic field-induced quantum oscillations, and further found that the valley Hall signals approach the quantum valley Hall value at 1.8 K.

Chapter 6

HIGH-YIELD SINGLE-STEP CATALYTIC GROWTH OF GRAPHENE NANOSTRIPES BY PECVD

6.1 Introduction

Among many intriguing properties and promising applications of graphene-based materials,[1,4,74] reduced dimensional graphene nanostructures, such as graphene nanoribbons (GNRs) that often refer to one-dimensional crystals with nanoscale widths, have attracted much attention for their quantum confinement effects in extremely narrow ribbons,[75,76] novel edge characteristics,[4,77–79] mechanical strength,[80,81] and a wide range of technological prospects in such areas as nano-electronics,[82–86] spintronics,[87,88] plasmonics,[89–91] biosensors,[92,93] energy storage,[94] and energy production.[95]

One of the primary challenges to fully realize the technological promises of reduced dimensional graphene nanostructures is to reliably produce a large number of high-quality nanomaterials with large aspect ratios. In general, the structural and physical properties of reduced dimensional graphene nanostructures are strongly depending on the synthesis method. To date, the best-known methods for synthesizing quasi-one-dimensional graphene nanostructures include the following primary categories: [1] The top-down approach, which utilizes lithographic techniques to produce GNRs from two-dimensional graphene sheets on a substrate. The quantities of GNRs thus produced are limited due to the time-consuming lithographic processes, and the edges of these GNRs are usually jagged.[96,97] [2] The bottom-up approach, which may be further divided into the surface-assisted[98,99] and solution-phase synthesized[100–106] approaches. The surface assisted method involves pre-synthesis of polymer chains on metallic substrates and has the advantage of achieving atomically precise armchair- or zigzag-edges.[78,79,98,99] However, this approach generally involves multiple steps of processing, which leads to very low yields and relatively short GNRs. Moreover, these GNRs are not easily transferrable to other substrates. Similarly, the solution-phase synthesized approach also involves multiple steps and the resulting GNRs exhibit a range of controlled widths on the order of 1 ~ 2 nm and typical lengths over 100 nm.[101–107] While both

types of bottom-up approaches can achieve better control of the structures of GNRs, the complexity in the synthesis procedures and the relatively low yields are not ideal for mass production in large-scale applications. [3] Unzipping carbon nanotubes (CNTs): Multi-walled CNTs can be unzipped along the longitudinal direction to form GNRs.[108,109] Compared to the first two methods, this approach has the potential for mass production and lower costs. However, the process is time-consuming and also requires the initial mass production of CNTs. The GNRs thus produced also contain excess metallic impurities.[110,111] [4] Growth by thermally assisted plasma-enhanced chemical vapor deposition (PECVD): Synthesis of vertically-oriented graphene "nanowalls" or "nanosheets" by means of PECVD have been reported for a variety of precursor gases.[36,112] However, this method faces three major challenges[36]: First, all processes reported to date involve multiple steps of pretreatment of the substrates as well as high-temperature (ranging from 500 ºC to 1150 ºC) substrate heating and high plasma power (>10^2 W and up to ~ 10^3 W) during the graphene growth. Second, the yields are generally too low to be practical for mass production. Third, the morphology and structures of vertically grown graphene nanosheets are not well controlled[36,112] because the growth mechanisms under different growth parameters and precursor molecules are not fully understood.

To overcome the aforementioned challenges, we report in this work a new single-step seeded growth method of "graphene nanostripes" (GNSPs) by PECVD techniques that can achieve high-yield and high-quality growth of GNSPs reliably without any active heating. The lengths of these GNSPs range from a few to tens of micrometers and the widths range from tens to hundreds of nanometers. As a result, they exhibit large aspect ratios (typically from 10:1 to >~130:1) but do not manifest the effects of quantum confinement. Further, their widths are typically narrower than most nanowalls and nanosheets reported to date.[36,112] Therefore, we refer these quasi-one-dimensional nanostructures to "graphene nanostripes" (GNSPs) to indicate their large aspect ratios and to differentiate them from GNRs that exhibit quantum confinement and also from graphene nanosheets[36] or nanowalls[112] that are generally wider and are with smaller aspect ratios than our GNSPs.

In comparison with our single-step PECVD growth process of high-quality large graphene sheets laterally on copper substrates without active heating,[29] these GNSPs of large aspect ratios are grown vertically on various transition-metal substrates by PECVD with the addition of substituted aromatics such as 1,2-dichlorobenzene (1,2-DCB), 1,2-dibromobenzene (1,2-DBB), 1,8-dibromonaphthalene (1,8-DBN) and toluene as the seeding molecules. Among these substituted aromatics, we find that 1,2-DCB is most effective for the growth of GNSPs at room temperature. Therefore, we focus hereafter on the studies of PECVD-grown GNSPs that are seeded by 1,2-DCB, and only briefly discuss representative findings associated with GNSPs grown with 1,2-DBB and 1,8-DBN for completeness.

The entire growth process occurs in a single step within less than 20 min at a relatively low plasma power (60 W), and the resulting GNSPs exhibit large aspect ratios and high yields. Studies of the Raman spectroscopy, scanning electron microscopy (SEM), transmission electron microscopy (TEM), energy dispersion x-ray spectroscopy (EDS), ultraviolet photoemission spectroscopy (UPS) and electrical conductivity all confirm the high quality of the GNSPs thus obtained. Based on these experimental findings together with data from the residual gas analyzer (RGA) spectra and optical emission spectroscopy (OES) taken during the plasma process, we propose a growth mechanism and suggest that the introduction of substituted aromatics in the hydrogen plasma plays a critical role in achieving rapid vertical growth of GNSPs with high aspect ratios.

6.2 Experimental

6.2.1 Experimental Setup

The PECVD system is schematically illustrated in Fig. 2.1(a). It consists of an Evenson cavity and a power supply (MPG-4, Opthos Instruments Inc.) to generate plasma. The 1,2-DCB or 1,2-DBB precursor is stored in a quartz container and attached to the growth chamber via a leak valve and a quarter-turn, shut-off valve. A residual gas analyzer (RGA) is used to monitor the partial pressure of precursor and by-products. Because 1,8-DBN is in a solid form at room temperature, it was placed in a quartz boat and was heated up in a furnace as shown in Fig. 6.1.

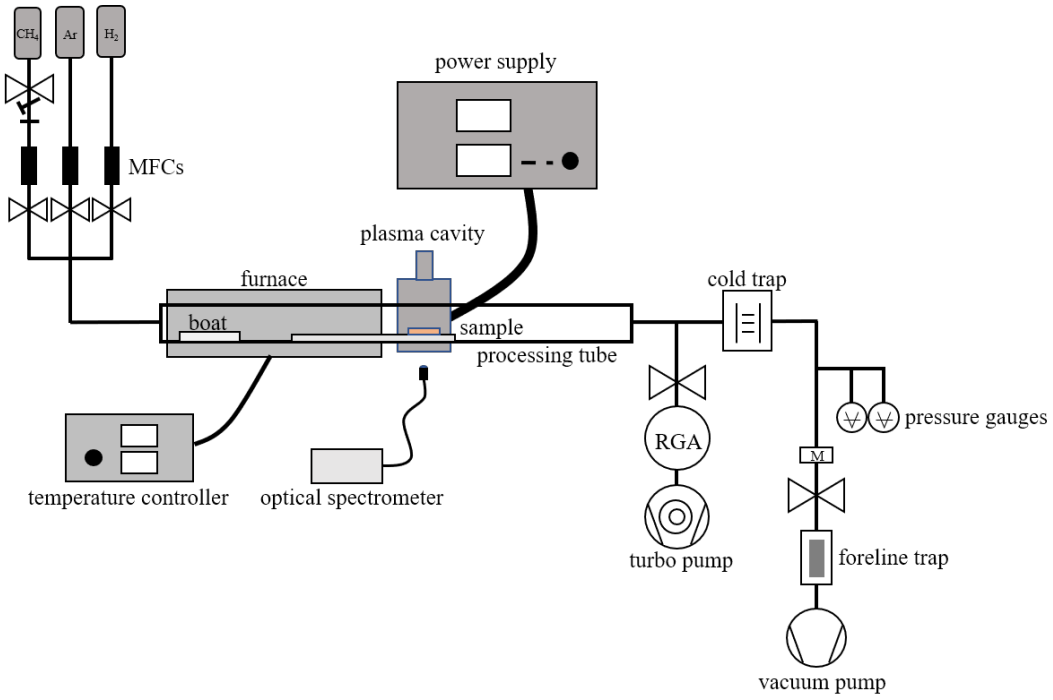

Figure 6.1. A schematic of the experimental setup used for 1,8-DBN. The precursor was heated from 60 °C to 100 °C to introduce different precursor partial pressures.

6.2.2 Seeded growth of GNSPs

The quartz tube was pumped down to 27 mTorr. During the growth, the total pressure of the tube was maintained at 500mTorr with 2 sccm hydrogen. The additional methane and 1,2-DCB were controlled by a precision leak valve and the partial pressure was monitored by an RGA. Typical methane and 1,2-DCB partial pressures were (10 ~ 900) × 10^{-9} Torr and (1 ~ 10) × 10^{-9} Torr, respectively, as measured in the RGA. Hydrogen plasma was formed away from the substrate and then moved to the substrate in order to prevent any plasma transient damages. Typical plasma power ranged from 40 to 60 W with a plasma size of 1 ~ 2 cm^3, and growth time ranged from 0.5 to 20 min.

The vapor pressure of 1,2-dichlorobenzene (1,2-DCB) at room temperature is 1.36 mmHg, and 1,2-dibromobenzene (1,2-DBB) is predicted to have a vapor pressure of 0.101 mmHg. Since the vapor pressure of 1,2-DBB is one order of magnitude smaller than that of 1,2-DCB, the size of the GNSPs grown by 1,2-DBB tends to decrease due to fewer amounts of precursors available to form GNSPs. For 1,8-DBN, the temperature of the furnace ranged from 60 °C to 100 °C, which corresponded to a range of different precursor partial pressures.

6.2.3 Characterization

The PECVD-grown GNSPs were characterized by Raman spectroscopy, UPS, XPS, SEM, TEM, and electrical conductivity studies. Raman spectra were taken via a Renishaw M1000 micro-Raman spectrometer system using a 514.3 nm laser (2.41 eV) as the excitation laser source. The laser spot size was ~1 mm in diameter and the exposure time was 30 s. A 50× objective lens with a numerical aperture of 0.75 and a 2400 lines/mm grating was chosen during the measurement to achieve a better signal-to-noise ratio. The UPS was performed via the Kratos-Ultra-XPS model which uses a magnetic immersion lens with a spherical mirror and concentric hemispherical analyzers with a delay-line detector for both imaging and spectroscopy. He I (21.2 eV) were used as excitation sources for UPS measurement in an ultrahigh vacuum chamber with a base pressure of 2×10^{-10} Torr. The SEM images were taken by a FEI Nova 600 SEM system with the following parameters: acceleration voltage = 5 kV, beam current = 98 pA, and working distance ~5 mm. The TEM measurements were performed on a FEI Tecnai TF30 STEM (TF30) with an operating voltage of 300 kV. The electrical conductivity measurements were made by means of the four-probe method on GNSPs aligned on patterned electrodes via electrophoresis techniques.

6.3 Results and analysis

The seeded PECVD growth process is schematically illustrated in Fig. 6.2(a). We use 1,2-DCB to act as seeds for vertically aligned carpets of GNSPs grown on Cu surfaces. The hydrogen plasma with a slight trace of CN radicals is used to remove the surface copper oxide and expose fresh copper surface upon which 1,2-DCB molecules can seed, resulting in the initial formation of vertical GNSPs. Additionally, methane is introduced into the hydrogen plasma as another carbon source to enhance the growth rate. We have also demonstrated the feasibility of using other carbon-based, substituted aromatics such as 1,2-DBB, 1,8-DBN and toluene as precursors and different transition-metal substrates (such as Ni foam and Ni foil besides Cu foil), as exemplified in Fig. 6.3 and Fig. 6.4.

The PECVD system is equipped with a residual gas analyzer (RGA) and an optical emission spectrometer (OES), which are used to monitor the gases in the growth chamber during the

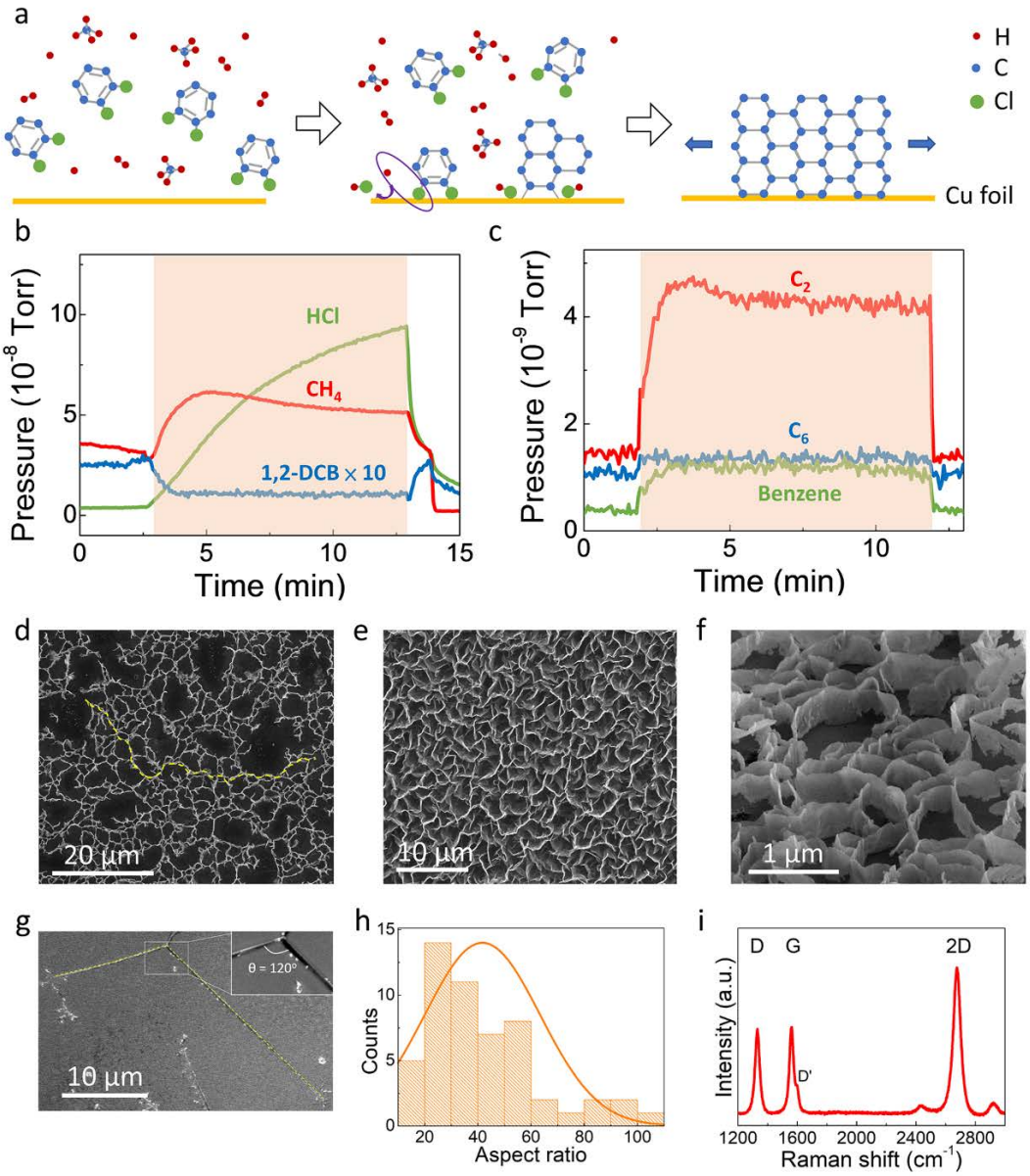

Figure 6.2. (a) Schematic illustration of the seeded growth process of PECVD-grown GNSPs. (b) ~ (c) RGA spectra of gas pressures in the growth chamber as a function of time, where the shaded area indicated the duration of the plasma process. (d) ~ (e) Two representative SEM images of the top view of GNSPs on Cu foil fabricated by PECVD with 1,2-DCB molecules for 10 min (f) SEM image of the tilted view (at 52º) of GNSPs shown in (d), revealing a relatively constant width of ~500 nm for all GNSPs within the field of view. (g) SEM image of one GNSP isolated from the batch of GNSPs in (e) and placed on a silicon substrate, showing a length of ~66 mm (main panel) and a three-fold branching point near the end of the GNSP (inset). The GNSP in the main panel is highlighted by yellow dashed lines for clarity. (h) A representative histogram of the aspect ratios of GNSPs obtained from multiple sets of SEM images within their field of view. (i) A typical Raman spectrum of GNSPs.

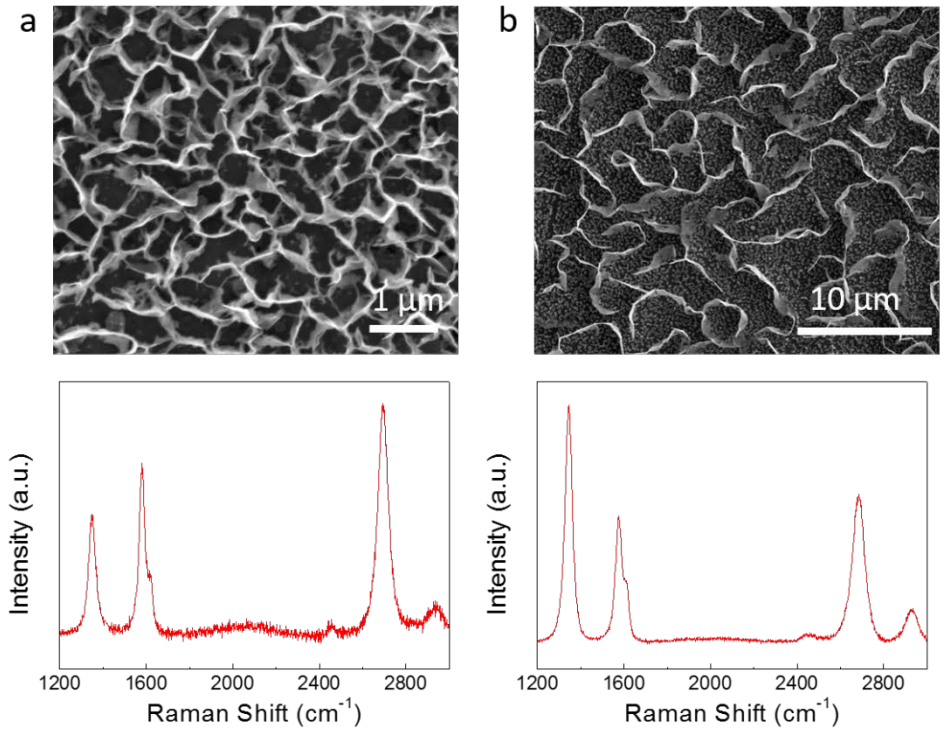

Figure 6.3. (a) SEM image (top) and Raman spectrum (bottom) of GNSPs on Cu foil grown by 1,2-DBB for 10 minutes. (b) SEM image (top) and Raman spectrum (bottom) of GNSPs on Cu foil grown by 1,2-DBN for 10 minutes. 1,2-DBN was heated up to 80°C to produce enough vapor pressure.

PECVD process. Two representative RGA spectra are shown in Fig. 6.2(b) and (c), where the shaded band indicates the time interval from turning on to turning off the plasma. The spectrum in Fig. 6.2(b) reveals that hydrogen chloride (HCl) is a main byproduct of the seeded PECVD growth process. This indicates that hydrogen radicals can react with chlorine in 1,2-DCB to form hydrogen chloride and render the resulting vertical GNSPs mostly free of chlorine. Additionally, substantial amounts of C_2 and C_6 radicals together with C_6H_6 molecules are found during the plasma growth process, as shown in Fig. 6.2(c).We note that while C_2 is common radicals found in all previously reported thermally assisted PECVD growth,[36] the eminent presence of C_6 radicals and C_6H_6 molecules are unique in our low-temperature PECVD process.

We have also monitored the optical emission spectra (OES) of the plasma during the growth process as a function of the 1,2-DCB/CH4 partial pressure ratio, as shown in Fig. 6.5. We

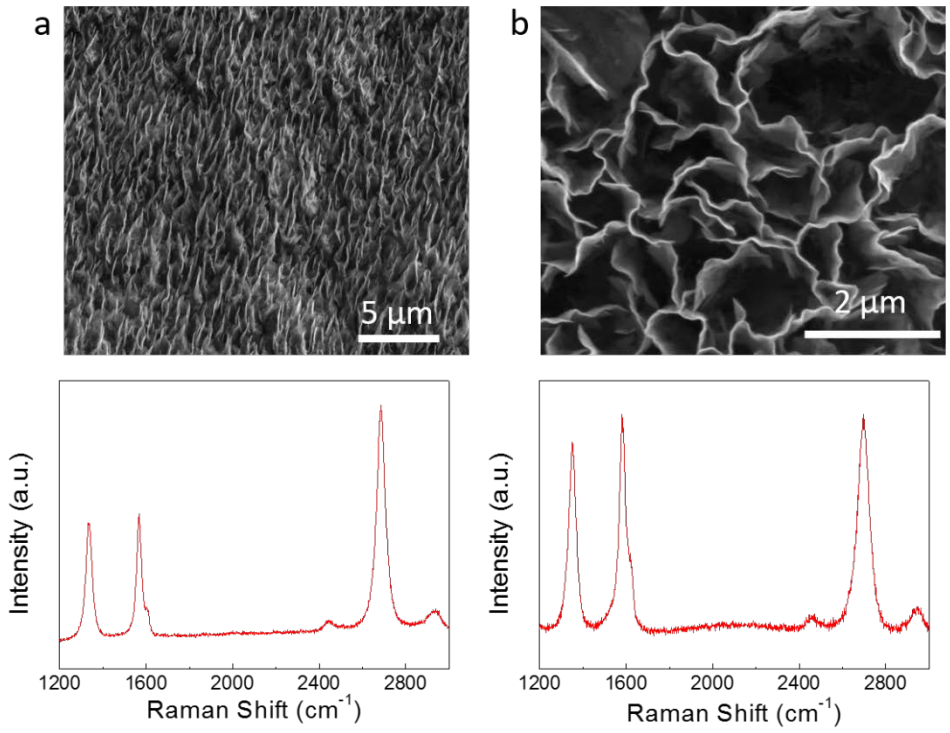

Figure 6.4. **(a)** SEM image (top) and Raman spectrum (bottom) of GNSPs on Ni foam grown by 1,2-DCB for 10 minutes. **(b)** SEM image (top) and Raman spectrum (bottom) of GNSPs on Ni foil grown by 1,2-DCB for 10 minutes.

find that the intensities of all hydrogen-related peaks (H_α, H_2, and H_β) decrease with increasing 1,2-DCB partial pressure, consistent with the reaction of hydrogen with increasing chlorine radicals. On the other hand, the intensity of C_2 radicals is enhanced upon the introduction of 1,2-DCB precursor molecules, although no further increase appears with increasing 1,2-DCB partial pressure.

Fig. 6.2(d) ~ (e) show two representative SEM images of the top view of GNSPs grown for 10 min with the growth parameters listed in the first row of Table 6.1, and Fig. 6.2(f) is the SEM image of a tilted view (at 52º) of the GNSPs shown in Fig. 6.2(d). These images together with the optical micrograph exemplified in Fig. 6.6 reveal that GNSPs uniformly distributed over the entire (1.2 cm × 0.8 cm) surface area of the Cu substrate. Moreover, we note that the widths of all GNSPs synthesized with a given set of PECVD growth parameters

appeared to be nearly the same, as exemplified by the tilted view shown in Fig. 6.2(f) where the average width of GNSPs is ~500 nm. On the other hand, there is a range of length

1,2-DCB (10^{-9} Torr)	CH_4 (10^{-9} Torr Torr)	Power (W)	Growth Time (min)	Yield(μg)
1-10	10-40	40	10	≤1
1-10	10-40	60	10	12±6
1-10	900	60	5	350±280
1-10	900	60	10	530±130
1-10	900	60	15	800±270
1-10	900	60	20	1300±430

Table 6.1 Experimental parameters for the growth process, showing the gas partial pressures of 1,2-DCB and CH_4, plasma power, and time for the PECVD growth of GNSPs. The gas partial pressures were as measured in the RGA.

distributions for the GNSPs and they are typically on the order of tens of micrometers, as exemplified by the yellow line in Fig. 6.2(d) from one open end to the other open end, and by the SEM image shown in Fig. 6.2(g) for an isolated GNSP that was transferred to a silicon substrate. Here we note that the real lengths of individual GNSPs are generally much longer than the distances between joint points revealed in the SEM images of as-grown GNSPs, as corroborated by Fig. 6.2(g).

To isolate and image individual GNSPs by SEM, we first immersed the copper substrate with as-grown GNSPs in dimethylformamide (DMF) solvent for ~ 9 h and then sonicated the solution for 3 min. A drop of the solution with dispersed GNSPs was placed on a silicon substrate and then heated at 175 ºC until the solvent completely boiled off. GNSPs left on the silicon substrate were then imaged by SEM without further modification.

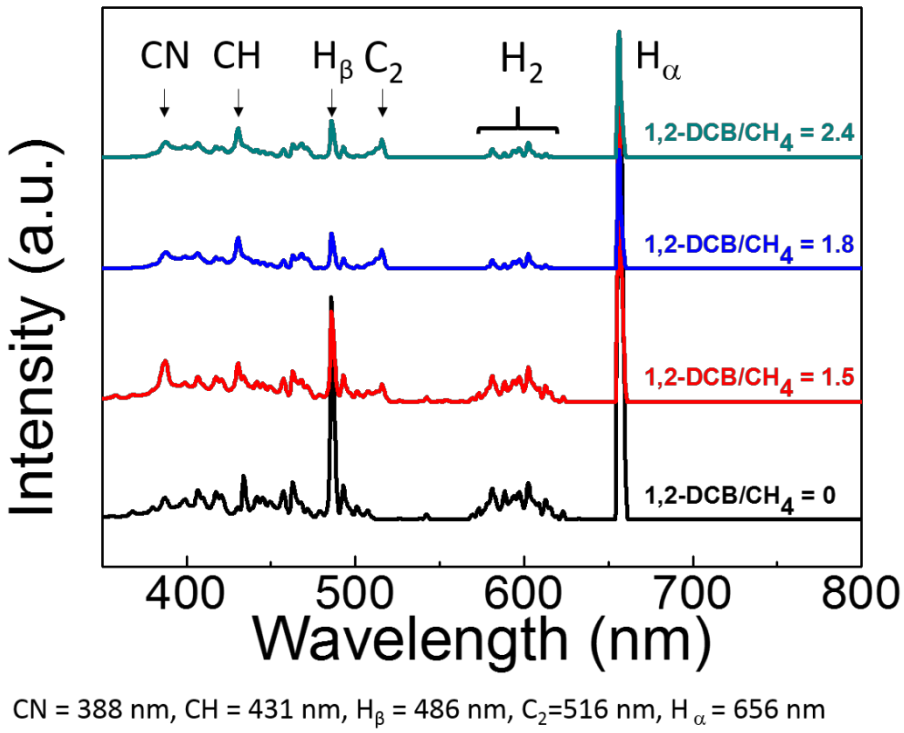

Figure 6.5. Optical emission spectroscopy (OES) of PECVD-grown GNS under different 1,2-DCB/CH_4 partial pressure ratios, showing decreasing intensities of all hydrogen-related peaks with increasing1,2-DCB partial pressure. On the other hand, the intensity of C_2 radicals, critically important for graphene growth, is enhanced upon the introduction of 1,2-DCB precursor molecules, although no further increase appears with increasing 1,2-DCB partial pressure.

By analyzing the top views of multiple sets of SEM images for the length distributions of GNSPs and the tilted views for the average widths, we obtained a representative histogram for the aspect ratios of GNSPs in Fig. 6.2(h), showing a distribution from ~10 to >~130.

A representative Raman spectrum of the GNSPs is shown in Fig. 6.2(i), where three distinct peaks are visible:[24,26,113,114] The peak at ~2700 cm^{-1} is known as the 2D-band that represents a double-resonance process of graphene; the peak at ~1590 cm^{-1} is the G-band associated with the doubly degenerate zone-center E_{2g} mode of graphene, and the peak at ~1350 cm^{-1} is the D-band that corresponds to zone-boundary phonons due to defects, edges, and/or folds of graphene sheets. Given that the laser spot of our Raman spectrometer (~1 mm) is larger than the typical widths (tens to hundreds of nanometers) of our GNSPs, we attribute the intense D-band of our GNSPs to the prevailing presence of edges and/or the presence of folds

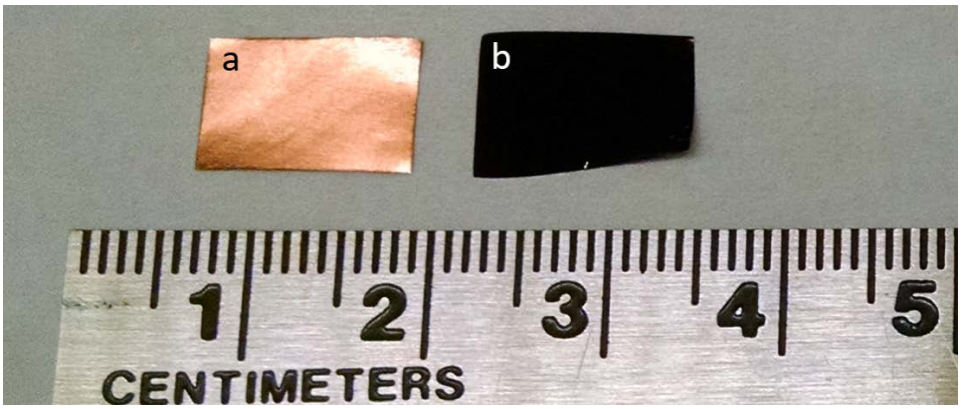

Figure 6.6. Optical micrographs of a copper substrate **(a)** before and **(b)** after the growth of GNS. The growth parameters for the micrograph in (b) are given in the last row of Table 6.1.

as observed in SEM and transmission electron microscopy (TEM) images. We further note that the 2D-to-G intensity ratio, (I_{2D}/I_G), is typically greater than 1 and that the full-width-half-maximum (FWHM) of the 2D-band is relatively sharp, which seems to suggest that our GNSPs are largely monolayer.[24,26,113–115] However, this notion contradicts the findings of multilayer GNSPs from our AFM and TEM studies. These seemingly inconsistent results can be reconciled by the presence of incommensurate rotation of one layer relative to the adjacent layers of these multilayer GNSPs, as elaborated later in this chapter. Moreover, the turbostratic multilayer structures of GNSPs may also be responsible for the appearance of a slight shoulder in the G-band peak, which is known as the D′-band that results from defects-induced intra-valley scattering.

To investigate the dependence of GNSPs growth on various parameters, we show in Fig. 6.7(a) to (c) SEM top-view images of PECVD-grown GNSPs on Cu under different 1,2-DCB/CH_4 partial pressure ratios. The total gas pressure was 500 mTorr and the flow rate of H_2 was 2 sccm. With the CH_4 partial pressure kept constant at ~6×10^{-9} Torr (based on the RGA reading) during the growth, we found that the morphology of GNSPs was strongly dependent on the ratio of 1,2-DCB to CH4 partial pressures. For instance, when the 1,2-DCB/CH_4 partial pressure ratio was ~1.5 or less, the resulting GNSPs grown on Cu had typical lengths of a few to tens of micrometers and relatively large aspect ratios, as exemplified in Fig. 6.7(a). With the partial pressure ratio of 1,2-DCB/CH_4 increased to ~1.8,

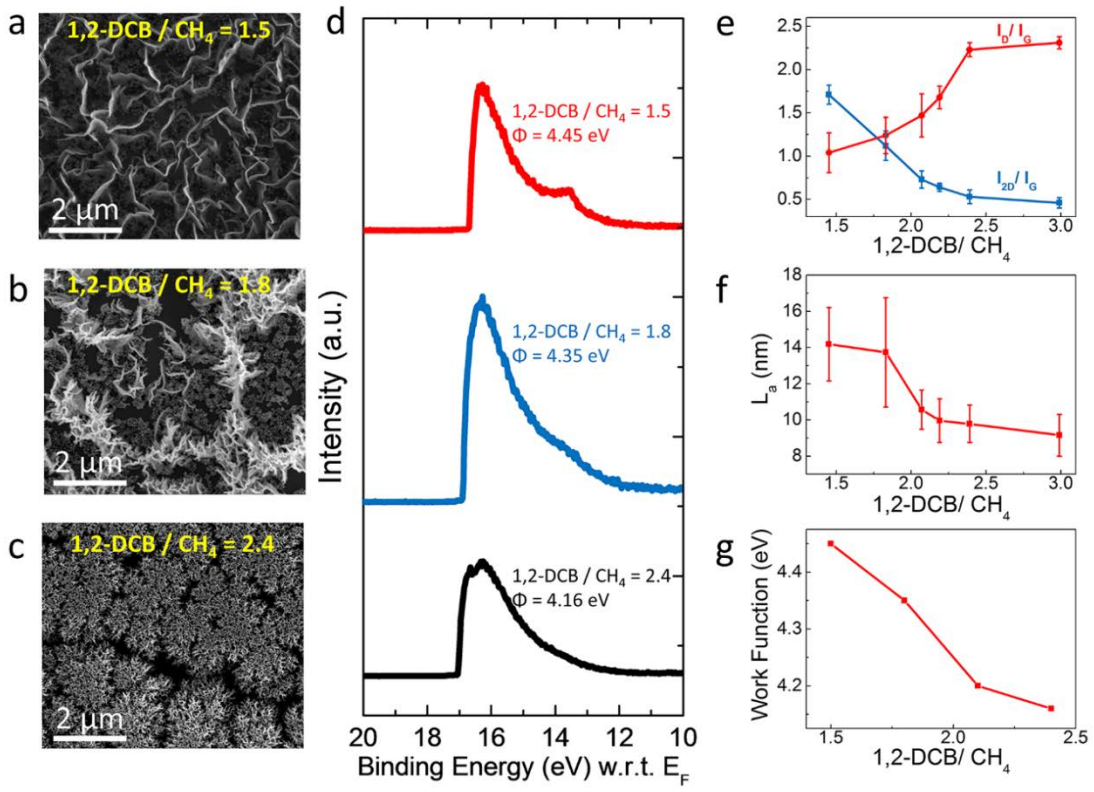

Figure 6.7. Dependence of the surface morphology, work function, Raman spectroscopy and crystalline size of GNSPs on the 1,2-DCB/CH_4 partial pressure ratio: (a)~(c) SEM images of GNSPs with 1,2-DCB/CH_4 partial pressure ratio = 1.5 in (a), 1.8 in (b) and 2.4 in (c), showing increasing branching phenomena. (d) UPS data taken on GNSPs grown under 1,2-DCB/CH_4 partial pressure ratio = 1.5, 1.8 and 2.4, showing increasing electron doping. (e) Raman 2D/G and D/G intensity ratios of GNSPs grown under different 1,2-DCB/CH_4 partial pressure ratios. (f) Planar sp^2 crystallite size (L_a) and (g) work function of our GNSPs as a function of the 1,2-DCB/CH_4 partial pressure ratio. (XPS and UPS measurement done by Wei-Shiuan Tseng)

the GNSPs began to branch out, as shown in Fig. 6.7(b). Upon further increase of the 1,2-DCB/CH4 partial pressure ratio to ~2.4, a highly branched, flowerlike nanostructure developed. These graphene “nano-flowers” (see Fig. 6.7(c)) were thinner and shorter than the typical GNSPs grown with a smaller 1,2-DCB/CH_4 partial pressure ratio. This trend was in part attributed to the high 1,2-DCB concentration that saturated the substrate and led to a high density of nucleation sites and therefore an overall decrease in the lateral size of GNSPs, as manifested in Fig. 6.7(c). The branching behavior in addition to the shorter lengths of the

graphene nanostructures may be attributed to the large amount of 1,2-DCB that resulted in excess chlorine ions terminated along the edges of the GNSPs and activated the formation of the branching behavior. This scenario is consistent with studies of the ultraviolet photoelectron spectroscopy (UPS), TEM, and energy-dispersive x-ray spectroscopy (EDS) of GNSPs as a function of the 1,2-DCB/CH_4 partial pressure ratio, to be elaborated below.

UPS experiments were conducted to investigate the work functions of GNSPs grown under different 1,2-DCB/CH_4 partial pressure ratios and to provide direct information about possible doping effects on GNSPs.[116–118] As shown in Fig. 6.7(d) and summarized in Fig. 6.7(g), the work function value Φ deduced from the secondary electron cutoff of the UPS spectrum was found to be 4.45 eV for GNSPs grown with a 1,2-DCB/CH_4 partial pressure ratio = 1.5, which is a value close to that of pristine graphene (~4.5 eV).[119] The work function value decreased to 4.16 eV for GNSPs grown with a 1,2-DCB/CH_4 partial pressure ratio increased to 2.4, implying significant electron doping. This finding suggests that excess 1,2-DCB not only resulted in the formation of branches and excess chlorine in the GNSPs (see TEM and EDS results) but also introduced additional electron doping.

We further performed Raman spectroscopic studies on GNSPs grown under different 1,2-DCB/CH_4 partial pressure ratios. Fig. 6.7(e) shows the 2D to G intensity ratios, (I_{2D}/I_G), and D to G intensity ratios, (I_D/I_G), of GNSPs grown at different 1,2-DCB/CH_4 partial pressure ratios. The (I_{2D}/I_G) ratio decreases with the increase of 1,2-DCB/CH_4 partial pressure ratio, suggesting that more layers of GNSPs were grown with larger amounts of 1,2-DCB. On the other hand, the (I_D/I_G) ratio increases with the increase of 1,2-DCB/CH_4 partial pressure ratio, which is consistent with more edges due to branching.[24,26] Additionally, the in-plane sp^2 crystallite size (L_a) of the GNSPS may be estimated by using the (I_D/I_G) ratio and the following empirical formula.[58]

$$L_a(nm) = \frac{560}{E_L^4}\left(\frac{I_D}{I_G}\right)^{-1}, \tag{6.1}$$

where E_L denotes the excitation energy of the laser source, which is 514 nm for our Raman spectrometer. We find that both the crystallite size L_a and the work function Φ of the GNSPs

decrease steadily with increasing 1,2-DCB/CH_4 partial pressure ratio, as illustrated in Fig. 6.7(f) and (g), respectively.

In order to achieve high yields of GNSPs growth, we experimented with various parameters for synthesizing typical GNSPs with 1,2-DCB/CH_4 partial pressure ratios <~1, as summarized in Table 6.1. We found that the yield of GNSPs, determined in units of mass per unit area, increased by more than one order of magnitude when the power was increased from 40W to 60W. This finding may be attributed to the presence of more energetic gas molecules and radicals (particularly C_2, C_6, and C_6H_6) in the plasma to initiate and maintain the growth of GNSPs. Additionally, higher CH_4 partial pressure and longer growth time provided more carbon sources and therefore also help increase the yield of GNSPs. On the other hand, further increase of either the plasma power above 60W or the CH_4 partial pressure could not result in higher yields, which may be the result of a limited surface area of the Cu substrate in our growth chamber for initiating the vertical growth of GNSPs. Moreover, excess plasma power tends to increase the amount of C_2 radicals at the expense of reducing the amount of C_6 radicals and C_6H_6 molecules. Given that C_6 radicals and C_6H_6 molecules are likely playing an important role in enhancing the growth rate of GNSPs, proper balance between the plasma power and the amount of C_6 and C_6H_6 is necessary to achieve high yields of GNSPs.

By optimizing various growth parameters, we found that the best yield for 20 min of growth time could reach (1.30 ± 0.43) mg/cm^2, or equivalently, (13.0 ± 4.3) g/m^2. The high-yield growth of GNSPs resulted in a completely darkened surface of the substrate due to dense coverage of GNSPs on the metallic substrate, as exemplified by the optical micrographs in Fig. 6.6 (a) - (b) and the nearly zero optical transmission from 400 nm to 800 nm shown in the main panel of Fig. 6.6. The completely darkened substrate surface by the coverage of GNSPs and the vanishing optical transmission is indicative of strong light absorption by GNSPs, which may be attributed to effective light trapping in stacks of GNSPs due to multiple subwavelength scattering. Thus, GNSPs may be considered as efficient light

absorbers for potential applications to photovoltaic cells when combined with proper plasmonic nanostructures.[95]

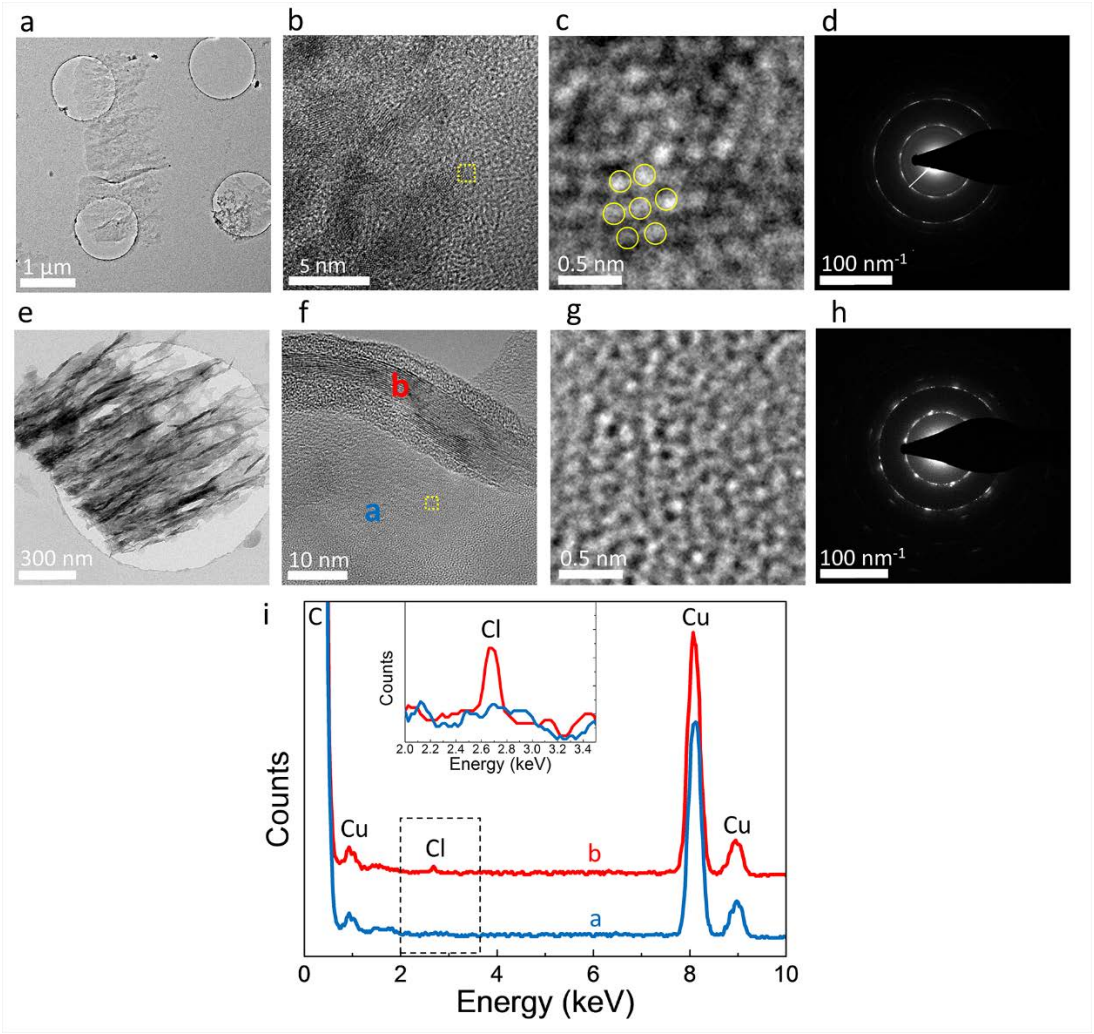

Figure 6.8. (a) ~ (c) TEM top view images of GNSPs with successively increasing resolution from large scale to atomic-scale images, with (c) being the expansion of a region indicated by the small yellow box in (b). (d) SAD pattern of GNSPs for the region shown in (c). (e) ~ (f) TEM top view images of graphene nanoflowers from large scale to atomic-scale images, with (g) being the expansion of a region indicated by the small yellow box in (f). (h) SAD pattern of the sample region shown in (g). (i) EDS data shows a distinct chlorine peak on a branching region labeled by b in (f), which is in stark contrast to the absence of chlorine in flat areas such as the region labeled by a. The inset is an expansion of the dashed area shown in the main panel. (TEM measurement done by Marcus Teague)

Next, nanoscale structural properties and chemical compositions of the PECVD-grown GNSPs were investigated by means of TEM and EDS. Measurements were initially performed on standard GNSPs similar to those shown in Fig. 6.7(a). Fig. 6.8(a) ~ (c) are TEM top view images, with successively increasing resolution, of GNSPs grown with a 1,2-DCB/CH_4 partial pressure ratio ~ 1.5. From detailed TEM studies, we found that the typical size of GNSPs transferred to the TEM grid was 500 nm ~ 1.0 μm in width and 5 ~ 10 μm in length, as exemplified in Fig. 6.8(a). The shorter lengths than those of the as-grown GNSPs (as represented by the histogram in Fig. 6.2(h)) may be attributed to the TEM sample preparation steps that involved sonication of GNSPs in a solution that led to shortened samples.

These GNSPs were generally flat over large areas and exhibited ordered nanoscale structures, as illustrated in Fig. 6.8(b). High-resolution images taken on these flat areas further revealed graphene atomic lattice structures, as shown in Fig. 6.8(c). We found that these GNSPs were mostly multilayers and turbostratic: From selected area diffraction (SAD) in Fig. 6.8(d), the sample exhibited two predominant orientations and exceeded 6 layers in thickness. This finding of multilayer GNSPs seems to differ from Raman spectroscopic studies of the same GNSPs that always revealed both (I_{2D}/I_G) ratios > 1 and relatively small FWHM in the 2D-band and so would imply monolayer GNSPs.[26,29,114] However, we note that the Raman spectra of multilayer graphene sheets with turbostratic stacking (where individual layers separated by a larger than normal interlayer distance) were also found to exhibit (I_{2D}/I_G) ratios >1.[22] Therefore, our findings derived from the TEM studies of standard GNSPs can be reconciled with the Raman spectroscopic studies.

In addition to studies of the structural properties, we performed nanoscale EDS measurements on flat, unstrained regions of these standard GNSPs, and found a pure carbon composition without any chlorine or other contaminants. This finding is in contrast to studies of the “nano-flowers” samples where chlorine appeared in regions with bifurcations, branching, or strain, as explained below.

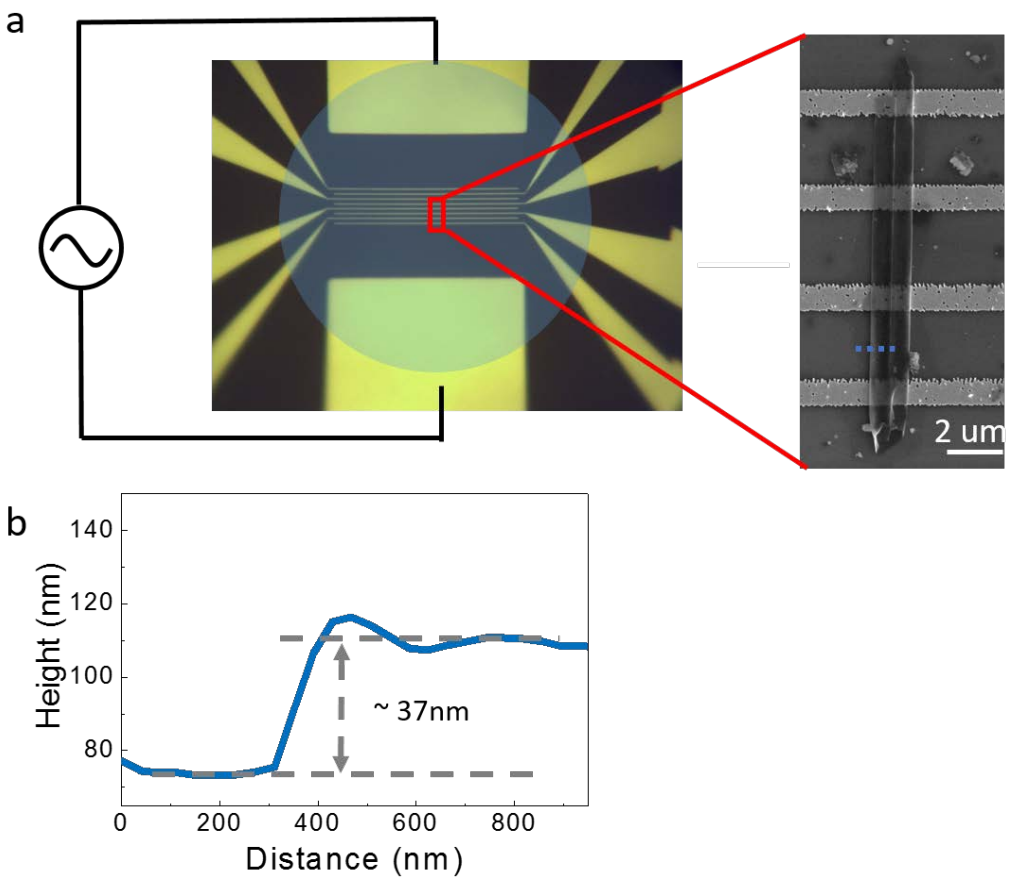

Figure 6.9. (a) (Left) Setup of the dielectrophoresis method[2,3] to align GNSPs on the Au electrodes. (Right) An SEM image of a GNSP on four Au electrodes. **(b)** AFM cross-section of the image along the blue line in the SEM image of (a).

In Fig. 6.8(e)-(g), we show TEM images with successively increasing resolution that were taken on nano-flower GNSPs grown with a 1,2-DCB/CH_4 partial pressure ratio ~ 2.3. In contrast to the typical images taken on standard GNSPs, Fig. 6.8(e) and (f) reveal that nano-flowers generally consisted of a large number of layers, with numerous branching points and reorientations of the layers. In particular, Fig. 6.8(f) shows that in the reoriented graphene region the number of graphene layers within the field of view is > 20, whereas graphene atomic structures can be resolved in flat regions, as exemplified in Fig. 6.8(g). Further SAD studies on a flat region of the sample in Fig. 6.8(f) exhibit a diffraction pattern that provides evidence for multiple layers, with varying orientations for many individual graphene layers that lead to the disordered circular pattern. On the other hand, a significant chlorine peak in the EDS data is always observed at a large number of branching and reorientation locations

in the nano-flower samples, as exemplified in Fig. 6.8(i). This presence of a distinct chorine peak in a branching region of the nano-flowers is in stark contrast to the absence of any chlorine signal in the flat region of the same samples.

We also investigated the electrical properties of the standard GNSPs by aligning them on Au electrodes using the dielectrophoresis techniques,[120,121] as shown in Fig. 6.9(a)-(b). The procedure for aligning the GNSPs is as follows: We immersed the GNS-covered copper foils in dichlorobenzene solvent for 20 hours to lift GNSPs off the copper foils and then sonicated the suspension for 3 minutes to break down big chunks of GNSPs. Then we used a micropipette to drop the suspension onto a set of Au electrodes where an AC field of a frequency 500 kHz was applied while the voltage steadily increased up to 60 volts and kept on until the dichlorobenzene evaporated completely at room temperature.

Fig. 6.9(b) is an AFM cross-section of the image along the blue line in the SEM image of Fig. 6.9(a). From our TEM studies, we found that the interlayer distances of the multilayer, turbostratic GNSPs ranged from 0.355 nm to 0.394 nm, larger than the interlayer spacing (0.335 nm) of pristine graphite. Thus, from the resistivity and thickness measurements of aligned GNSPs using the dielectrophoresis method, We found that the sheet resistance R of a single layer GNSPs to be ranging from ~7.0 kΩ/sq to ~7.8 kΩ/sq at room temperature, which were larger than that of typical pristine graphene sheet resistance (~1 kΩ/sq), but were significantly smaller than those values (~50 kΩ/sq to ~ 30 kΩ/sq) reported for lithographically patterned single-layer GNSPs of comparable widths (100 nm ~ μm),[122] suggesting good conducting properties of our GNSPs even in the absence of excess doping. If we take the work function of undoped graphene to be 4.50 eV,[118] the electron density n_{2D} of our standard GNSPs with $\Phi = 4.45$ eV (and therefore a Fermi energy $E_F \sim 0.05$ eV above the Dirac point) is estimated to be $n_{2D} = (E_F/\hbar v_F)^2/\pi \sim 1.0\times 10^{11}$ cm^{-2} for a Fermi velocity $v_F = 10^6$ m/s.[4] Therefore, the electrical mobility μ of our GNSPs is found to be $\mu = \left(n_{2D} e R_{sq}\right)^{-1} =$ 8000 ~ 9000 cm^2/V-s at room temperature, which is 5 ~ 10 times smaller than that of our typical PECVD-grown graphene sheets[29] and is about 10^2 ~ 10^3 times better than that of the vertical graphene nano-sheets reported to date.[36,112]

6.4 Discussion

The prominent presence of C_6 radicals and C_6H_6 molecules in our plasma growth process is likely important for increasing the growth rate and yield of GNSPs because graphene structures can be more effectively assembled from these molecules than from C_2 radicals. This notion is further corroborated by recent studies using solution plasma-induced formation of nano-carbons,[123] which revealed that among hexane, hexadecane, cyclohexane, and benzene, the synthesis rate from benzene was the highest.

Our empirical findings are suggestive of the importance of both 1,2-DCB precursor molecules and the resulting C_6, C_6H_6 and chlorine radicals in hydrogen plasma for mediating rapid vertical growth of GNSPs with large aspect ratios. In contrast to other reports for PECVD-grown vertical graphene sheets to date that generally required pretreatment of the substrates and additional substrate heating from 500 ºC to 1000 ºC,[36,112] our single step, low-power growth process requires neither active heating nor pretreatment of the substrates, indicating the effectiveness of 1,2- DCB as seeding molecules for the vertical growth of GNSPs.

6.5 Conclusions

In summary, we have developed a new high-yield single-step method for growing large quantity GNSPs on various transition metal substrates by means of PECVD and aromatic precursors such as 1,2-DCB molecules. This efficient growth method does not require any active heating and can reproducibly produce a high yield of ~10 g/m^2 within 20 min at a relatively low power of $\leq$ 60W. Moreover, the GNSPs thus produced reveal large aspect ratios (up to >~130) and can be easily transferred from the growth substrate to any other substrates. Therefore, this new growth method is highly promising for the mass production of GNSPs. From studies of the Raman spectra, SEM images, UPS, TEM images, EDS, and electrical conductivity of these GNSPs as functions of the growth parameters, we have also confirmed the high-quality of these GNSPs and found the correlation of the properties of GNSPs with the growth parameters. Based on our experimental findings, we propose a growth and branching mechanism of GNSPs that suggests the important role of the 1,2-DCB

precursor molecules in assisting the vertical growth and determining the morphology as well as the large aspect ratio of GNSPs. These findings, therefore, open up a new pathway to large-scale, inexpensive mass production of high-quality GNSPs for such large-scale applications as supercapacitors and photovoltaic cells.

Chapter 7

SELECTIVE GROWTH OF PECVD GRAPHENE ON CU NANOSTRUCTURES

7.1 Introduction

Modern semiconductor technology uses Cu interconnects because metallic conductivity and resistance to electromigration of bulk Cu are better than Al. However, as the size of the Cu interconnects scales down, strong carrier scatterings can cause reduction in the thermal and electrical conductivity of Cu[124–126]. Meanwhile, Cu has a tendency to diffuse into Si, SiO_2, and other dielectrics and cause significant reliability issues.[127–131] A barrier layer is needed to prevent Cu diffusion.

Graphene has been considered as a promising material for interconnect application due to many unique properties such as high mobility,[4] high mechanical strength,[132] and high thermal conductivity[133]. Moreover, impermeability[134] and oxidation resistance[135] of graphene make it an ideal candidate as a protection barrier material for Cu interconnects to prevent oxidation and diffusion of Cu into the underlying low-k dielectrics. Kang et al[136] synthesized graphene on Cu conducting lines of 2 μm width by the T-CVD method and found that the resistance was reduced by 2%–7% and the breakdown current density was increased by 18% compared to pure Cu wires. Mehta et al[137,138] investigated low temperature (~650 °C) deposition of graphene around Cu nanowires and found that the graphene deposition enhanced both the electrical and thermal conductivity. They also demonstrated successful blockage of Cu ion diffusion by large area multi-layer graphene membranes deposited directly on silicon oxide using PECVD. However, these experimental studies all involved high-temperature synthesis of graphene (>550 °C), which was incompatible with typical CMOS processing temperatures (<450 °C). Further, none of the aforementioned studies were carried out on realistic industrial wafers with high-density nanostructures on delicate low-k dielectrics.

In this chapter, we'll discuss how we integrate our PECVD graphene growth technique with realistic industrial wafers and demonstrate selective growth of graphene on Cu nanostructures.

7.2 Optimization of Growth Conditions

Our substrates were fabricated by an industrial semiconducting company. As shown in Fig. 7.1(a), SEM images with increasing magnification show micron-sized Cu pads (left image) and Cu nanostructures with different widths (right image). The bright areas in the SEM images represented Cu coated device and interconnect structures, and the dark areas represented a low-k dielectric material. Using proper growth conditions, we could reproducibly deposit high quality and continuous graphene layers onto the Cu nanostructures in the industrial wafers. Moreover, the low plasma power density (10 W for ~1 cm^3 volume)

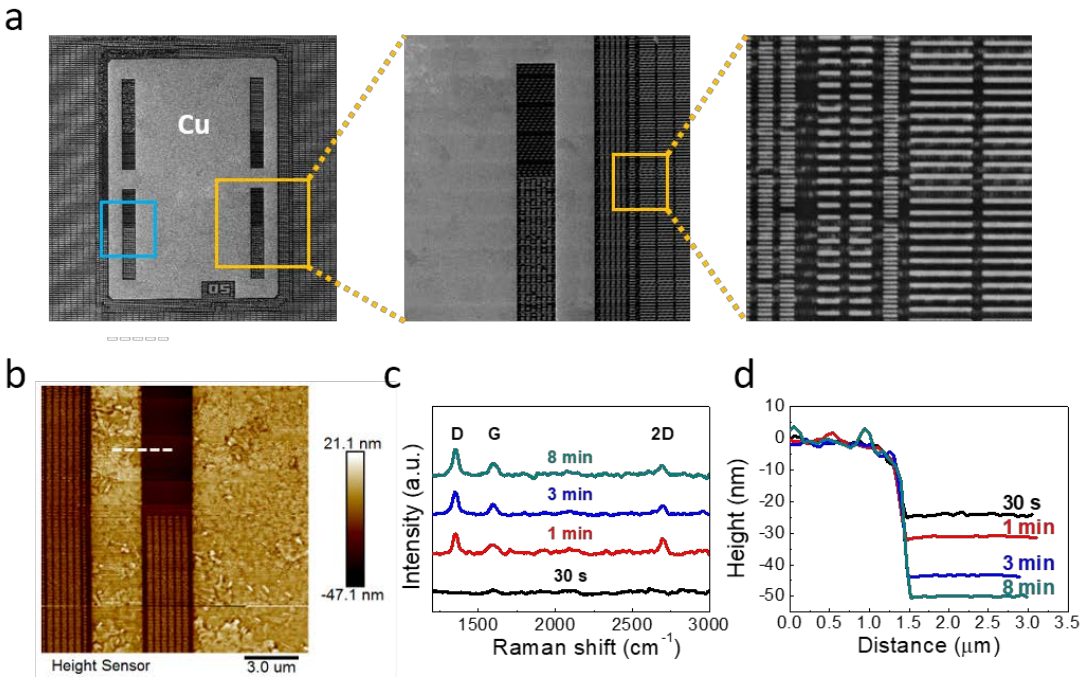

Figure 7.1 (a) SEM images of industrial wafers with increasing magnification from left to right. Right image shows Cu nanostructures with different widths, and the smallest feature is <~ 20 nm. (b) AFM images corresponding to the region indicated by the blue box in (a), after direct PECVD growth. (c) Time-evolved Raman spectra of graphene on Cu taken with increasing growth time. (d) AFM line profile (white dash line in (b)) with different growth times.

employed in the PECVD growth corresponded to a gas temperature ~160 °C, which was fully compatible with the current fabrication processes in the semiconducting industry.

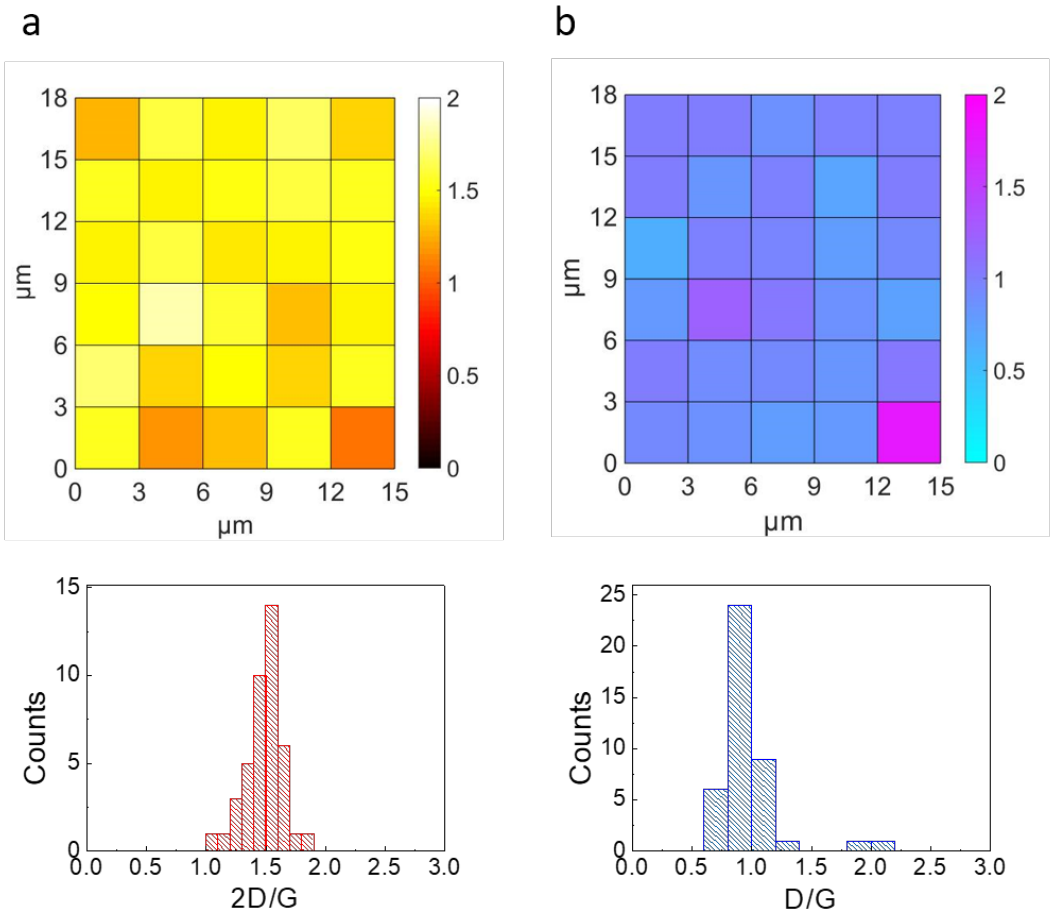

Figure 7.2 (a) (Top) Raman spatial map of the graphene I_{2D}/I_G ratio over a (15 × 18) μm^2 area. (Bottom) Histogram of the Raman I_{2D}/I_G ratio map. (b) Raman spatial map of the graphene I_D/I_G ratio over a (15 × 18) μm^2 area. (Bottom) Histogram of the Raman I_D/I_G ratio map.

Fig. 7.2 is Raman spectroscopic mapping of the samples taken over a (15 × 18) μm^2 area after PECVD processing. It confirmed that graphene coverage over the metallic nanostructures was continuous. A more quantitative comparison of the spatial distribution of the ratio in these two areas is illustrated by the histograms in Fig. 7.2. The high I_D/I_G ratio suggests this is turbostratic graphene.

However, the PECVD process was found to induce some damages to the low-k dielectrics, depending on the growth parameters and schemes of experimental setups. In Fig. 7.1(b) we show the AFM images of the region indicated by the blue box in Fig. 7.1(a) after graphene growth. In Fig. 7.1 (b) for graphene grown under direct exposure to plasma, many clusters appeared on the surface due to the low-k material etched by plasma and redeposited on the Cu surface and the graphene structures grown on Cu appeared inhomogeneous. To minimize the plasma-induced low-k damage, it's crucial to understand the mechanism of plasma damage.

7.2.1. Mechanisms of Plasma Damage

The plasma damage of low-k dielectrics involves both physical and chemical effects.[139] Physical damage is typically due to ion bombardment from the ionic species in the plasma; whereas chemical damage includes chemical reactions between the plasma and low-k material. In the following sessions, we discuss how we use different approaches to reduce both physical and chemical damages on the semiconductor industrial samples.

7.2.2 Different growth conditions

The PECVD setup is identical to Fig. 3.1(a). During the growth, the total pressure of the tube was maintained at 500 mTorr and the flow rate of hydrogen is 2 sccm. The additional methane is controlled by a precision leak valve and the partial pressure was monitored by an RGA. During the graphene synthesis, hydrogen plasma was formed away from the substrate and then moved to the substrate in order to prevent any plasma transient damages. We found the low-k damage can be controlled by the different growth parameters, such as compositions and flow rates of the gases introduced into the plasma, plasma, and the growth time. We have tabulated Table 7.1 below to compare different growth parameters and low-k damages. The low-k damage in the last column is defined by the height difference of the low-k materials

In Chapter 3 we found that Cu etching always accompanies graphene growth. Because the Cu thickness of the industrial wafer is only tens of nanometers thick, when the plasma power

is larger than 30 W, Cu will be completely etched and there is no graphene growth. Meanwhile, the low-k materials also suffer more damages due to higher plasma power. When the plasma power is reduced to 10W, we can successfully grow graphene with low-k damage around ~ 43nm.

Sample	H_2 (sccm)	CH_4 (Torr)	Power (W)	Time (s)	Graphene	Low-k damage (nm)
1	2	1×10^{-7}	40	600	No	> 50
2	2	1×10^{-7}	30	600	No	> 50
3	2	1×10^{-7}	20	600	Yes	> 50
4	2	1×10^{-7}	10	600	Yes	~ 43
5	2	1×10^{-7}	10	480	Yes	~ 39
6	2	1×10^{-7}	10	180	Yes	~ 33
7	2	1×10^{-7}	10	60	Yes	~ 21
8	2	1×10^{-7}	10	30	No	~ 14
9	2	2×10^{-7}	10	180	Yes	~ 23
10	2	5×10^{-7}	10	180	Yes	~ 17
11	2	1×10^{-6}	10	180	Yes	~ 13

Table 7.1 Experimental parameters for the growth process, showing the H_2 flow rate, gas partial pressure of CH_4, plasma power, time for the PECVD growth of graphene, validity of graphene growth, and low-k damage.

To investigate the dependence of low-k damage on various parameters, sample 4 ~ 8 in Table 7.1 shows low-k damage can be reduced significantly from 43 nm to 14 nm. Fig. 7.1(c) and (d) show time evolution Raman spectra of PECVD-graphene and the AFM line profile (white dash line in Fig. 7.1(b)) with different growth times. It takes at least 60 seconds for radicals to nucleate and form continuous graphene film on the Cu surface. Additionally, longer growth time results in more plasma damages to the low-k material. Plasma-induced damages of low-k dielectrics was estimated by measuring the height difference of Cu pads and low-k before and after PECVD processing. Before PECVD processes, the line profile was ~ 10 nm in height. By optimizing various growth parameters, we found that the least low-k damage for 60 seconds of growth time could reach ~ 14 nm.

We also found low-k damage was strongly dependent on the partial pressure of CH_4. For instance, when the partial pressure of CH_4 was 1×10^{-7} Torr and growth time was 180 seconds, the low-k damage was ~ 33nm. With the partial pressure of CH_4 increased to 2×10^{-7} Torr and 5×10^{-7} Torr, the low-k damage was reduced to 23 nm and 17nm, respectively. Upon further increase the CH_4 partial pressure to 1×10^{-6} Torr, we could reduce the damage to 13 nm. This trend was attributed to faster graphene growth associated with higher CH_4 partial pressure, which helped decrease the exposure of low-k dielectric material to the plasma environment.

7.2.3 Block UV light and ion bombardment

The damages induced by plasma to the low-k dielectrics were mainly due to energetic ion bombardment and UV light, as schematically shown in the left panel of Fig. 7.3 (a). Many research groups have figured out different setups to block the UV light and ions. For example, Shi *et al.*[140,141] have designed a gap structure to reduce the plasma damage. It contains two parallel Si spacers and a top optical window to control the energy and intensity of ions, photons, and radicals in the plasma. This window can block ions and only photons and radicals can react with the low-k material underneath the mask. Uchida *et al.*[142] and Takeda *et al.*[143] also used a similar setup to separate different radiation damages with different kinds of mask materials (MgF_2 and quartz).

To mitigate the plasma-induced damages to the low-k dielectrics, we introduced a holed graphite plate as a UV absorber, as schematically shown in the right panel in Fig. 7.3(a). we found that holed graphite was the best absorber to minimizing damages to the low-k dielectrics while allowing graphene growth on Cu nanostructures. Using this configuration, we were able to block most of the UV light and minimize damages to the low-k dielectrics. AFM images were taken after graphene growth with the graphite UV absorber as shown in Fig. 7.3 (c). It revealed significant improvement on the surface and better Raman spectra (Fig. 7.3 (d) and (e)). By changing the gap height and different plasma conditions, the radical density in the gap structure can be adjusted and therefore minimize the low-k damage.

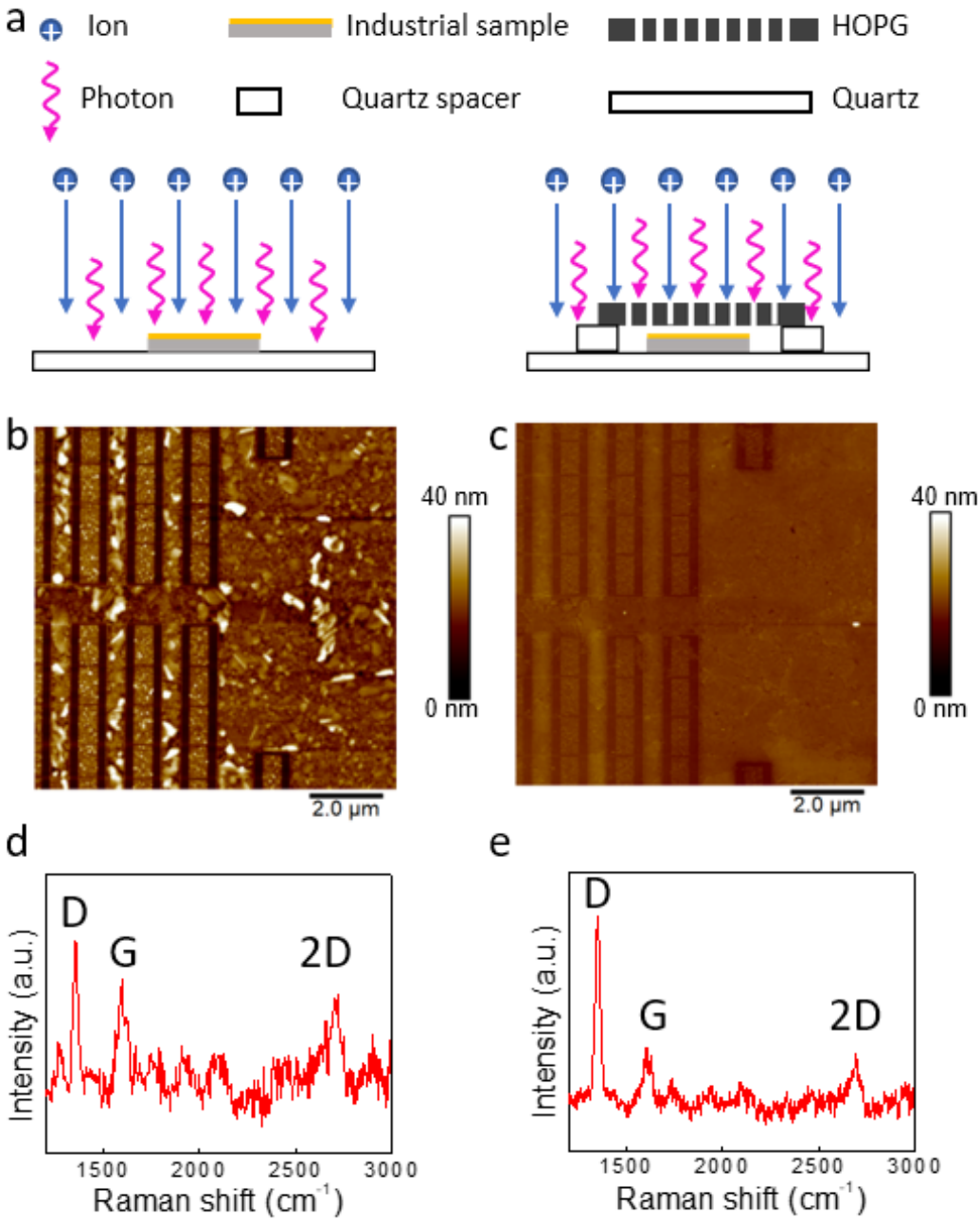

Figure 7.3 (a) Schematic drawings of the side view for the direct PECVD growth configuration (left) and that for the PECVD growth configuration with a holed graphite plate as the UV absorber (right). (b) and (c) AFM images after direct PECVD growth (b) and growth with HOPG absorber (c), respectively. (d) and (e) Raman spectra of (b) and (c), respectively.

7.2.4 Different Low-k Dielectric Material

In semiconductor manufacturing, a low-k material is a material with a dielectric constant much smaller than silicon dioxide (SiO_2 has the k-value of 4.2). Low-k material is sensitive to chemical modification, and their porosity increases the reactivity and penetration depth of reaction species. This is one of the main obstacles to integrate low-k dielectrics into integrated circuits. In this session, we'd like to investigate the effect of PECVD processing on different dielectric materials and to achieve optimized PECVD parameters for graphene synthesis that yield minimized damages to the low-k dielectrics.

We have three different low-k materials blanket wafers provided by the semiconductor industry company, which are labeled low-k 1, low-k 2, and low-k 3. We use typical e-beam lithography method to deposit 50nm thick Cu squares on the blanket wafers as a reference height (h1) and compare the height (h2) after the growth process. The plasma damage of different low-k dielectrics was estimated by measuring the height difference of Cu pads and low-k before and after PECVD processing (low-k damage = h2 – h1). Table 7.2 shows using different low-k results in dramatically different low-k damages and low-k 1 is the most resistant to the plasma damage. By applying the same PECVD growth parameters to different types of low-k dielectrics, we concluded that low-k 1 dielectric material was least susceptible to plasma-induced damages.

Low-k	H_2 (sccm)	CH_4 (Torr)	Power (W)	Time (s)	Low-k damage (nm)
1	2	1×10^{-6}	10	180	~ 3
2	2	1×10^{-6}	10	180	~ 5
3	2	1×10^{-6}	10	180	~ 8

Table 7.2 Experimental parameters for three different types of low-k dielectrics under the same growth conditions.

.

To further understand the relation of different low-k materials and the plasma-induced damages, we also applied PECVD processing conditions that yield high-quality graphene

growth (sample 11 in Table 7.1) to three types of dielectric blanket wafers provided by IMEC with different k values. They are SiO_2 as a control sample, three organosilicate glass (OSG) wafers with different k values (2.55, 2.85, and 3.0), and two ALK wafers (ALK is IMEC's internal abbreviation) with two different k values (2.0 and 2.3). Plasma-induced damage of different dielectric materials was estimated by measuring the low-k thickness before and after PECVD processing using ellipsometry. Fig. 7.4 is low-k damage of six different dielectric materials under the same growth condition with different growth times. We found that the SiO_2 substrate appears to be largely damage-free under plasma processing for up to 3 minutes. Plasma-induced damages to dielectric substrates under the same PECVD condition appear to increase with decreasing dielectric constant and increasing processing time. From these two studies, we know that choosing an appropriate low-k material is very important because it plays an important role in reducing the low-k damage.

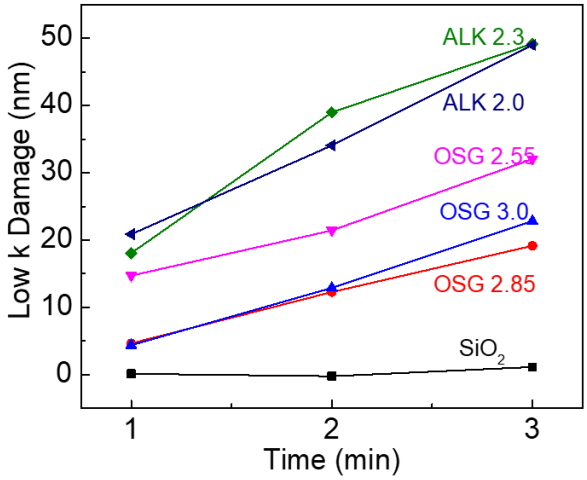

Figure 7.4 Low-k damage of six different dielectric materials under the same growth condition with different growth times.

7.3 Stability Test

The coating of multi-layers of graphene on Cu or Ni could prevent the metal from rapid oxidation.[135] Moreover, stacked graphene oxide layers were found to be water

impermeable.[144] Here we report systematic spectroscopic studies of graphene-coated realistic industrial semiconductor samples under oxygen and moisture environment.

7.3.1 Under Oxygen Environment

Here we evaluate the stability of PECVD-grown graphene at different temperatures and under oxygen environment. Specifically, the PECVD-grown graphene on copper is exposed to ~ 4 torr of O_2 gas mixed with ~ 0.7 Torr Ar and heated from 200 ~ 400 ºC for 30 minutes because these conditions are typical processing conditions in the semiconductor.

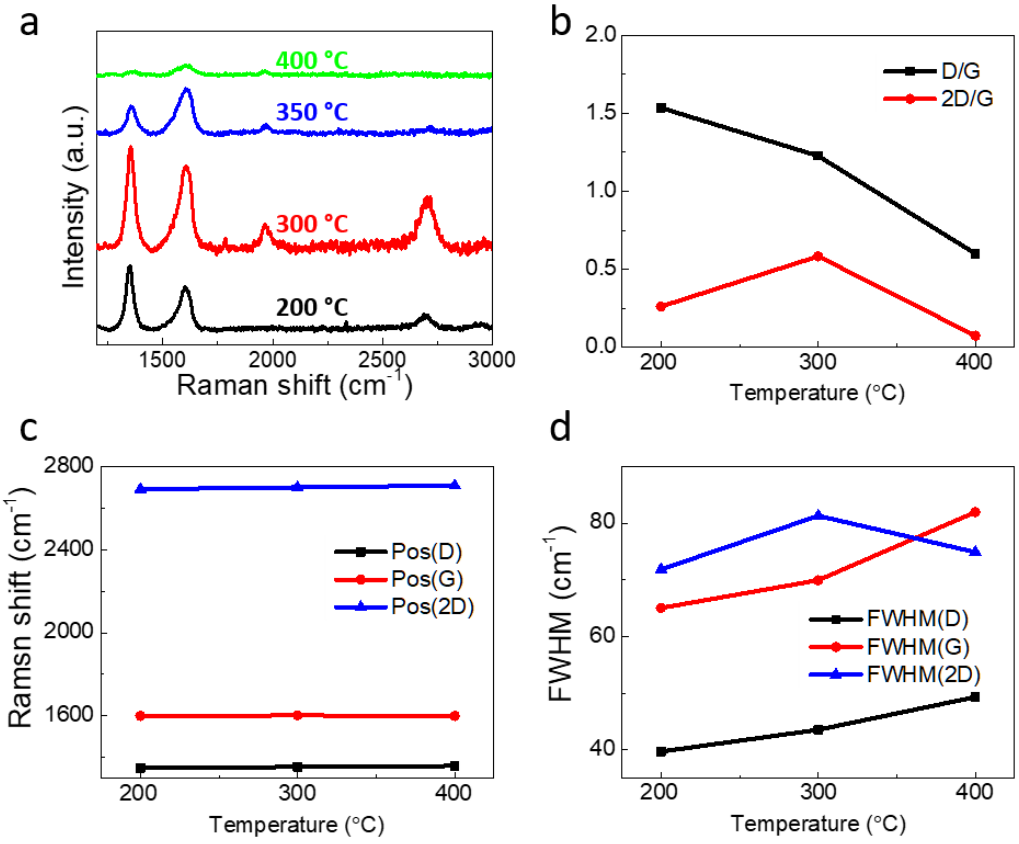

Figure 7.5 (a) Comparison of the Raman spectra of graphene taken after different annealing temperatures. (b) I_{2D}/I_G and I_D/I_G ratio (c) Position of D, G, and 2D band, and (d) FWHM of the D, G, and 2D band at different annealing temperatures.

However, there is an additional peak at ~ 1969 cm^{-1}, which could be some low-k materials redeposit on the graphene surface or radicals react with samples to form some compounds. When the temperature reaches 350ºC, the 2D peak becomes weaker and even vanishes at 400ºC. This might be due to the fact that graphene starts to react with oxygen at 350ºC.[145]

Fig. 7.5 (b) ~ (d) I_{2D}/I_G and I_D/I_G ratio, the position of D, G, and 2D band, and FWHM of the D, G, and 2D band obtained after different annealing temperatures. The decreasing of I_{2D}/I_G and I_D/I_G ratio is due to the combustion of graphene at a higher temperature. Although the position of D, G, and 2D-band remain almost unchanged with different temperatures, the FWHM linewidth of the three bands broadens with increasing annealing temperature. This may be attributed to degradation of graphene at high temperatures so that graphene begins to transform into amorphous carbon.

7.3.2 Under Moisture Environment

In order to investigate the stability of PECVD-grown graphene under moisture environment, the PECVD-grown graphene on copper is exposed to saturated moisture over varying time periods. The graphene sample was sealed in a saturated moisture environment with humidity 67% and we took Raman spectra of graphene as a function of time for up to 61 days.

The time evolution of the Raman spectral characteristic for the 2D-, G-, and D-bands of the graphene is shown in Fig. 7.6(a) ~ (d). We found that the intensity of D-band increased strongly with time. The increasing of I_D/I_G ratio is generally indicative of the degradation of single layer graphene quality. D'-band also starts to show up as the time increasing. This may be attributed to water molecules reacted with graphene edges and also increase edge states, which lead to propagating damages along the graphene grain boundaries. Meanwhile, increasing the FWHM linewidth of the 2D-band implies broadening of the phonon modes involved in the double resonance of single layer graphene. The broadening

can be understood as the result of symmetry-breaking among the carbon atoms due to excess edge stats and/or formation of other chemical bonds by the reaction of graphene and moisture. The peak positions of the three major bands remain stable with time.

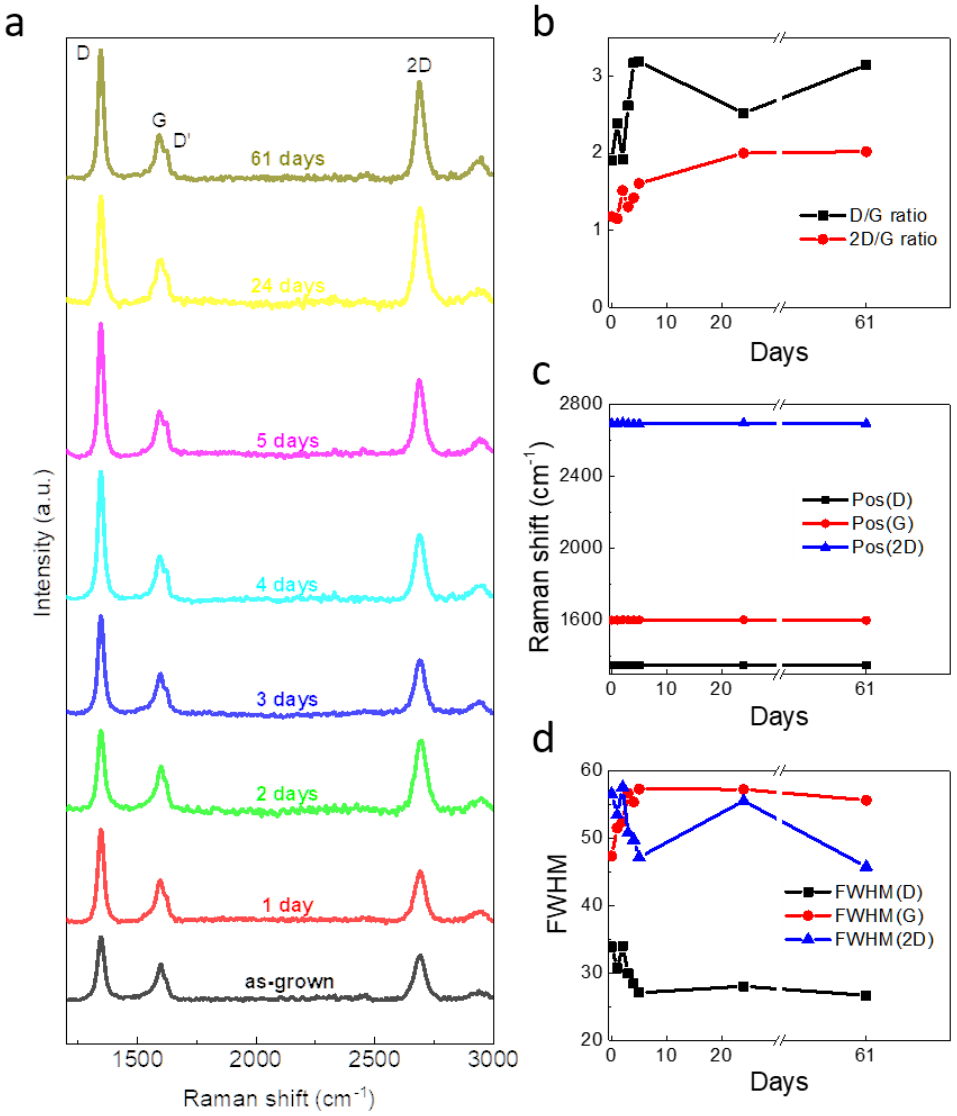

Figure 7.6 (a) The time-dependent Raman spectral evolution of graphene in 67% humidity. Time evolution of (b) I_{2D}/I_G and I_D/I_G ratio (c) D, G, and 2D band position, and (d) FWHM of the D, G, and 2D band.

7.4 Future Work

Minimize or Eliminate Plasma-induced Damages

Although we have obtained suitable plasma growth parameters to minimize plasma-induced damages to the low-k dielectrics, compared three types of low-k dielectrics, and implemented a graphite UV absorber to eliminate UV and ionic damages to the low-k dielectric, damages to the low-k and Cu surface are inevitable. Fig. 7.7 shows SEM and AFM images and Raman spectra of graphene on semiconductor industrial wafers under different growth conditions. We can see that even with our best growth conditions, the Cu RMS roughness increased from 0.564 nm to 1.70 nm. As Moore's law approaches to the atomic scale, any atomic-scale etching may change devices' performance dramatically. Further minimize or eliminate plasma-induced damages is required.

Test graphene as Cu diffusion barrier

To evaluate the quality of graphene as a barrier material to Cu from diffusion across the graphene sheet, we can either transfer blank sheets of PECVD-grown graphene to silicon substrates or directly grown graphene on silicon and then deposit Cu on top of graphene. After that, we can evaluate possible changes in the electrical transport properties or capacitance of the silicon substrate in order to investigate whether copper may have diffused across graphene into silicon to yield changes.

Graphene/Cu Nanostructure Electrical Transport

We can use e-beam lithography to pattern graphene on Cu thin film into a four-point probe configuration and perform direct conductivity measurements of PECVD-grown graphene on Cu and evaluate the improvement in conductivity of graphene on Cu versus pure Cu.

Graphene Growth on Other Metal

Resistance of interconnect at a smaller dimension is a critical scaling bottleneck. Copper resistivity is increasing due to boundary scattering and cross-sectional area reducing. The

semiconductor industry has developed and proposed using Co or Ru as an alternative metal to solve the issues in the interconnect.[146] Demonstration of a low-temperature PECVD growth of graphene uniformly on other metal but not on low-k dielectrics is also worth to explore the possibility to continue Moore's Law.

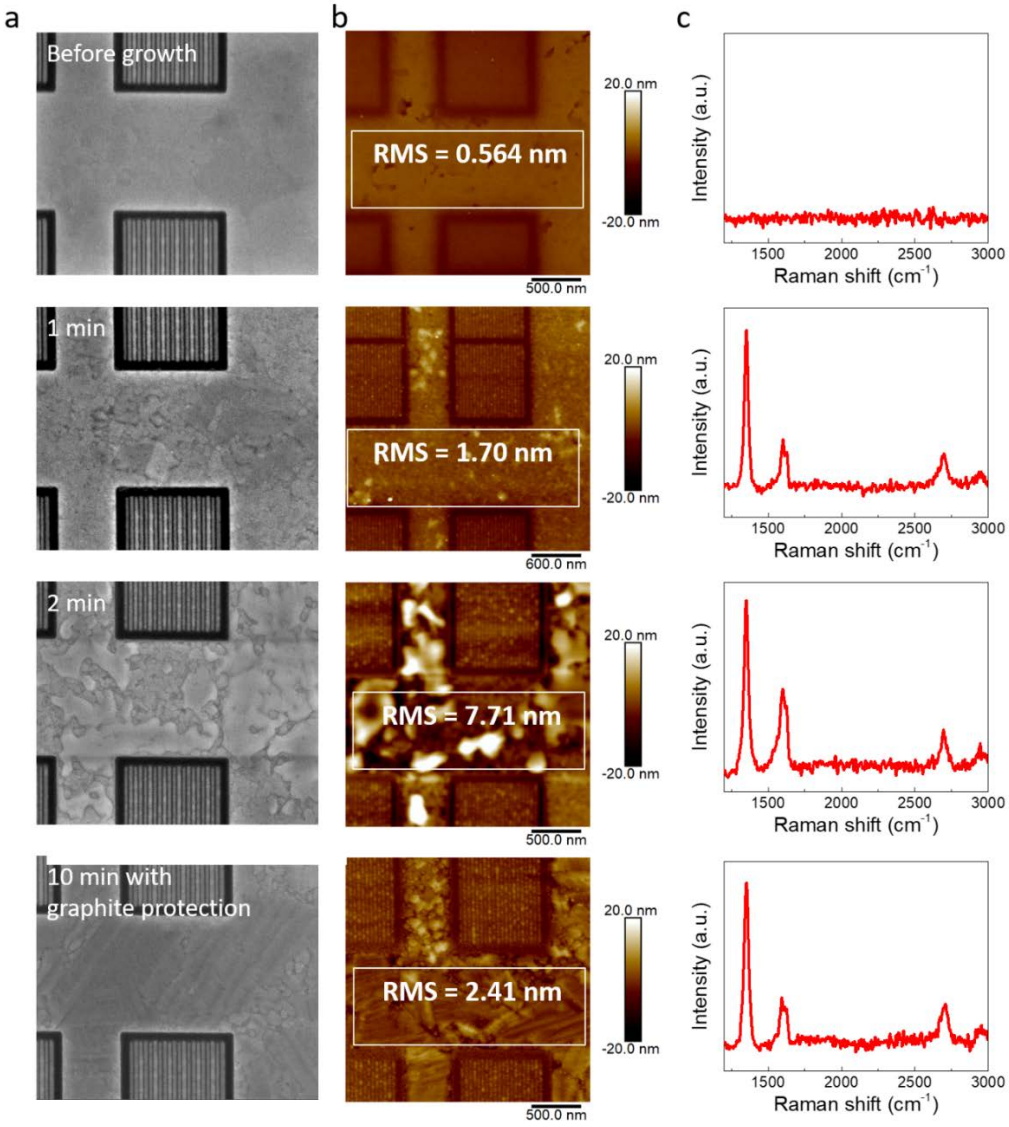

Figure 7.7 (a) SEM images (b) AFM images and (c) Raman spectra of graphene on semiconductor industrial wafers under different growth conditions. First row: before growth. Second row: 1min growth time. Third row: 2min growth time. Fourth row: 10 min growth time with graphite protection

Chapter 8

CONCLUSION

We have developed different methods in the synthesis of graphene and graphene-based nanostructures on a variety of substrates by means of PECVD techniques. The graphene synthesis includes horizontal growth of SLG and MLG sheets, vertical growth of graphene nanostructures such as graphene nano-sheets and GNSPs with large aspect ratios, and direct and selective deposition of MLG on nanostructures. The rich chemical environment provided by PECVD enables graphene growth on a range of different material surfaces at lower temperatures and faster growth than typical thermal CVD growth. Additionally, proper choices of the precursor and source gases can simplify the graphene synthesis into a single-step process, provide control of the aspect ratios, and even induce desirable functionalities in the samples. Therefore, PECVD techniques for graphene synthesis are highly versatile and also promising for large-scale industrial applications.

We have also demonstrated a new approach to manipulating the topological states in single layer graphene via nanoscale strain engineering. By placing strain-free single layer graphene on different architected nanostructures to induce global inversion symmetry breaking, we are able to induce giant pseudo-magnetic fields, realize global valley polarization, and achieve periodic one-dimensional topological channels for protected propagation of chiral Fermion modes in strained graphene. Non-local resistance and non-local magnetoresistance are measured on both strained and unstrained graphene devices, which confirm strain-induced valley Hall effect (VHE), the occurrence of quantum valley Hall effect (QVHE) at the Dirac point at low temperatures, and the presence of pseudo-magnetic field-induced quantum oscillations by nanoscale strain engineering. The methodology presented in this work not only provides a new platform for designing and controlling the gauge potential and Berry curvatures in graphene but is also promising for realizing scalable graphene-based valleytronic devices.

A p p e n d i x

RGA Spectra of PECVD Single-layer Graphene Growth

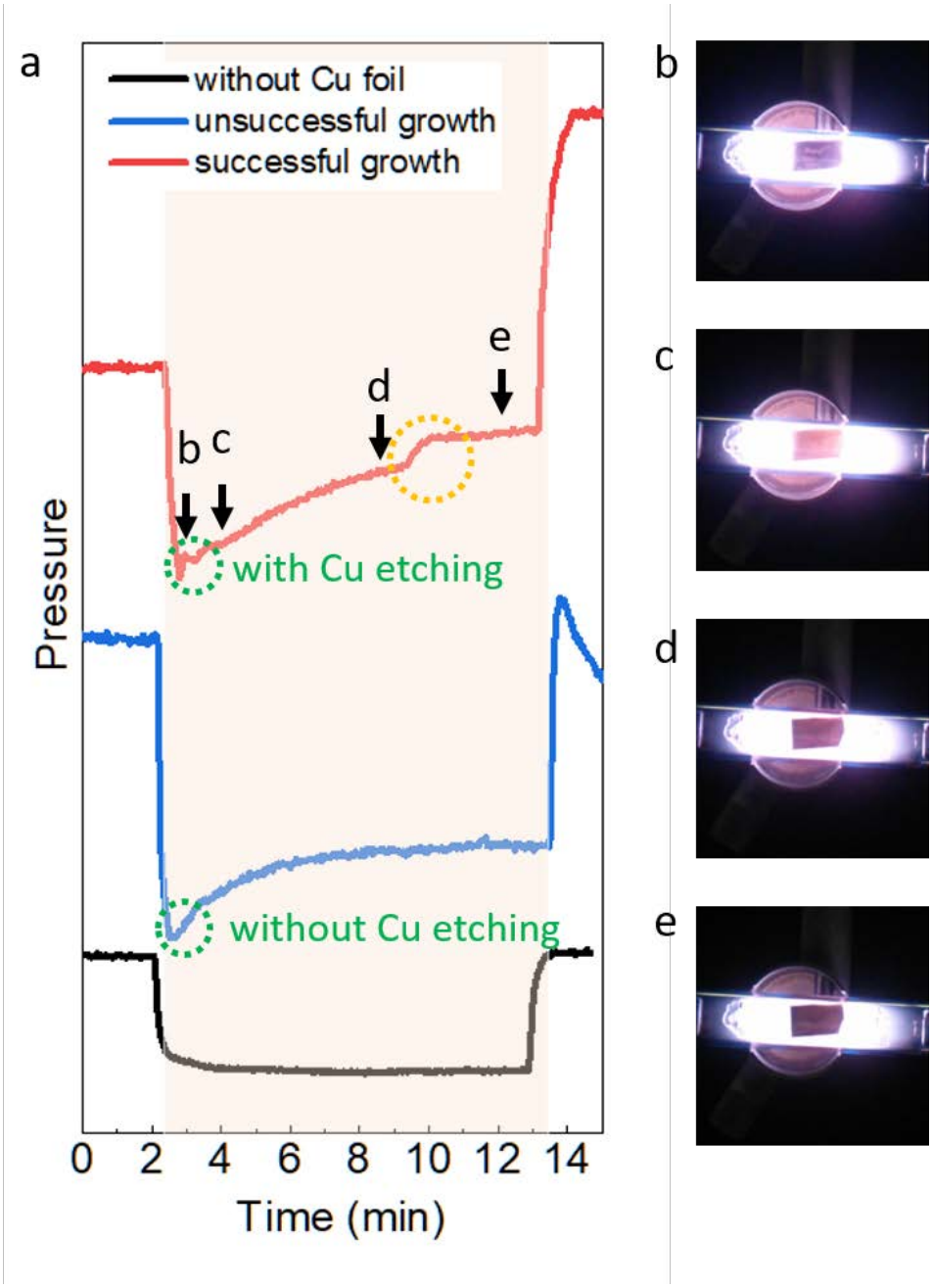

Figure A1. (a) RGA spectra of CH_4 partial pressure in the growth chamber as a function of time. (b) ~ (e) Optical images showing the change of the backside of Cu foils at different times.

One interesting feature to determine the success of graphene growth I found is the CH_4 partial pressure recorded in the RGA spectra. Fig. A1(a) is three representative RGA spectra of CH_4 partial pressure, where the shade band indicates the time interval from turning on to off the plasma. The black curve is a reference spectrum of CH_4 partial pressure where no Cu foil is inside the tube. Because CH_4 was cracked into smaller radicals in the plasma environment, the CH_4 partial pressure dropped when plasma was on. When we put Cu foil into the tube, CH_4 partial pressure changes dramatically as shown in the blue curve and red curve, where the blue curve represents an unsuccessful graphene growth and the red curve represents a successful growth. As we mentioned in Chapter 3, Cu etching always accompanies successful graphene growth. We also always found there is a peak increase at the beginning of CH_4 partial pressure when Cu starts to etch, as indicated in the green circle on the red curve. On the contrary, no such peak was seen in the blue curve when no or very little Cu etching. Next, when the graphene synthesis process is finished, there is a sudden increase of CH_4 partial pressure as shown in the yellow circle on the red curve. Fig. A1(b) ~ (e) is optical images of the backside of the Cu foil at different times during the growth, as denoted by the arrows in Fig. A1(a). Cu oxide and Cu were etched from Fig. A1(b) to (c), revealing fresh Cu surface. As graphene keeps growing on the backside and more Cu is deposited to the holder, Cu darkens with time.

Silicon Substrate Cleaning

The silicon substrate was purchased from Siltronix. It's covered with 300 nm dry-thermal oxide. The silicon is P-type Boron doped and 500μm thick. The crystal orientation is (100) and resistivity is 0.001 ~ 0.005 ohm-cm. Before any process, the silicon substrate is first sonicated in acetone and IPA, followed by an RCA clean and DI rinse. The detailed cleaning process is as follows:

1. Sonicate the Si substrates with acetone, isopropyl alcohol, and deionized water

2. RCA-1 clean

Prepare RCA-1 bath: 5 parts of deionized water + 1 part of 29% ammonia water (NH_3) + 1 part of 30% hydrogen peroxide (H_2O_2)

Soak wafer in RCA-1 bath at 75°C for 10 minutes

Rinse with DI water and blow-dry

3. RCA-2 clean

Prepare RCA-2 bath: 6 parts of deionized water + 1 part of 27% hydrogen chloride (HCl) + 1 part of 30 % hydrogen peroxide (H_2O_2)

Soak wafer in RCA-1 bath at 75°C for 10 minutes

Rinse with DI water and blow-dry

Graphene transfer

PMMA transfer

PMMA 950 A4 is spin-coated on the graphene/Cu foil at 4000 rpm for 1 minute. Then the sample is baked at 180ºC for 1 minute to evaporate the solvent. The bottom side of graphene (without PMMA protection) is etched for 1 minute in an RIE oxygen plasma at 10 sccm, 20 mTorr, and 80W. The PMMA/graphene/Cu foil is then put on top of the 0.2 M ammonium persulfate ($(NH_4)_2S_2O_8$) to etch Cu foil. A plastic spoon or glass slide is then used to scoop PMMA/graphene film and place it into a DI water bath for ~ 10 minutes to rinse the remaining ammonium persulfate residues. This rinsing process is repeated for three times to fully remove any residues. Finally, the PMMA/graphene is scooped up by the target substrate. Usually there is some water trapped between the graphene and substrate. The sample is left at room temperature to evaporate the trapped water gradually. After PMMA/graphene film fully attached to the substrate surface. The sample is baked out at ~ 50 ºC overnight to completely remove the water and graphene can be better adhesive to the substrate. PMMA is then removed in acetone overnight.

Polymer free transfer

This method is modified by a polymer-free transfer method[147] without using two syringe pumps. Similar to the PMMA transfer, graphene/Cu foil is placed on top of the Cu etchant solution, which is mixed with IPA and 0.1M ammonium persulfate. The setup is shown in Fig. A1. A glass protective holder was used to locate graphene and prevent it from attaching to the edge of the petri dish. Four glass pillars were used to fix the position of the glass protective holder from moving around. After Cu foil is etched, one pipette was used to slowly removed the etchant. Another pipette was used to slowly inject mixed DI water/IPA (10:1) solution to rinse the graphene sheet. This process is repeated three times. Finally, the target substrate is put underneath the floating graphene in the DI water/IPA solution. The solution is slowly removed by a pipette to land the graphene onto the substrate. The sample was then baked out using the same method mentioned in the PMMA transfer.

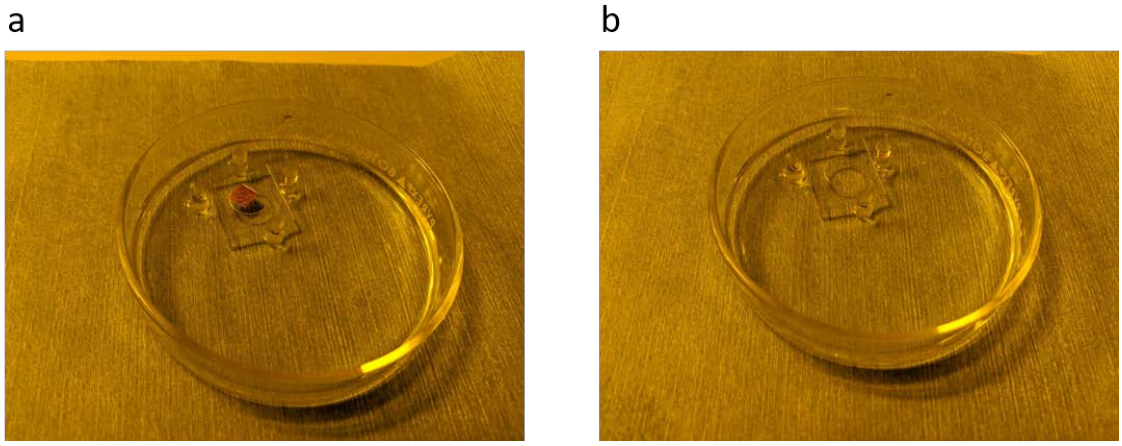

Figure A2. (a) Setup of the polymer-free transfer method. Graphene/Cu foil was placed in a glass protective holder. (b) After Cu foil was etched by $(NH_4)_2S_2O_8$

Device Fabrication

Electron Beam Lithography

The 495 A4 PMMA is spin-coated on the chip at 3000 rpm for 1 minute and baked for 1 minute. Graphene Hall bar and TLM sample are patterned by 30keV electron beam lithography with NPGS on the Quanta 200F in Kavli Nanoscience Institute. The chip is then dipped in a 3:1 volumetric ratio of isopropanol (IPA) and methyl isobutyl ketone

(MIBK) for 60 secs and then Immediately transfer to 100% IPA for 60 seconds to dilute away MIBK. The chip is blown dry by N_2. Graphene without PMMA protection is then etched using an RIE oxygen plasma at 10 sccm, 20 mTorr, and 80W for 30 seconds. PMMA is then removed in acetone overnight. The chip is then baked out in the forming gas (Ar: H_2 = 10: 1) at 350 ºC for 1 hour to remove any PMMA residues.

SiO_2 nano-cone array fabrication process

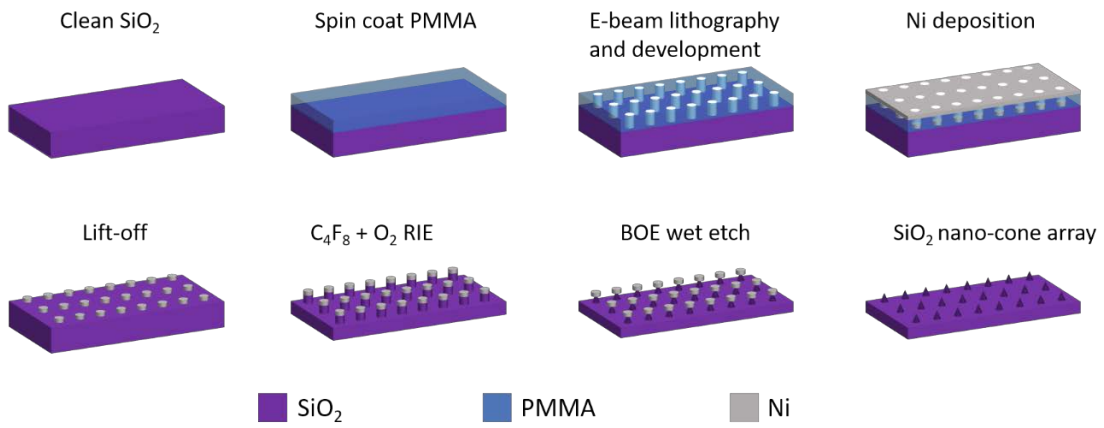

Figure A3. SiO2 nano-cone array fabrication process.

1. Si chip with a 300 nm oxide layer was ultra-sonicated in acetone and IPA for 10 min respectively and then blown dry with nitrogen.
2. Spin coat ~ 100 nm PMMA on the SiO2 and bake on a hot plate at 180 °C for 1 minute.
3. Using typical E-beam lithography method to pattern disc arrays
4. Deposit 15 nm Ni
5. Lift off the resist by soaking the chip in acetone overnight.
6. Use C_4F_8/O_2 reactive ion etching (RIE) to create SiO_2 nano-pillars.
7. Dip the chip in a buffered oxide etch (BOE) for ~ 20 seconds until Ni discs fall off.

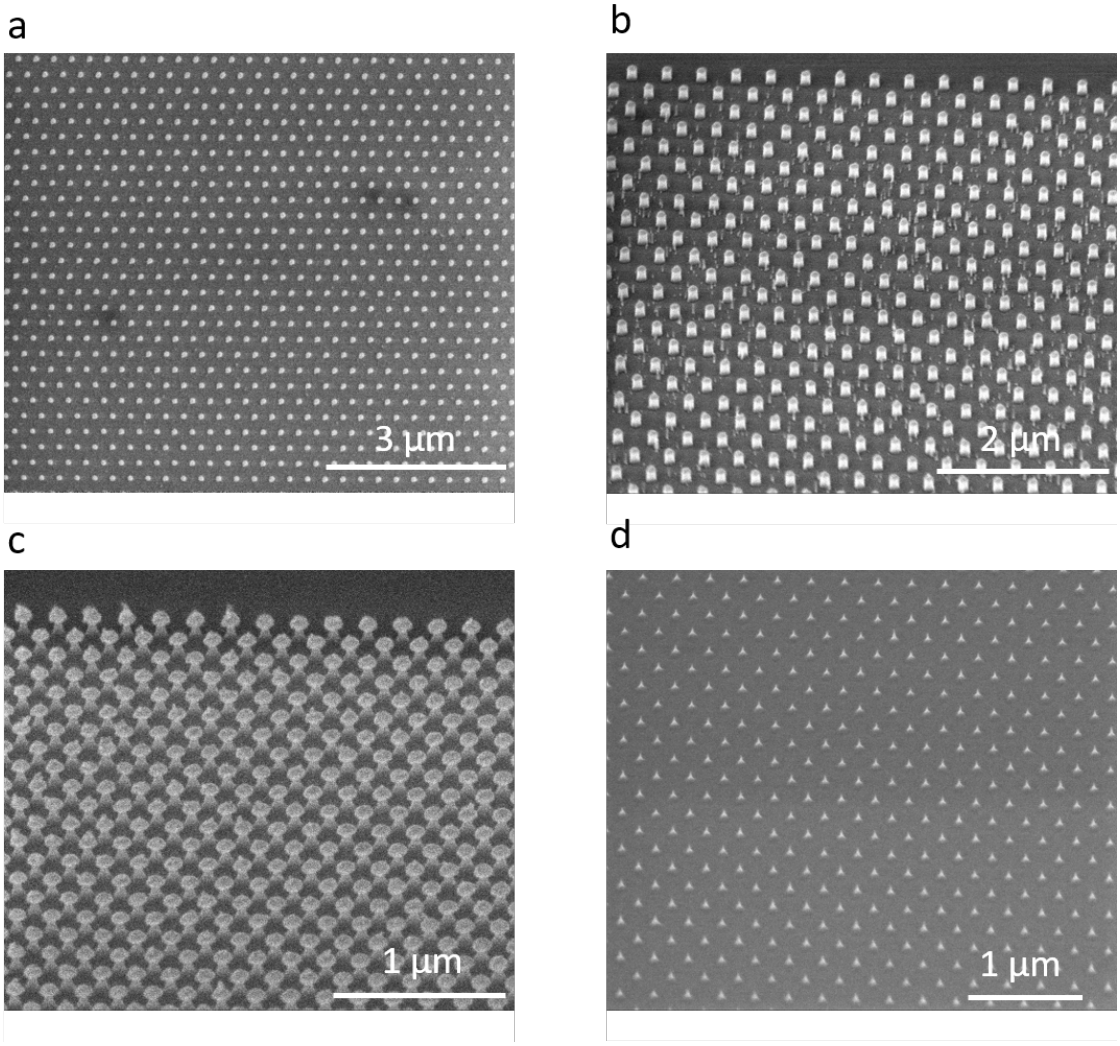

Figure A4. SEM images of (a) Ni nanodiscs on a Si substrate. (b) Ni/SiO_2 nanopillars after C_4F_8/O_2 (RIE) for 30s. (c) BOE etch for 13s. (d) BOE etch for 20s until Ni discs fall off, showing SiO_2 nanocones.

Deposit Ti/Au Contacts

Contacts are patterned by 30keV electron beam lithography with NPGS on the Quanta 200F. Bilayer resist is used to here to have a better lift-off process. The chip is spin-coated by PMMA 495 A4 at 4000 rpm for 1 minute and baked for 1 minute. The second layer is spin-coated by PMMA 950 A4 at 4000 rpm for 1 minute and baked for 1 minute. The chip is then followed by a typical electron beam lithography process.

The contacts are deposited using a Lesker Labline e-beam evaporator. In order to have a better contact resistance, it's required to deposit metal in lower pressure. Before transferring the chip into the main chamber, we deposit 10 nm Ti at 1Å/s as a titanium sublimation pump and the pressure can usually reach 3×10^{-8} torr. After transferring the chip into the main chamber, 5nm Ti at 0.5Å/s followed by 100nm Au at 1Å/s are deposited. Once the contacts have been deposited, the chip is soaking in acetone overnight. It's then sprayed with acetone and IPA to remove lift-off Au and then blown dry with N_2.

Wire Bonding

A wire bonder West Bond model 7476D-79 is used to bond Al wires from the sample contacts to the pads on a PC Board. It's found that we need to use low power to bond the wire on the sample contacts without punching through the material and shorting to the underlying Si back gate. The typical recipe I used is ultrasonic power 150 and ultrasonic time 25ms on the sample contacts.

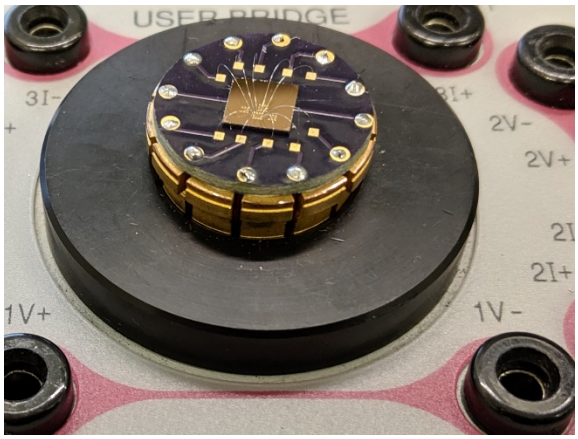

Figure A5 Optical image of samples after wire bonding.

Dielectrophoresis method for aligning graphene nanostrips

Dielectrophoresis method has been widely used in aligning carbon nanotubes (CNTs).[148–150] This method has been discovered to work on CNTs in (IPA) and CNTs move toward both electrodes and align along the electric field. Follow similar ideas, we report the alignment of GNSPs with the use of the AC dielectrophoresis method. This method is

performed by the following steps: (1) GNSPs on Cu foil samples are immersed in 1,2-DCB solvent for 20 hours to peel off GNSPs from the Cu foils, and the suspension is then sonicated for 3 minutes to break down big chunks of GNRs. (2) We patterned several electrodes (1μm wide) with 2.5 μm spacing. These thin electrodes were between two bigger electrodes which were used for applying an AC electric field to align GNSPs. (Fig. A6(a)) (3) The suspension is dropped by micropipette onto the Au electrodes. An AC electric field with frequency varies from 50 kHz to 500 kHz and voltage slowly ramping up to 60V is applied to the big electrodes until 1,2-DCB has evaporated. (Fig. A6(b))

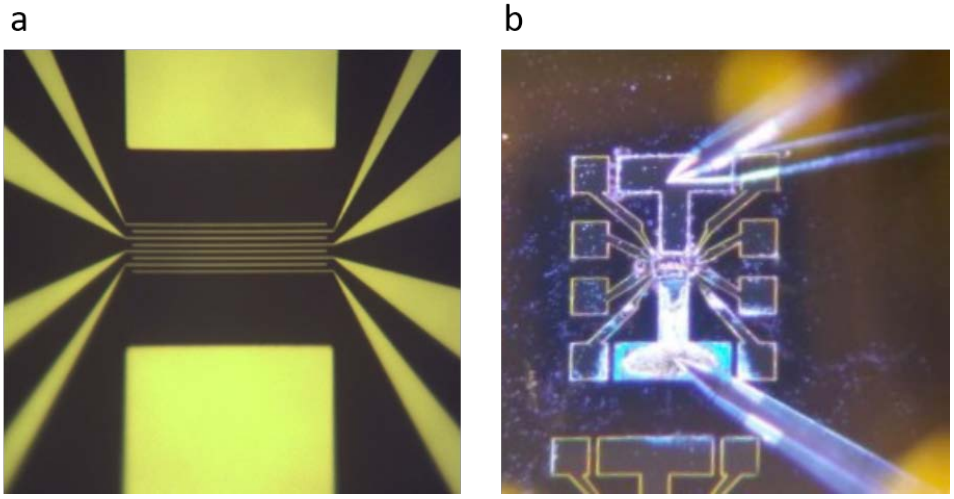

Figure A6 (a) Au electrode pattern for GNSPs alignment and electronic transport measurement. (b) AC electric field is applied to the big electrodes with two Tungsten tips.

BIBLIOGRAPHY

1. Geim, A. K. & Novoselov, K. S. The rise of graphene. *Nature Materials* **6**, 183–191 (2007).
2. Novoselov, K. S. *et al.* A roadmap for graphene. *Nature* **490**, 192–200 (2012).
3. Allen, M. J., Tung, V. C. & Kaner, R. B. Honeycomb Carbon: A Review of Graphene. *Chem. Rev.* **110**, 132–145 (2010).
4. Castro Neto, A. H., Guinea, F., Peres, N. M. R., Novoselov, K. S. & Geim, A. K. The electronic properties of graphene. *Reviews of Modern Physics* **81**, 109–162 (2009).
5. Wallace, P. R. The Band Theory of Graphite. *Phys. Rev.* **71**, 622–634 (1947).
6. Guinea, F., Katsnelson, M. I. & Geim, A. K. Energy gaps and a zero-field quantum Hall effect in graphene by strain engineering. *Nature Physics* **6**, 30 (2009).
7. Levy, N. *et al.* Strain-Induced Pseudo–Magnetic Fields Greater Than 300 Tesla in Graphene Nanobubbles. *Science* **329**, 544–547 (2010).
8. Quantal phase factors accompanying adiabatic changes. 13.
9. Mikitik, G. P. & Sharlai, Yu. V. Manifestation of Berry's Phase in Metal Physics. *Physical Review Letters* **82**, 2147–2150 (1999).
10. Xiao, D., Chang, M.-C. & Niu, Q. Berry phase effects on electronic properties. *Reviews of Modern Physics* **82**, 1959–2007 (2010).
11. Thouless, D. J., Kohmoto, M., Nightingale, M. P. & den Nijs, M. Quantized Hall Conductance in a Two-Dimensional Periodic Potential. *Physical Review Letters* **49**, 405–408 (1982).
12. Qi, X.-L. & Zhang, S.-C. The quantum spin Hall effect and topological insulators. *Physics Today* **63**, 33–38 (2010).
13. Hasan, M. Z. & Kane, C. L. *Colloquium* : Topological insulators. *Reviews of Modern Physics* **82**, 3045–3067 (2010).
14. Zhou, S. Y. *et al.* Substrate-induced bandgap opening in epitaxial graphene. *Nature Materials* **6**, 770 (2007).
15. Guinea, F., Katsnelson, M. I. & Vozmediano, M. A. H. Midgap states and charge inhomogeneities in corrugated graphene. *Physical Review B* **77**, (2008).
16. Suzuura, H. & Ando, T. Phonons and electron-phonon scattering in carbon nanotubes. *Physical Review B* **65**, (2002).
17. Mañes, J. L. Symmetry-based approach to electron-phonon interactions in graphene. *Physical Review B* **76**, (2007).
18. Guinea, F., Geim, A. K., Katsnelson, M. I. & Novoselov, K. S. Generating quantizing pseudomagnetic fields by bending graphene ribbons. *Physical Review B* **81**, (2010).
19. Guinea, F., Katsnelson, M. I. & Geim, A. K. Energy gaps and a zero-field quantum Hall effect in graphene by strain engineering. *Nature Physics* **6**, 30 (2009).
20. Yeh, N.-C. *et al.* Scanning Tunnelling Spectroscopic Studies of Dirac Fermions in Graphene and Topological Insulators. *EPJ Web of Conferences* **23**, 00021 (2012).
21. Yeh, N.-C. *et al.* Strain-induced pseudo-magnetic fields and charging effects on CVD-grown graphene. *Surface Science* **605**, 1649–1656 (2011).

22. Malard, L. M., Pimenta, M. A., Dresselhaus, G. & Dresselhaus, M. S. Raman spectroscopy in graphene. *Physics Reports* **473**, 51–87 (2009).
23. Beams, R., Gustavo Cançado, L. & Novotny, L. Raman characterization of defects and dopants in graphene. *Journal of Physics: Condensed Matter* **27**, 083002 (2015).
24. Ferrari, A. C. Raman spectroscopy of graphene and graphite: Disorder, electron–phonon coupling, doping and nonadiabatic effects. *Solid State Communications* **143**, 47–57 (2007).
25. Ferrari, A. C. & Basko, D. M. Raman spectroscopy as a versatile tool for studying the properties of graphene. *Nature Nanotechnology* **8**, 235–246 (2013).
26. Ferrari, A. C. *et al.* Raman Spectrum of Graphene and Graphene Layers. *Physical Review Letters* **97**, (2006).
27. Dimiev, A. *et al.* Layer-by-Layer Removal of Graphene for Device Patterning. *Science* **331**, 1168–1172 (2011).
28. Ferralis, N., Maboudian, R. & Carraro, C. Evidence of Structural Strain in Epitaxial Graphene Layers on 6H-SiC(0001). *Physical Review Letters* **101**, (2008).
29. Boyd, D. A. *et al.* Single-step deposition of high-mobility graphene at reduced temperatures. *Nature Communications* **6**, 6620 (2015).
30. Boyd, D. A. *et al.* Single-step deposition of high-mobility graphene at reduced temperatures. *Nature Communications* **6**, 6620 (2015).
31. Blake, P. *et al.* Graphene-Based Liquid Crystal Device. *Nano Lett.* **8**, 1704–1708 (2008).
32. Hernandez, Y. *et al.* High-yield production of graphene by liquid-phase exfoliation of graphite. *Nature Nanotechnology* **3**, 563–568 (2008).
33. Ohta, T., Bostwick, A., Seyller, T., Horn, K. & Rotenberg, E. Controlling the Electronic Structure of Bilayer Graphene. *Science* **313**, 951–954 (2006).
34. Virojanadara, C. *et al.* Homogeneous large-area graphene layer growth on 6 H - SiC(0001). *Phys. Rev. B* **78**, 245403 (2008).
35. Li, X. *et al.* Large-Area Synthesis of High-Quality and Uniform Graphene Films on Copper Foils. *Science* **324**, 1312–1314 (2009).
36. Bo, Z. *et al.* Plasma-enhanced chemical vapor deposition synthesis of vertically oriented graphene nanosheets. *Nanoscale* **5**, 5180–5204 (2013).
37. Hao, Y. *et al.* The Role of Surface Oxygen in the Growth of Large Single-Crystal Graphene on Copper. *Science* **342**, 720–723 (2013).
38. Yan, Z. *et al.* Toward the Synthesis of Wafer-Scale Single-Crystal Graphene on Copper Foils. *ACS Nano* **6**, 9110–9117 (2012).
39. Mun, J. H. & Cho, B. J. Synthesis of Monolayer Graphene Having a Negligible Amount of Wrinkles by Stress Relaxation. *Nano Lett.* **13**, 2496–2499 (2013).
40. Liang, T. *et al.* Graphene Nucleation Preferentially at Oxygen-Rich Cu Sites Rather Than on Pure Cu Surface. *Advanced Materials* **27**, 6404–6410 (2015).
41. Liang, T., Luan, C., Chen, H. & Xu, M. Exploring oxygen in graphene chemical vapor deposition synthesis. *Nanoscale* **9**, 3719–3735 (2017).
42. Habib, M. R. *et al.* A review of theoretical study of graphene chemical vapor deposition synthesis on metals: nucleation, growth, and the role of hydrogen and oxygen. *Rep. Prog. Phys.* **81**, 036501 (2018).
43. Wang, S. *et al.* A growth mechanism for graphene deposited on polycrystalline Co film by plasma enhanced chemical vapor deposition. *New J. Chem.* **37**, 1616 (2013).

44. Wang, S. M. *et al.* Synthesis of graphene on a polycrystalline Co film by radio-frequency plasma-enhanced chemical vapour deposition. *J. Phys. D: Appl. Phys.* **43**, 455402 (2010).
45. Woo, Y. *et al.* Large-grained and Highly-ordered Graphene Synthesized by Radio Frequency Plasma-enhanced Chemical Vapor Deposition. in *ECS Transactions* 111–114 (ECS, 2009). doi:10.1149/1.3119534.
46. Nandamuri, G., Roumimov, S. & Solanki, R. Remote plasma assisted growth of graphene films. *Appl. Phys. Lett.* **96**, 154101 (2010).
47. Kim, Y. *et al.* Low-temperature synthesis of graphene on nickel foil by microwave plasma chemical vapor deposition. *Appl. Phys. Lett.* **98**, 263106 (2011).
48. Peng, K.-J. *et al.* Hydrogen-free PECVD growth of few-layer graphene on an ultra-thin nickel film at the threshold dissolution temperature. *J. Mater. Chem. C* **1**, 3862 (2013).
49. Terasawa, T. & Saiki, K. Synthesis of Nitrogen-Doped Graphene by Plasma-Enhanced Chemical Vapor Deposition. *Jpn. J. Appl. Phys.* **51**, 055101 (2012).
50. Yamada, T., Ishihara, M. & Hasegawa, M. Large area coating of graphene at low temperature using a roll-to-roll microwave plasma chemical vapor deposition. *Thin Solid Films* **532**, 89–93 (2013).
51. Kim, Y. S. *et al.* Methane as an effective hydrogen source for single-layer graphene synthesis on Cu foil by plasma enhanced chemical vapor deposition. *Nanoscale* **5**, 1221 (2013).
52. Kalita, G., Wakita, K. & Umeno, M. Low temperature growth of graphene film by microwave assisted surface wave plasma CVD for transparent electrode application. *RSC Adv.* **2**, 2815 (2012).
53. Chan, S.-H. *et al.* Low-temperature synthesis of graphene on Cu using plasma-assisted thermal chemical vapor deposition. *Nanoscale Res Lett* **8**, 285 (2013).
54. Nang, L. V. & Kim, E.-T. Controllable Synthesis of High-Quality Graphene Using Inductively-Coupled Plasma Chemical Vapor Deposition. *J. Electrochem. Soc.* **159**, K93–K96 (2012).
55. van der Laan, T., Kumar, S. & Ostrikov, K. (Ken). Water-mediated and instantaneous transfer of graphene grown at 220 °C enabled by a plasma. *Nanoscale* **7**, 20564–20570 (2015).
56. Kim, J. *et al.* Low-temperature synthesis of large-area graphene-based transparent conductive films using surface wave plasma chemical vapor deposition. *Appl. Phys. Lett.* **98**, 091502 (2011).
57. Terasawa, T. & Saiki, K. Growth of graphene on Cu by plasma enhanced chemical vapor deposition. *Carbon* **50**, 869–874 (2012).
58. Cançado, L. G. *et al.* General equation for the determination of the crystallite size La of nanographite by Raman spectroscopy. *Appl. Phys. Lett.* **88**, 163106 (2006).
59. Hsu, C.-C. *et al.* High-yield single-step catalytic growth of graphene nanostripes by plasma enhanced chemical vapor deposition. *Carbon* **129**, 527–536 (2018).
60. Teague, M. L. *et al.* Evidence for Strain-Induced Local Conductance Modulations in Single-Layer Graphene on SiO2. *Nano Lett.* **9**, 2542–2546 (2009).
61. Yeh, N.-C. *et al.* Nanoscale strain engineering of graphene and graphene-based devices. *Acta Mech. Sin.* **32**, 497–509 (2016).

62. Herbut, I. F. Pseudomagnetic catalysis of the time-reversal symmetry breaking in graphene. *Physical Review B* **78**, 205433 (2008).
63. Araki, Y. Chiral symmetry restoration in monolayer graphene induced by Kekule distortion. *Phys. Rev. B* **84**, 113402 (2011).
64. Yeh, N.-C. *et al.* Nano-Scale Strain-Induced Giant Pseudo-Magnetic Fields and Charging Effects in CVD-Grown Graphene on Copper. *ECS Trans.* **35**, 161–172 (2011).
65. Rycerz, A., Tworzydło, J. & Beenakker, C. W. J. Valley filter and valley valve in graphene. *Nature Phys* **3**, 172–175 (2007).
66. Lee, M.-K., Lue, N.-Y., Wen, C.-K. & Wu, G. Y. Valley-based field-effect transistors in graphene. *Phys. Rev. B* **86**, 165411 (2012).
67. Gorbachev, R. V. *et al.* Detecting topological currents in graphene superlattices. *Science* **346**, 448–451 (2014).
68. Boyd, D. A. Chapter 13 - Block Copolymer Lithography. in *New and Future Developments in Catalysis* (ed. Suib, S. L.) 305–332 (Elsevier, 2013). doi:10.1016/B978-0-444-53874-1.00013-5.
69. Zhang, Y. *et al.* Seedless Growth of Palladium Nanocrystals with Tunable Structures: From Tetrahedra to Nanosheets. *Nano Lett.* **15**, 7519–7525 (2015).
70. Komatsu, K. *et al.* Observation of the quantum valley Hall state in ballistic graphene superlattices. *Science Advances* **4**, eaaq0194 (2018).
71. Sui, M. *et al.* Gate-tunable topological valley transport in bilayer graphene. *Nature Physics* **11**, 1027–1031 (2015).
72. Shimazaki, Y. *et al.* Generation and detection of pure valley current by electrically induced Berry curvature in bilayer graphene. *Nature Physics* **11**, 1032–1036 (2015).
73. Ju, L. *et al.* Topological valley transport at bilayer graphene domain walls. *Nature* **520**, 650–655 (2015).
74. Geim, A. K. Graphene: Status and Prospects. *Science* **324**, 1530–1534 (2009).
75. Nakada, K., Fujita, M., Dresselhaus, G. & Dresselhaus, M. S. Edge state in graphene ribbons: Nanometer size effect and edge shape dependence. *Phys. Rev. B* **54**, 17954–17961 (1996).
76. Wakabayashi, K., Fujita, M., Ajiki, H. & Sigrist, M. Electronic and magnetic properties of nanographite ribbons. *Phys. Rev. B* **59**, 8271–8282 (1999).
77. Han, M. Y., Özyilmaz, B., Zhang, Y. & Kim, P. Energy Band-Gap Engineering of Graphene Nanoribbons. *Phys. Rev. Lett.* **98**, 206805 (2007).
78. Kimouche, A. *et al.* Ultra-narrow metallic armchair graphene nanoribbons. *Nat Commun* **6**, 1–6 (2015).
79. Ruffieux, P. *et al.* On-surface synthesis of graphene nanoribbons with zigzag edge topology. *Nature* **531**, 489–492 (2016).
80. Faccio, R., Denis, P. A., Pardo, H., Goyenola, C. & Mombrú, Á. W. Mechanical properties of graphene nanoribbons. *J. Phys.: Condens. Matter* **21**, 285304 (2009).
81. Xiang, C. *et al.* Functionalized Low Defect Graphene Nanoribbons and Polyurethane Composite Film for Improved Gas Barrier and Mechanical Performances. *ACS Nano* **7**, 10380–10386 (2013).
82. Behnam, A. *et al.* Transport in Nanoribbon Interconnects Obtained from Graphene Grown by Chemical Vapor Deposition. *Nano Lett.* **12**, 4424–4430 (2012).

83. Hwang, W. S. *et al.* Graphene nanoribbon field-effect transistors on wafer-scale epitaxial graphene on SiC substrates. *APL Materials* **3**, 011101 (2015).
84. Li, X., Wang, X., Zhang, L., Lee, S. & Dai, H. Chemically Derived, Ultrasmooth Graphene Nanoribbon Semiconductors. *Science* **319**, 1229–1232 (2008).
85. Wang, Q. *et al.* Fabrication and In Situ Transmission Electron Microscope Characterization of Free-Standing Graphene Nanoribbon Devices. *ACS Nano* **10**, 1475–1480 (2016).
86. Wang, Q. H. *et al.* Understanding and controlling the substrate effect on graphene electron-transfer chemistry via reactivity imprint lithography. *Nature Chemistry* **4**, 724–732 (2012).
87. Han, W., Kawakami, R. K., Gmitra, M. & Fabian, J. Graphene spintronics. *Nature Nanotechnology* **9**, 794–807 (2014).
88. Magda, G. Z. *et al.* Room-temperature magnetic order on zigzag edges of narrow graphene nanoribbons. *Nature* **514**, 608–611 (2014).
89. Grigorenko, A. N., Polini, M. & Novoselov, K. S. Graphene plasmonics. *Nature Photonics* **6**, 749–758 (2012).
90. Brar, V. W., Jang, M. S., Sherrott, M., Lopez, J. J. & Atwater, H. A. Highly Confined Tunable Mid-Infrared Plasmonics in Graphene Nanoresonators. *Nano Lett.* **13**, 2541–2547 (2013).
91. Brar, V. W. *et al.* Hybrid Surface-Phonon-Plasmon Polariton Modes in Graphene/Monolayer h-BN Heterostructures. *Nano Lett.* **14**, 3876–3880 (2014).
92. Myung, S. *et al.* Graphene-Encapsulated Nanoparticle-Based Biosensor for the Selective Detection of Cancer Biomarkers. *Advanced Materials* **23**, 2221–2225 (2011).
93. Jin, Z. *et al.* Metallized DNA nanolithography for encoding and transferring spatial information for graphene patterning. *Nature Communications* **4**, 1663 (2013).
94. Ahuja, P., Sharma, R. K. & Singh, G. Solid-state, high-performance supercapacitor using graphene nanoribbons embedded with zinc manganite. *J. Mater. Chem. A* **3**, 4931–4937 (2015).
95. Echtermeyer, T. J. *et al.* Strong plasmonic enhancement of photovoltage in graphene. *Nature Communications* **2**, 458 (2011).
96. Wang, X. & Dai, H. Etching and narrowing of graphene from the edges. *Nature Chem* **2**, 661–665 (2010).
97. Abramova, V., Slesarev, A. S. & Tour, J. M. Meniscus-Mask Lithography for Narrow Graphene Nanoribbons. *ACS Nano* **7**, 6894–6898 (2013).
98. Cai, J. *et al.* Atomically precise bottom-up fabrication of graphene nanoribbons. *Nature* **466**, 470–473 (2010).
99. Vo, T. H. *et al.* Large-scale solution synthesis of narrow graphene nanoribbons. *Nature Communications* **5**, 3189 (2014).
100. From Nanographene and Graphene Nanoribbons to Graphene Sheets: Chemical Synthesis - Chen - 2012 - Angewandte Chemie International Edition - Wiley Online Library. https://onlinelibrary.wiley.com/doi/full/10.1002/anie.201201084.
101. Narita, A. *et al.* Bottom-Up Synthesis of Liquid-Phase-Processable Graphene Nanoribbons with Near-Infrared Absorption. *ACS Nano* **8**, 11622–11630 (2014).

102. Daigle, M., Miao, D., Lucotti, A., Tommasini, M. & Morin, J.-F. Helically Coiled Graphene Nanoribbons. *Angewandte Chemie International Edition* **56**, 6213–6217 (2017).
103. Yang, W., Lucotti, A., Tommasini, M. & Chalifoux, W. A. Bottom-Up Synthesis of Soluble and Narrow Graphene Nanoribbons Using Alkyne Benzannulations. *J. Am. Chem. Soc.* **138**, 9137–9144 (2016).
104. Goldfinger, M. B. & Swager, T. M. Fused Polycyclic Aromatics via Electrophile-Induced Cyclization Reactions: Application to the Synthesis of Graphite Ribbons. *J. Am. Chem. Soc.* **116**, 7895–7896 (1994).
105. Jordan, R. S. *et al.* Synthesis of Graphene Nanoribbons via the Topochemical Polymerization and Subsequent Aromatization of a Diacetylene Precursor. *Chem* **1**, 78–90 (2016).
106. Sisto, T. J. *et al.* Long, Atomically Precise Donor–Acceptor Cove-Edge Nanoribbons as Electron Acceptors. *J. Am. Chem. Soc.* **139**, 5648–5651 (2017).
107. Chen, L., Hernandez, Y., Feng, X. & Müllen, K. From Nanographene and Graphene Nanoribbons to Graphene Sheets: Chemical Synthesis. *Angewandte Chemie International Edition* **51**, 7640–7654 (2012).
108. Genorio, B. *et al.* In Situ Intercalation Replacement and Selective Functionalization of Graphene Nanoribbon Stacks. *ACS Nano* **6**, 4231–4240 (2012).
109. Kosynkin, D. V. *et al.* Highly Conductive Graphene Nanoribbons by Longitudinal Splitting of Carbon Nanotubes Using Potassium Vapor. *ACS Nano* **5**, 968–974 (2011).
110. Wong, C. H. A., Chua, C. K., Khezri, B., Webster, R. D. & Pumera, M. Graphene Oxide Nanoribbons from the Oxidative Opening of Carbon Nanotubes Retain Electrochemically Active Metallic Impurities. *Angewandte Chemie International Edition* **52**, 8685–8688 (2013).
111. Ambrosi, A. *et al.* Graphene and its electrochemistry – an update. *Chem. Soc. Rev.* **45**, 2458–2493 (2016).
112. Hiramatsu, M. & Hori, M. *Carbon nanowalls: synthesis and emerging applications*. (Springer, 2010).
113. Dimiev, A. M. *et al.* Direct Real-Time Monitoring of Stage Transitions in Graphite Intercalation Compounds. *ACS Nano* **7**, 2773–2780 (2013).
114. Dimiev, A. M., Bachilo, S. M., Saito, R. & Tour, J. M. Reversible Formation of Ammonium Persulfate/Sulfuric Acid Graphite Intercalation Compounds and Their Peculiar Raman Spectra. *ACS Nano* **6**, 7842–7849 (2012).
115. Sun, Z. *et al.* Large-Area Bernal-Stacked Bi-, Tri-, and Tetralayer Graphene. *ACS Nano* **6**, 9790–9796 (2012).
116. Liu, Z. *et al.* The Application of Highly Doped Single-Layer Graphene as the Top Electrodes of Semitransparent Organic Solar Cells. *ACS Nano* **6**, 810–818 (2012).
117. Hsu, C.-L. *et al.* Layer-by-Layer Graphene/TCNQ Stacked Films as Conducting Anodes for Organic Solar Cells. *ACS Nano* **6**, 5031–5039 (2012).
118. Kim, H. *et al.* Organic solar cells using CVD-grown graphene electrodes. *Nanotechnology* **25**, 014012 (2013).
119. Zhou, Y. *et al.* Quantitative secondary electron imaging for work function extraction at atomic level and layer identification of graphene. *Scientific Reports* **6**, 21045 (2016).

120. Separation of Metallic from Semiconducting Single-Walled Carbon Nanotubes | Science. https://science.sciencemag.org/content/301/5631/344.
121. Vijayaraghavan, A. *et al.* Dielectrophoretic Assembly of High-Density Arrays of Individual Graphene Devices for Rapid Screening. *ACS Nano* **3**, 1729–1734 (2009).
122. Qi, Z. J. *et al.* Correlating Atomic Structure and Transport in Suspended Graphene Nanoribbons. *Nano Lett.* **14**, 4238–4244 (2014).
123. Morishita, T. *et al.* Fastest Formation Routes of Nanocarbons in Solution Plasma Processes. *Scientific Reports* **6**, 36880 (2016).
124. Graham, R. L. *et al.* Resistivity dominated by surface scattering in sub-50 nm Cu wires. *Appl. Phys. Lett.* **96**, 042116 (2010).
125. Huang, Q., Lilley, C. M., Bode, M. & Divan, R. Surface and size effects on the electrical properties of Cu nanowires. *Journal of Applied Physics* **104**, 023709 (2008).
126. Steinhögl, W., Schindler, G., Steinlesberger, G. & Engelhardt, M. Size-dependent resistivity of metallic wires in the mesoscopic range. *Phys. Rev. B* **66**, 075414 (2002).
127. Lloyd, J. R., Murray, C. E., Ponoth, S., Cohen, S. & Liniger, E. The effect of Cu diffusion on the TDDB behavior in a low-k interlevel dielectrics. *Microelectronics Reliability* **46**, 1643–1647 (2006).
128. Alers, G. B., Jow, K., Shaviv, R., Kooi, G. & Ray, G. W. Interlevel dielectric failures in copper/low-k structures. *IEEE Transactions on Device and Materials Reliability* **4**, 148–152 (2004).
129. Gonella, R. Key reliability issues for copper integration in damascene architecture. *Microelectronic Engineering* **55**, 245–255 (2001).
130. Shacham-Diamand, Y., Dedhia, A., Hoffstetter, D. & Oldham, W. G. Copper Transport in Thermal SiO2. *J. Electrochem. Soc.* **140**, 2427–2432 (1993).
131. Fisher, I. & Eizenberg, M. Copper ion diffusion in porous and nonporous SiO2-based dielectrics using bias thermal stress and thermal stress tests. *Thin Solid Films* **516**, 4111–4121 (2008).
132. Briggs, B. D. *et al.* Electromechanical robustness of monolayer graphene with extreme bending. *Appl. Phys. Lett.* **97**, 223102 (2010).
133. Balandin, A. A. *et al.* Superior Thermal Conductivity of Single-Layer Graphene. *Nano Lett.* **8**, 902–907 (2008).
134. Bunch, J. S. *et al.* Impermeable Atomic Membranes from Graphene Sheets. *Nano Lett.* **8**, 2458–2462 (2008).
135. Chen, S. *et al.* Oxidation Resistance of Graphene-Coated Cu and Cu/Ni Alloy. *ACS Nano* **5**, 1321–1327 (2011).
136. Kang, C. G. *et al.* Effects of multi-layer graphene capping on Cu interconnects. *Nanotechnology* **24**, 115707 (2013).
137. Mehta, R., Chugh, S. & Chen, Z. Enhanced Electrical and Thermal Conduction in Graphene-Encapsulated Copper Nanowires. *Nano Lett.* **15**, 2024–2030 (2015).
138. Mehta, R., Chugh, S. & Chen, Z. Transfer-free multi-layer graphene as a diffusion barrier. *Nanoscale* **9**, 1827–1833 (2017).
139. Baklanov, M. R. *et al.* Plasma processing of low-k dielectrics. *Journal of Applied Physics* **113**, 041101 (2013).

140. Shi, H. *et al.* Plasma altered layer model for plasma damage characterization of porous OSG films. in *2009 IEEE International Interconnect Technology Conference* 78–80 (2009). doi:10.1109/IITC.2009.5090345.
141. Shi, H. *et al.* Role of ions, photons, and radicals in inducing plasma damage to ultra low-k dielectrics. *Journal of Vacuum Science & Technology B* **30**, 011206 (2011).
142. Uchida, S. *et al.* Plasma damage mechanisms for low-k porous SiOCH films due to radiation, radicals, and ions in the plasma etching process. *Journal of Applied Physics* **103**, 073303 (2008).
143. Takeda, K. *et al.* Mechanism of plasma-induced damage to low-k SiOCH films during plasma ashing of organic resists. *Journal of Applied Physics* **109**, 033303 (2011).
144. Nair, R. R., Wu, H. A., Jayaram, P. N., Grigorieva, I. V. & Geim, A. K. Unimpeded Permeation of Water Through Helium-Leak-Tight Graphene-Based Membranes. *Science* **335**, 442–444 (2012).
145. Eftekhari, A. & Jafarkhani, P. Curly Graphene with Specious Interlayers Displaying Superior Capacity for Hydrogen Storage. *J. Phys. Chem. C* **117**, 25845–25851 (2013).
146. Ren, H. *et al.* Resistance Scaling of Cu Interconnect and Alternate Metal (Co, Ru) Benchmark toward sub 10nm Dimension. in *2018 IEEE International Interconnect Technology Conference (IITC)* 166–168 (2018). doi:10.1109/IITC.2018.8430411.
147. Lin, W.-H. *et al.* A Direct and Polymer-Free Method for Transferring Graphene Grown by Chemical Vapor Deposition to Any Substrate. *ACS Nano* **8**, 1784–1791 (2014).
148. Krupke, R., Hennrich, F., Löhneysen, H. v & Kappes, M. M. Separation of Metallic from Semiconducting Single-Walled Carbon Nanotubes. *Science* **301**, 344–347 (2003).
149. Yamamoto, K., Akita, S. & Nakayama, Y. Orientation and purification of carbon nanotubes using ac electrophoresis. *J. Phys. D: Appl. Phys.* **31**, L34–L36 (1998).
150. Xu, X. *et al.* Electrophoretic Analysis and Purification of Fluorescent Single-Walled Carbon Nanotube Fragments. *J. Am. Chem. Soc.* **126**, 12736–12737 (2004).